Preface

A small gathering of science and engineering enthusiasts in 2003, organized under the title SISY conference - Serbian-Hungarian Joint Symposium on Intelligent Systems, has grown into an annual international meeting that presents latest results and achievements in Mathematics, Informatics, Intelligent Manufacturing Systems, Intelligent Mechatronics, Intelligent Robotics, Computational Intelligence. Our conference is now proudly called International Symposium on Intelligent Systems and Informatics, and it is a member of the prestigious IEEE family of conferences.

This special issue of Acta Polytechnica Hungarica is dedicated to the 17th meeting held in 2019. The papers presented in this volume are elaborations of the most notable presentations that received the highest marks during the review process. A wide range of contemporary topics is covered, from inequalities for nontypical integrals, such as bipolar Shilkret, Sugeno and Choquet integrals, and derivative-free method for singular systems, through Adaptive Control of Single Variable 2nd Order Systems, Electric Vehicle Sensor and Control Network, Interior Navigation System, Enterprise Data Storage Systems, Bluetooth Mesh Architectural Models, all the way to fuzzy systems, namely Fuzzy FxLMS Algorithm and Fuzzy Failure Modes.

We are very grateful to all the authors for their enthusiasm during the preparation of contributions for this special issue and for sharing their research with us especially for this occasion.

Last, but not the least, we wish to express our gratitude to the founding fathers of our SISY conference for creating this wonderful opportunity for presenting and exchanging ideas and opinions in such pleasant surroundings, the birthplace of fruitful cooperation, joint projects, and long-lasting scientific collaborations. Also, we are honestly thankful to the editorial board of Acta Polytechnica Hungarica for making this issue possible.

Ivana Štajner-Papuga and Márta Takács

Guest Editors

Jensen Type Inequality for the Bipolar Shilkret, Sugeno and Choquet Integrals

Biljana Mihailović[a], Mirjana Štrboja[b], Miloš Todorov[c]

[a] University of Novi Sad, Faculty of Technical Sciences,
Trg Dositeja Obradovića 6, 21000 Novi Sad, Serbia, lica@uns.ac.rs

[b] University of Novi Sad, Faculty of Sciences, Department of Mathematics and Informatics, Trg Dositeja Obradovića 4, 21000 Novi Sad, Serbia, mirjana.strboja@dmi.uns.ac.rs

[c] University of Novi Sad, Faculty of Technical Sciences, Trg Dositeja Obradovića 6, 21000 Novi Sad, Serbia, todorov.dt6.2013@uns.ac.rs

Abstract: In this paper we prove the Jensen type inequality for the discrete bipolar Shilkret and Sugeno integrals. We propose the conditions for the validity of this type inequality for the discrete bipolar Choquet integral. In order to illustrate the obtained results, some examples are given.

Keywords: bi-capacity; bipolar Choquet integral; bipolar Shilkret integral; bipolar Sugeno integral; Jensen's inequality

1 Introduction

Non-additive (fuzzy) integrals with respect to capacities, or fuzzy measures have been studied in [6, 9, 14, 19] as aggregation tools in multicriteria decision analysis, with a wide range of applications in economics, machine learning, engineering, etc. Among these integrals based on capacities, let us mention prominent ones as the Choquet integral [4, 5, 18], the Sugeno integral [26, 27], and the Shilkret integral [22].

In recent years, the concept of bipolar fuzzy integrals more general than integral models such as Cumulative prospect theory (CPT) [31] has been considered in [8, 10-12, 16]. In [11] the discrete bipolar universal integral based on bi-capacities was defined and discussed, as an extension of the bipolar Choquet integration proposed in [8] and the bipolar fuzzy integration introduced in [12]. Recently, the idea was further developed in [25, 28, 30] by introducing and investigating the bipolar pseudo-integrals and bipolar pan-integrals in discrete settings.

Due to the integrals based on capacities are used extensively, the research of integral inequalities related to fuzzy integrals based on capacities has been explored by various authors in [1, 2, 13, 15, 20, 21, 24]. Jensen's inequality has usage in many disciplines, such as mathematical economics, probability and optimization theory, etc. This inequality has also been studied for the bipolar pseudo-integral [30]. However, in the case of bipolar pseudo-integrals, the underlining bi-capacities have to be $\oplus$-decomposable, where $\oplus$ is a corresponding pseudo-addition. Therefore, it is useful to consider other types of integrals, based on the bipolar scale and related to an arbitrary normalized bi-capacity, and to investigate the inequalities of such type for these integrals. Hence, our main goal now is to propose the conditions for validity of the Jensen type inequality for the bipolar Shilkret, Sugeno and Choquet integrals.

This paper is based on [29] and [17]. The paper is organized as follows. In Section 2, an overview related to bi-capacities and the bipolar fuzzy integrals with respect to bi-capacities is given. In Section 3, the Jensen type inequality for the bipolar Shilkret integral and the bipolar Sugeno integral are proved, based on [29]. Novel results related to the reversed Jensen type inequality are shown and new illustrative examples are given. In Section 4, using results from [17], as a novel result the Jensen type inequality for the bipolar Choquet integral is considered and the reversed Jensen type inequality for this integral is obtained. Finally, some concluding remarks are given.

2 Preliminaries

According to [7, 8, 11, 12], in this section, some basic notions related to bi-capacities and the bipolar Shilkret, Sugeno and Choquet integrals are presented. Recall that the symmetric maximum and the symmetric minimum are operations $\veebar, \barwedge\colon [-1,1]^2 \to [-1,1]$ given by:

$$x \veebar y = \operatorname{sign}(x+y)(|x| \vee |y|);$$

$$x \barwedge y = \operatorname{sign}(x \cdot y)(|x| \wedge |y|).$$

The symmetric maximum $\veebar$ is not associative, hence we adopt the next convention based on the splitting rule:

$$\bigveebar_{x_i \in I} x_i = \sup_{x_i \geqslant 0} x_i \veebar \inf_{x_i < 0} x_i,$$

for any subset I of the interval $[-1,1]$.

Let $X = \{x_1, x_2, \ldots, x_n\}$ be a non-empty set, which defines the set of arguments, and $\mathcal{P}(X)$ be its partitive set.

Recall, a mapping $\mathrm{m}\colon \mathcal{P}(X) \to [0,1]$ is said to be a capacity (or fuzzy measure) if $\mathrm{m}(\emptyset) = 0$ and for all $A \subset B \subset X$ it holds $\mathrm{m}(A) \leq \mathrm{m}(B)$.

Definition 1 *([7])A mapping* $\mathbf{m}: Q(X) \to \mathbb{R}$, *where*

$$Q(X) := \{(A,B) \in \mathcal{P}(X) \times \mathcal{P}(X) |\ A \cap B = \emptyset\},$$

is said to be a bi-capacity if $\mathbf{m}(\emptyset,\emptyset) = 0$ *and for all* $A \subset B \subset X$ *it holds*

$$\mathbf{m}(A,\cdot) \leq \mathbf{m}(B,\cdot) \quad and \quad \mathbf{m}(\cdot,A) \geq \mathbf{m}(\cdot,B).$$

Now, let us consider $f: X \to [-1,1]$ and a bi-capacity $\mathbf{m}: Q(X) \to [-1,1]$. We denote $f(x_i) = f_i$, $i = 1, \dots, n$.

In the sequel, the class containing all functions $f: X \to [-1,1]$ will be denoted by $\mathcal{S}$. The class of all normalized bi-capacities $\mathbf{m}: Q(X) \to [-1,1]$, i.e. such that $\mathbf{m}(X,\emptyset) = 1 = -\mathbf{m}(\emptyset,X)$, will be denoted by $\mathcal{M}$. For each $A \in \mathcal{P}(X)$, the characteristic function is defined as usual by

$$\chi_A(x) = \begin{cases} 0, & x \notin A \\ 1, & x \in A. \end{cases}$$

For each $(A,B) \in Q(X)$, $\chi_{(A,B)} \in \mathcal{S}$ is defined by

$$\chi_{(A,B)}(x) = \begin{cases} 1, & x \in A, \\ -1, & x \in B, \\ 0, & x \notin A \cup B. \end{cases}$$

Obviously, for all $(A,B) \in Q(X)$, it holds $\chi_{(A,B)} = \chi_A - \chi_B$.

For all $t \in]0,1]$, the couple of sets $(\{x \in X \mid f(x) \geq t\}, \{x \in X \mid f(x) \leq -t\})$, shortly denoted by $(\{f \geq t\}, \{f \leq -t\})$ belongs to $Q(X)$. In order to ensure the same property for $t = 0$, $(\{f \geq 0\}, \{f \leq 0\})$ will be interpreted as $(\{f \geq 0\}, \{f < 0\})$.

The bipolar Shilkret integral was introduced in [12] and studied in [11].

Definition 2 *For* $f \in \mathcal{S}$ *and* $\mathbf{m} \in \mathcal{M}$, *the bipolar Shilkret integral is defined by*

$$BSh(f,\mathbf{m}) = \mathbb{V}_{i=1}^{n} |f_i| \cdot \mathbf{m}(\{f \geq |f_i|\}, \{f \leq -|f_i|\}).$$

Let X_n be a finite set of cardinality n for $n \in \mathbb{N}$, $\mathcal{S}_n$ be the class of all functions from the set X_n to the interval $[-1,1]$ and $\mathcal{M}_n$ be the class of all normalized bi-capacities on $Q(X_n)$. The main properties of bipolar Shilkret integral $BCh: \cup_{n\in\mathbb{N}} \mathcal{S}_n \times \mathcal{M}_n \to [-1,1]$, given in [11], are:

(Sh1) $BSh(c \cdot \chi_{(A,B)}, \mathbf{m}) = c \cdot \mathbf{m}(A,B)$, for all $c \in [0,1]$ and for all $\mathbf{m} \in \mathcal{M}_n$, $(A,B) \in Q(X_n)$, $n \in \mathbb{N}$;

(Sh2) $BSh(f,\mathbf{m}_1) \geq BSh(g,\mathbf{m}_2)$, for all pairs $(f,\mathbf{m}_1) \in \mathcal{S}_{n_1} \times \mathcal{M}_{n_1}$, and $(g,\mathbf{m}_2) \in \mathcal{S}_{n_2} \times \mathcal{M}_{n_2}$, $n_1, n_2 \in \mathbb{N}$ satisfying

$$\mathbf{m}_1(\{f \geq t\}, \{f \leq -t\}) \geq \mathbf{m}_2(\{g \geq t\}, \{g \leq -t\}), \tag{1}$$

for all $t \in]0,1]$.

The bipolar Sugeno integral was initially introduced in [12] and studied in [11].

Definition 3 *For $f \in \mathcal{S}$ and $\mathbf{m} \in \mathcal{M}$, the bipolar Sugeno integral is given by*

$$BSu(f, \mathbf{m}) = \mathbb{V}_{i=1}^{n} |f_i| \ \mathbb{\wedge} \ \mathbf{m}(\{f \geq |f_i|\}, \{f \leq -|f_i|\}).$$

The bipolar Sugeno integral $BSu: \cup_{n\in\mathbb{N}} \mathcal{S}_n \times \mathcal{M}_n \to [-1,1]$ possesses the following properties:

(Su1) $BSu(c \cdot \chi_{(A,B)}, \mathbf{m}) = c \ \mathbb{\wedge} \ \mathbf{m}(A,B)$, for all $c \in [0,1]$ and for all $\mathbf{m} \in \mathcal{M}_n$, $(A,B) \in Q(X_n)$, $n \in \mathbb{N}$;

(Su2) $BSu(f, \mathbf{m}_1) \geq BSu(g, \mathbf{m}_2)$, for all pairs $(f, \mathbf{m}_1) \in \mathcal{S}_{n_1} \times \mathcal{M}_{n_1}$, and $(g, \mathbf{m}_2) \in \mathcal{S}_{n_2} \times \mathcal{M}_{n_2}$, $n_1, n_2 \in \mathbb{N}$ such that (1) is fulfilled for all $t \in]0,1]$.

Finally, let us recall the definition of the bipolar Choquet integral. The bipolar Choquet integral was initially introduced in [8, 10] and studied in [11].

Definition 4 *For $f \in \mathcal{S}$ and $\mathbf{m} \in \mathcal{M}$, the bipolar Choquet integral is defined by*

$$BCh(f, \mathbf{m}) = \sum_{i=1}^{n} (|f_{\alpha(i)}| - |f_{\alpha(i-1)}|) \cdot \mathbf{m}(\{f \geq |f_{\alpha(i)}|\}, \{f \leq -|f_{\alpha(i)}|\}),$$

where a permutation of indexes $\alpha = (\alpha(1), \ldots \alpha(n))$ is related to non-decreasing order of values $|f(x_i)| = |f_i|$, i.e. such that $0 \leq |f_{\alpha(1)}| \leq |f_{\alpha(2)}| \leq \cdots \leq |f_{\alpha(n)}|$, $|f_{\alpha(0)}| = 0$.

The bipolar Choquet integral $BCh: \cup_{n\in\mathbb{N}} \mathcal{S}_n \times \mathcal{M}_n \to [-1,1]$ has the next properties:

(Ch1) $BCh(c \cdot (\chi_{(A,B)}), \mathbf{m}) = c \cdot \mathbf{m}(A,B)$, for all $c \in [0,1]$ and for all $\mathbf{m} \in \mathcal{M}_n$, $(A,B) \in Q(X_n)$, $n \in \mathbb{N}$;

(Ch2) $BCh(f, \mathbf{m}_1) \geq BCh(g, \mathbf{m}_2)$, for all pairs $(f, \mathbf{m}_1) \in \mathcal{S}_{n_1} \times \mathcal{M}_{n_1}$, and $(g, \mathbf{m}_2) \in S_{n_2} \times M_{n_2}$, $n_1, n_2 \in \mathbb{N}$ such that (1) is fulfilled for all $t \in]0,1]$.

By Theorem 2 from [11], the properties (Sh1), (Sh2), (Su1), (Su2), (Ch1) and (Ch2), ensure that each of bipolar integrals

$$BSu, BSh, BCh: \cup_{n\in\mathbb{N}} \mathcal{S}_n \times \mathcal{M}_n \to [-1,1]$$

is the $[-1,1]$-valued bipolar universal integral introduced and studied in [11] (for more details we refer to [7, 8, 10-12]).

3 Jensen Inequality for the Bipolar Shilkret and Sugeno Integrals

In this section, we present the results based on [29]. The Jensen type inequality for the bipolar Shilkret and Sugeno integrals is considered. Further, we will observe conditions under which the reversed Jensen type inequality for these integrals is valid.

We have the following lemma. We refer to [30] for details of its proof.

Lemma 1

(i) For any strictly increasing and odd function φ, $\varphi\colon [-1,1] \to [-1,1]$, *it holds*

$$\varphi(|x|) = |\varphi(x)|.$$

(ii) For any strictly increasing and odd function φ, $\varphi\colon [-1,1] \to [-1,1]$, *and for any* $f \in \mathcal{S}$, *it holds*:

$$\{ f \geq |f_i| \} = \{ \varphi(f) \geq |\varphi(f_i)| \} \quad and \quad \{ f \leq -|f_i| \} = \{ \varphi(f) \leq -|\varphi(f_i)| \},$$

for $i = 1,2, \dots, n$.

(iii) For any strictly increasing function φ, $\varphi\colon [-1,1] \to [-1,1]$, *it holds*

$$\varphi\left(\bigwedge_{i=1}^{n} x_i \right) = \bigwedge_{i=1}^{n} \varphi(x_i) \quad and \quad \varphi\left(\bigvee_{i=1}^{n} x_i \right) = \bigvee_{i=1}^{n} \varphi(x_i),$$

for all $x_i \in [0,1]$, $i = 1, \dots, n$.

(iv) For any function φ, $\varphi\colon [-1,1] \to [-1,1]$, *such that* φ *is a convex function on* $[0,1]$ *and concave on* $[-1,0]$, *and* $\varphi(0) = 0$, *it holds*

$$\varphi(\lambda \cdot x) \leq \lambda \cdot \varphi(x),$$

for all $x \in [0,1]$ *and* $\lambda \in [0,1]$, *and*

$$\varphi(\lambda \cdot x) \geq \lambda \cdot \varphi(x),$$

for all $x \in [-1,0]$ *and* $\lambda \in [0,1]$.

In the following theorem, we consider the Jensen type inequality related to the bipolar Shilkret integral.

Theorem 1 *Let* $\varphi\colon [-1,1] \to [-1,1]$ *be an odd and strictly increasing function, which is convex on* $[0,1]$. *For all* $f \in \mathcal{S}$ *and* $\mathbf{m} \in \mathcal{M}$, *if* $BSh(\varphi(f), \mathbf{m}) \neq 0$, *it holds*

$$\varphi(|BSh(f, \mathbf{m})|) \leq |BSh(\varphi(f), \mathbf{m})|. \tag{2}$$

Proof. The bipolar Shilkret integral can be rewritten as

$$BSh(f, \mathbf{m}) = (\mathcal{S}BSh_{\mathbf{m}}(f)) \bigvee_{i=1}^{n} |f_i| \cdot |\mathbf{m}(\{ f \geq |f_i| \}, \{ f \leq -|f_i| \})|, \tag{3}$$

where, the notation $\mathcal{S}BSh_{\mathbf{m}}(f)$ is used to denote the signum of the bipolar Shilkret integral of f w.r.t. $\mathbf{m}$.

Let us assume that it holds $\mathcal{S}BSh_{\mathbf{m}}(\varphi(f)) \neq 0$. Due to (3) and Lemma 1 (iii), we obtain

$$\begin{aligned}\varphi(|BSh(f,\mathbf{m})|) &= \varphi(\bigvee_{i=1}^{n} |f_i| \cdot |\mathbf{m}(\{f \geq |f_i|\},\{f \leq -|f_i|\})|) \\ &= \bigvee_{i=1}^{n} \varphi(|f_i| \cdot |\mathbf{m}(\{f \geq |f_i|\},\{f \leq -|f_i|\})|).\end{aligned}$$

Further, according to Lemma 1 (iv), (ii) and (i) we have

$$\begin{aligned}\varphi(|BSh(f,\mathbf{m})|) &\leq \bigvee_{i=1}^{n} \varphi(|f_i|) \cdot |\mathbf{m}(\{\varphi(f) \geq |\varphi(f_i)|\},\{\varphi(f) \leq -|\varphi(f_i)|\})| \\ &= \bigvee_{i=1}^{n} |\varphi(f_i)| \cdot |\mathbf{m}(\{\varphi(f) \geq |\varphi(f_i)|\},\{\varphi(f) \leq -|\varphi(f_i)|\})| \\ &= |BSh(\varphi(f),\mathbf{m})|.\end{aligned}$$

□

Corollary 1 *Let $\varphi: [-1,1] \to [-1,1]$, $\varphi(1) = 1$, be an odd and strictly increasing function, which is concave on $[0,1]$. For all $f \in \mathcal{S}$ and $\mathbf{m} \in \mathcal{M}$, if $BSh(f,\mathbf{m}) \neq 0$, it holds*

$$\varphi(|BSh(f,\mathbf{m})|) \geq |BSh(\varphi(f),\mathbf{m})|.$$

Proof. Using the fact that φ^{-1} is odd and strictly increasing on $[-1,1]$ and convex on $[0,1]$, we obtain

$$\varphi^{-1}(|BSh(\varphi(f),\mathbf{m})|) \leq |BSh(\varphi^{-1}(\varphi(f)),\mathbf{m})| = |BSh(f,\mathbf{m})|,$$

thus the claim is valid. □

Notice that the stated inequality holds even if the condition $\varphi(1) = 1$ is omitted.

Example 1 *Let $X = \{x_1, x_2, x_3\}$, $\mathbf{m} \in \mathcal{M}$ such that $\mathbf{m}(\emptyset,\{x_3\}) = -0.5$, $\mathbf{m}(\{x_2\},\{x_3\}) = 0.4$ and $\mathbf{m}(\{x_1,x_2\},\{x_3\}) = 0.6$. Let $f(x_1) = 0$, $f(x_2) = 0.6$, $f(x_3) = -0.8$. By Definition 3, we get:*

$$\begin{aligned}BSh(f,\mathbf{m}) &= (0 \cdot \mathbf{m}(\{x_1,x_2\},\{x_3\})) \vee (0.6 \cdot \mathbf{m}(\{x_2\},\{x_3\})) \vee (0.8 \cdot \mathbf{m}(\emptyset,\{x_3\})) \\ &= (0 \cdot 0.6) \vee (0.6 \cdot 0.4) \vee (0.8 \cdot (-0.5)) \\ &= 0 \vee 0.24 \vee (-0.4) = -0.4.\end{aligned}$$

(i) Let $\varphi(x) = \frac{x}{2-|x|}$, $x \in [-1,1]$. Obviously, φ is convex on $[0,1]$.

$$\varphi(BSh(f,\mathbf{m})) = \frac{-0.4}{2-0.4} = -0.25.$$

Now, compute the related bipolar Shilkret integral of $\varphi(f)$:

$$\begin{aligned}BSh(\varphi(f),\mathbf{m}) &= (\varphi(0) \cdot \mathbf{m}(\{x_1,x_2\},\{x_3\})) \vee (\varphi(0.6) \cdot \mathbf{m}(\{x_2\},\{x_3\})) \\ &\quad \vee (\varphi(0.8) \cdot \mathbf{m}(\emptyset,\{x_3\})) \\ &= (\varphi(0.6) \cdot 0.4) \vee (\varphi(0.8) \cdot (-0.5)) \\ &\approx 0.17143 \vee (-0.33333) = -0.33333.\end{aligned}$$

We have $\varphi(|BSh(f,\mathbf{m})|) = \frac{1}{4} < \frac{1}{3} = |BSh(\varphi(f),\mathbf{m})|$, *i.e. in this case the inequality* (2) *is strict.*

(ii) Let $\varphi(x) = kx,\ x \in [-1,1]$, *where* $0 < k \leq 1$. *We obtain*

$$\varphi(BSh(f,\mathbf{m})) = -0.4k.$$

On the other hand, the bipolar Shilkret integral of a function $\varphi(f)$ *is:*

$$\begin{aligned} BSh(\varphi(f),\mathbf{m}) &= (0 \cdot 0.6) \veebar (0.6k \cdot 0.4) \veebar (0.8k \cdot (-0.5)) \\ &= 0.24k \veebar (-0.4k) \\ &= -0.4k. \end{aligned}$$

In this case, we have the equality $\varphi(|BSh(f,\mathbf{m})|) = |BSh(\varphi(f),\mathbf{m})| = 0.4k$.

(iii) Let $\varphi(x) = \frac{2x}{1+|x|},\ x \in [-1,1]$. *Obviously,* φ *is concave on* $[0,1]$. *We obtain*

$$\varphi(BSh(f,\mathbf{m})) = \frac{2 \cdot (-0.4)}{1 + |-0.4|} = -\frac{4}{7} \approx -0.57143.$$

Now, compute the related bipolar Shilkret integral of $\varphi(f)$:

$$\begin{aligned} BSh(\varphi(f),\mathbf{m}) &= (\varphi(0) \cdot \mathbf{m}(\{x_1,x_2\},\{x_3\})) \veebar (\varphi(0.6) \cdot \mathbf{m}(\{x_2\},\{x_3\})) \\ &\veebar (\varphi(0.8) \cdot \mathbf{m}(\emptyset,\{x_3\})) \\ &= (\varphi(0.6) \cdot 0.4) \veebar (\varphi(0.8) \cdot (-0.5)) \\ &\approx 0.3 \veebar (-0.44444) = -0.44444. \end{aligned}$$

Hence, $\varphi(|BSh(f,\mathbf{m})|) = \frac{4}{7} > \frac{4}{9} = |BSh(\varphi(f),\mathbf{m})|$, *i.e. the inequality given in Corollary 2 is strict.*

Notice that under the conditions given in Theorem 1, if $\mathcal{SBSh}_{\mathbf{m}}(\varphi(f)) = 0$, then the inequality (2) need not be satisfied, that is illustrated in the following example.

Example 2 *Consider* $X = \{x_1,x_2,x_3\}$ *and the function* f *given by* $f(x_1) = \sqrt[5]{0.3}$, $f(x_2) = -\sqrt[5]{0.6}$, $f(x_3) = \sqrt[5]{0.1}$, *and* $\varphi(x) = x^5, x \in [-1,1]$.

(i) Let $\mathbf{m} \in \mathcal{M}$, *such that* $\mathbf{m}(\{x_1,x_3\},\{x_2\}) = 1$, $\mathbf{m}(\{x_1\},\{x_2\}) = 0.8$ *and* $\mathbf{m}(\emptyset,\{x_2\}) = -0.4$. *We have*

$$\begin{aligned} BSh(f,\mathbf{m}) &= (\sqrt[5]{0.3} \cdot \mathbf{m}(\{x_1\},\{x_2\})) \veebar (\sqrt[5]{0.6} \cdot \mathbf{m}(\emptyset,\{x_2\})) \\ &\veebar (\sqrt[5]{0.1} \cdot \mathbf{m}(\{x_1,x_3\},\{x_2\})) \\ &= \left(\sqrt[5]{0.3} \cdot 0.8\right) \veebar (\sqrt[5]{0.6} \cdot (-0.4))\ (\sqrt[5]{0.1} \cdot 1) \\ &\approx 0.62880 \veebar (-0.36115) \veebar 0.63096 \\ &= 0.63096, \end{aligned}$$

thus, $\varphi(BSh(f,\mathbf{m}))=0.1$ *and*

$$\begin{aligned}BSh(\varphi(f),\mathbf{m}) &= (0.3\cdot\mathbf{m}(\{x_1\},\{x_2\}))\ \mathbb{V}\ (0.6\cdot\mathbf{m}(\emptyset,\{x_2\}))\\ &\quad\mathbb{V}\ (0.1\cdot\mathbf{m}(\{x_1,x_3\},\{x_2\}))\\ &= (0.3\cdot 0.8)\ \mathbb{V}\ (0.6\cdot(-0.4))\ \mathbb{V}\ (0.1\cdot 1)\\ &= 0.24\ \mathbb{V}\ (-0.24)\ \mathbb{V}\ 0.1\\ &= 0.\end{aligned}$$

Hence, we have $\varphi(|BSh(f,\mathbf{m})|)>|BSh(\varphi(f),\mathbf{m})|=0$.

(ii) Let $\mathbf{m}\in\mathcal{M}$, *such that* $\mathbf{m}(\{x_2\},\{x_1,x_3\})=-1$, $\mathbf{m}(\{x_2\},\{x_1\})=-0.8$, $\mathbf{m}(\{x_2\},\emptyset)=0.4$, *and* $g=-f$. *We obtain:*

$$\begin{aligned}BSh(g,\mathbf{m}) &= (\sqrt[5]{0.3}\cdot\mathbf{m}(\{x_2\},\{x_1\}))\ \mathbb{V}\ (\sqrt[5]{0.6}\cdot\mathbf{m}(\{x_2\},\emptyset))\\ &\quad\mathbb{V}\ (\sqrt[5]{0.1}\cdot\mathbf{m}(\{x_2\},\{x_1,x_3\}))\\ &= \left(\sqrt[5]{0.3}\cdot(-0.8)\right)\mathbb{V}\ (\sqrt[5]{0.6}\cdot 0.4)\ \mathbb{V}\ (\sqrt[5]{0.1}\cdot(-1))\\ &\approx (-0.62880)\ \mathbb{V}\ 0.36115\ \mathbb{V}\ (-0.63096)=-0.63096,\end{aligned}$$

therefore, $\varphi(BSh(g,\mathbf{m}))=-0.1$ *and*

$$\begin{aligned}BSh(\varphi(g),\mathbf{m}) &= (0.3\cdot\mathbf{m}(\{x_2\},\{x_1\}))\ \mathbb{V}\ (0.6\cdot\mathbf{m}(\{x_2\},\emptyset))\\ &\quad\mathbb{V}\ (0.1\cdot\mathbf{m}(\{x_2\},\{x_1,x_3\}))\\ &= \big(0.3\cdot(-0.8)\big)\ \mathbb{V}\ (0.6\cdot 0.4))\ \mathbb{V}\ (0.1\cdot(-1))\\ &= (-0.24)\ \mathbb{V}\ 0.24\ \mathbb{V}\ (-0.1)=0.\end{aligned}$$

Hence, we have $\varphi(|BSh(g,\mathbf{m})|)>|BSh(\varphi(g),\mathbf{m})|=0$.

(iii) If we take $\varphi(x)=x$, $x\in[-1,1]$, *same* $\mathbf{m}\in\mathcal{M}$ *as that given in (i), and* $h\in\mathcal{M}$, *given by* $h(x_1)=0.3$, $h(x_2)=-0.6$, $h(x_3)=0.1$, *then we get* $\varphi(|BSh(h,\mathbf{m})|)=|BSh(\varphi(h),\mathbf{m})|=0$.

Now, we will observe conditions under which the Jensen type inequality for the bipolar Sugeno integral is valid.

Theorem 2 *Let* $\varphi:[-1,1]\to[-1,1]$ *be an odd and strictly increasing function, such that* $\varphi(x)\le x$ *on* $[0,1]$. *For all* $f\in\mathcal{S}$ *and* $\mathbf{m}\in\mathcal{M}$, *if* $BSu(\varphi(f),\mathbf{m})\neq 0$, *then*

$$\varphi(|BSu(f,\mathbf{m})|)\le|BSu(\varphi(f),\mathbf{m})|.$$

Proof. The bipolar Sugeno integral can be expressed by:

$$BSu(f,\mathbf{m})=(\mathcal{S}BSh_{\mathbf{m}}(f))\bigvee_{i=1}^{n}|f_i|\wedge|\mathbf{m}(\{f\ge|f_i|\},\{f\le-|f_i|\})|, \tag{4}$$

where, the notation $\mathcal{S}BSu_{\mathbf{m}}(f)$ is used to denote the signum of the bipolar Sugeno integral of f w.r.t. $\mathbf{m}$.

Let $\mathcal{S}BSu_{\mathbf{m}}(\varphi(f)) \neq 0$. By (4) and Lemma 1 (iii) we get

$$\begin{aligned}\varphi(|BSu(f,\mathbf{m})|) &= \varphi(\bigvee_{i=1}^{n} |f_i| \wedge |\mathbf{m}(\{f \geq |f_i|\},\{f \leq -|f_i|\})|) \\ &= \bigvee_{i=1}^{n} \varphi(|f_i| \wedge |\mathbf{m}(\{f \geq |f_i|\},\{f \leq -|f_i|\})|) \\ &= \bigvee_{i=1}^{n} \varphi(|f_i|) \wedge \varphi(|\mathbf{m}(\{f \geq |f_i|\},\{f \leq -|f_i|\})|).\end{aligned}$$

Further, due to the condition that $\varphi(x) \leq x$ on $[0,1]$ and Lemma 1 (ii), we have

$$\begin{aligned}\varphi(|BSu(f,\mathbf{m})|) &\leq \bigvee_{i=1}^{n} \varphi(|f_i|) \wedge |\mathbf{m}(\{f \geq |f_i|\},\{f \leq -|f_i|\})| \\ &= \bigvee_{i=1}^{n} |\varphi(f_i)| \wedge |\mathbf{m}(\{\varphi(f) \geq |\varphi(f_i)|\},\{\varphi(f) \leq -|\varphi(f_i)|\})| \\ &= |BSu(\varphi(f),\mathbf{m})|.\end{aligned}$$

□

With a similar consideration as in the proof of Corollary 1, we have the next consequence of Theorem 2.

Corollary 2 *Let $\varphi\colon [-1,1] \to [-1,1]$, $\varphi(1) = 1$, be an odd and strictly increasing function, such that $\varphi(x) \geq x$ on $[0,1]$, which is concave on $[0,1]$. For all $f \in \mathcal{S}$ and $\mathbf{m} \in \mathcal{M}$, if $BSu(f,\mathbf{m}) \neq 0$, it holds*

$$\varphi(|BSu(f,\mathbf{m})|) \geq |BSu(\varphi(f),\mathbf{m})|.$$

Similarly as in the case of the bipolar Shilkret integral, the inequality holds even if the condition $\varphi(1) = 1$ is omitted.

Example 3 *Let us consider f and $\mathbf{m}$ from Example 1.*

(i) Let $\varphi(x) = \text{sign}(x)\ln(1+|x|)$, $x \in [-1,1]$. Obviously, $\varphi(x) \leq x$, for each $x \in [0,1]$. We have

$$\begin{aligned}BSu(f,\mathbf{m}) &= (0 \mathbin{\mathbb{\wedge}} \mathbf{m}(\{x_1,x_2\},\{x_3\})) \mathbin{\mathbb{\vee}} (0.6 \mathbin{\mathbb{\wedge}} \mathbf{m}(\{x_2\},\{x_3\})) \\ &\quad \mathbin{\mathbb{\vee}} (0.8 \mathbin{\mathbb{\wedge}} \mathbf{m}(\emptyset,\{x_3\})) \\ &= (0 \mathbin{\mathbb{\wedge}} 0.6) \mathbin{\mathbb{\vee}} (0.6 \mathbin{\mathbb{\wedge}} 0.4) \mathbin{\mathbb{\vee}} (0.8 \mathbin{\mathbb{\wedge}} (-0.5)) \\ &= 0 \;\; 0.4 \mathbin{\mathbb{\vee}} (-0.5) = -0.5,\end{aligned}$$

and therefore $\varphi(BSu(f,\mathbf{m})) = -\ln(1+0.5) \approx -0.40547$. On the other hand, we have

$$\begin{aligned}BSu(\varphi(f),\mathbf{m}) &= (\varphi(0) \mathbin{\mathbb{\wedge}} 0.6) \mathbin{\mathbb{\vee}} (\varphi(0.6) \mathbin{\mathbb{\wedge}} 0.4) \mathbin{\mathbb{\vee}} \big(\varphi(0.8) \mathbin{\mathbb{\wedge}} (-0.5)\big) \\ &= (0.47 \mathbin{\mathbb{\wedge}} 0.4) \mathbin{\mathbb{\vee}} \big(0.58779 \mathbin{\mathbb{\wedge}} (-0.5)\big) \\ &= 0.4 \mathbin{\mathbb{\vee}} (-0.5) = -0.5.\end{aligned}$$

Hence,

$$\varphi(|BSu(f,\mathbf{m})|) = 0.40547 \leq 0.5 = |BSu(\varphi(f),\mathbf{m})|,$$

i.e. the inequality stated in Theorem 2 is fulfilled.

(ii) Let $\varphi(x) = \frac{2x}{1+|x|}$, $x \in [-1,1]$. *Obviously,* $\varphi(x) \geq x$, *for each* $x \in [0,1]$.

We have $\varphi(BSu(f,\mathbf{m})) = \frac{2\cdot(-0.5)}{1+|-0.5|} = -\frac{2}{3}$ *and*

$$\begin{aligned} BSu(\varphi(f),\mathbf{m}) &= (\varphi(0) \mathbb{\wedge} 0.6) \mathbb{\vee} (\varphi(0.6) \mathbb{\wedge} 0.4) \mathbb{\vee} \left(\varphi(0.8) \mathbb{\wedge} (-0.5)\right) \\ &\approx (0.75 \mathbb{\wedge} 0.4) \mathbb{\vee} \left(0.88889 \mathbb{\wedge} (-0.5)\right) \\ &= 0.4 \mathbb{\vee} (-0.5) = -0.5. \end{aligned}$$

Hence,

$$\varphi(|BSu(f,\mathbf{m})|) = \frac{2}{3} \geq \frac{1}{2} = |BSu(\varphi(f),\mathbf{m})|,$$

i.e. the inequality stated in Corollary 2 is fulfilled.

Similarly as in Example 2 with the bipolar Shilkret integral, under the conditions of Theorem 2, if $\mathcal{SBSU}_{\mathbf{m}}(\varphi(f)) = 0$, the reversed inequality holds (see Example 10 in [29]):

$$\varphi(|BSu(f,\mathbf{m})|) \geq |BSu(\varphi(f),\mathbf{m})| = 0.$$

4 Jensen Inequality for the Bipolar Choquet Integral

The bipolar Choquet integral is the most prominent member of the class of bipolar Choquet g-integrals introduced in [17]. Therefore, based on [17], in this section, the Jensen type inequality for the bipolar Choquet integral is considered. Here, we will give the complete proof of the main theorem, and present the conditions under which the reversed Jensen type inequality for this integral is valid.

For $f \in \mathcal{S}$, denote

$$X^+ = \{x_i \in X \mid f(x_i) > 0\}, \qquad X^- = \{x_i \in X \mid f(x_i) < 0\},$$
$$X^0 = \{x_i \in X \mid f(x_i) = 0\}, \quad supp(f) = X^+ \cup X^- = X \backslash X^0,$$
$$X^{+0} = X^+ \cup X^0 \text{ and } X^{-0} = X^- \cup X^0.$$

Let $\mathbf{m} \in \mathcal{M}$ and $f \in \mathcal{S}$. Define set functions $\mu_{f^+}, \tilde{\mu}_{f^+} : \mathcal{P}(X) \to [-1,1]$ by

$$\mu_{f^+}(A) = \mathbf{m}(A \cap X^{+0}, A \cap X^-) \tag{5}$$

$$\tilde{\mu}_{f^+}(A) = \mathbf{m}(A \cap X^+, A \cap X^{-0}). \tag{6}$$

Let $\widehat{\mathbf{m}}(A,B) = -\mathbf{m}(B,A)$, for all $(A,B) \in Q(X)$. First, by Definition 2 it can be easily verified that $\widehat{\mathbf{m}} \in \mathcal{M}$. Further, for all $A \in \mathcal{P}(X)$ we have:

$$\mu_{f^+}(A) = -\hat{\mu}_{(-f)^+}(A), \text{ if } A \subset supp(f); \tag{7}$$

$$\mu_{f^+}(A) = -\tilde{\tilde{\mu}}_{(-f)^+}(A). \tag{8}$$

Obviously, any function $f \in \mathcal{S}$ can be expressed by:

$$f = \sum_{i=1}^{n} (|f_{\alpha(i)}| - |f_{\alpha(i-1)}|) \cdot \chi_{(A_i \cap X^{+0}, A_i \cap X^-)}$$
$$= \sum_{i=1}^{n} (|f_{\alpha(i)}| - |f_{\alpha(i-1)}|) \cdot \chi_{(A_i \cap X^+, A_i \cap X^{-0})},$$

where $|f_{\alpha(i)}| \leq |f_{\alpha(j)}|$, for all $i \leq j$, $f_{\alpha(0)} = 0$, and $A_i = \{x_{\alpha(i)}, \dots, x_{\alpha(n)}\}$, $i = 1, \dots, n$.

Now, for computing the bipolar Choquet integral we can use the formula from the next proposition.

Proposition 1 *Let $\varphi: [-1,1] \to [-1,1]$ be odd and strictly increasing function, $f \in \mathcal{S}$, $\varphi(f) = \varphi \circ f \in \mathcal{S}$ and $\mathbf{m} \in \mathcal{M}$. Then:*

$$BCh(\varphi(f), \mathbf{m}) = \sum_{i=1}^{n} (\varphi(|f_{\alpha(i)}|) - \varphi(|f_{\alpha(i-1)}|)) \cdot \mu_{f^+}(A_i) \tag{9}$$

$$= \sum_{i=1}^{n} (\varphi(|f_{\alpha(i)}|) - \varphi(|f_{\alpha(i-1)}|)) \cdot \tilde{\mu}_{f^+}(A_i) \tag{10}$$

$$= \sum_{i=1}^{n} \varphi(|f_{\alpha(i)}|) \cdot (\mu_{f^+}(A_i) - \mu_{f^+}(A_{i+1})), \tag{11}$$

for any permutation α of indexes such that $|f_{\alpha(i)}| \leq |f_{\alpha(j)}|$, for all $i \leq j$, $f_{\alpha(0)} = 0$, $A_i = \{x_{\alpha(i)}, \dots, x_{\alpha(n)}\}$, $i = 1, \dots, n$, and $A_{n+1} = \emptyset$.

Proof. Let $f \in \mathcal{S}$ and $\mathbf{m} \in \mathcal{M}$. Let φ be odd and strictly increasing and $\varphi(f) = \varphi \circ f \in \mathcal{S}$. For an arbitrary permutation of indexes α, such that $|f_{\alpha(i)}| \leq |f_{\alpha(j)}|$, for all $i \leq j$, $f_{\alpha(0)} = 0$, let $K = \{j \mid |f_{\alpha(j)}| \neq |f_{\alpha(j-1)}|\}$. For all $i \in K$, we get:

$$\mathbf{m}(\{f \geq |f_{\alpha(i)}|\}, \{f \leq -|f_{\alpha(i)}|\}) = \mu_{f^+}(A_i) = \tilde{\mu}_{f^+}(A_i).$$

By Lema 1, we have $\varphi(0) = 0$, $\varphi(|x|) = |\varphi(x)|$, for all $x \in [-1,1]$, and $\mu_{f^+} = \mu_{(\varphi \circ f)^+}$. Therefore

$$BCh(\varphi(f), \mathbf{m}) = \sum_{i \in K} (|\varphi(f_{\alpha(i)})| - |\varphi(f_{\alpha(i-1)})|) \cdot \mu_{(\varphi \circ f)^+}(A_i)$$
$$= \sum_{i \in K} (\varphi(|f_{\alpha(i)}|) - \varphi(|f_{\alpha(i-1)}|)) \cdot \mu_{f^+}(A_i)$$
$$= \sum_{i=1}^{n} (\varphi(|f_{\alpha(i)}|) - \varphi(|f_{\alpha(i-1)}|)) \cdot \mu_{f^+}(A_i)$$
$$= \sum_{i=1}^{n} \varphi(|f_{\alpha(i)}|) \cdot (\mu_{f^+}(A_i) - \mu_{f^+}(A_{i+1})),$$

where $A_i = \{x_{\alpha(i)}, \dots, x_{\alpha(n)}\}$, for $i \geq 2$, $A_1 = X$, $A_{n+1} = \emptyset$. Hence, (9) and (11) are valid. Due to $\mu_{f^+}(A) = \tilde{\mu}_{f^+}(A)$, for all $A \subset supp(f)$, we obtain (10). □

Example 4 *([17]) Consider* $X = \{x_1, x_2, x_3, x_4\}$ *and* $f: X \to [-1,1]$ *such that* $f(x_1) = 0.2$, $f(x_2) = -0.2$, $f(x_3) = 0, f(x_4) = -0.4$. *Obviously, we get* $X^{+0} = \{x_1, x_3\}$, $X^- = \{x_2, x_4\}$. *Let* $\mathbf{m} \in \mathcal{M}$, $card(Q(X)) = 3^4 = 81$.

Consider $\varphi(x) = x^k$, $x \in \mathbb{R}$, for odd $k \in \mathbb{N}$. For $\alpha_1 = (3,1,2,4)$, we have $|\varphi(f_3)| \leq |\varphi(f_1)| \leq |\varphi(f_2)| \leq |\varphi(f_4)|$. Using Proposition 1, we get:

$$\begin{aligned} BCh(\varphi(f), \mathbf{m}) = \\ = (|0| - |0|) \cdot \mu_{f^+}(\{x_3, x_1, x_2, x_4\}) + (|0.2|^k - |0|) \cdot \mu_{f^+}(\{x_1, x_2, x_4\}) + \\ +(|-0.2|^k - |0.2|^k) \cdot \mu_{f^+}(\{x_2, x_4\}) + (|-0.4|^k - |-0.2|^k) \cdot \mu_{f^+}(\{x_4\}) \\ = |0.2|^k \cdot \mu_{f^+}(\{x_1, x_2, x_4\}) + (|-0.4|^k - |-0.2|^k) \cdot \mu_{f^+}(\{x_4\}). \end{aligned}$$

For $\alpha_2 = (3,2,1,4)$, $\alpha_1 \neq \alpha_2$, it holds $|\varphi(f_3)| \leq |\varphi(f_2)| \leq |\varphi(f_1)| \leq |\varphi(f_4)|$, and by Proposition 1, we obtain the same result:

$$\begin{aligned} BCh(\varphi(f), \mathbf{m}) = \\ = (|-0.2|^k - |0|) \cdot \mu_{f^+}(\{x_2, x_1, x_4\}) + (|-0.4|^k - |0.2|^k) \cdot \mu_{f^+}(\{x_4\}) \\ = |-0.2|^k \cdot \mu_{f^+}(\{x_2, x_1, x_4\}) + (|-0.4|^k - |0.2|^k) \cdot \mu_{f^+}(\{x_4\}). \end{aligned}$$

Notice that $\mu_{f^+}(\{x_2, x_1, x_4\}) = \mu_{f^+}(\{x_1, x_2, x_4\}) = \mathbf{m}(\{x_1\}, \{x_2, x_4\})$ and $\mu_{f^+}(\{x_4\}) = \mathbf{m}(\emptyset, \{x_4\})$.

It should be noticed that by Proposition 1, for $\varphi(x) = x$, $x \in [-1,1]$, for $f \in \mathcal{S}$, $\mathbf{m} \in \mathcal{M}$, with α and A_i previously described, we have:

$$BCh(f, \mathbf{m}) = \sum_{i=1}^{n} |f_{\alpha(i)}| \cdot \left(\mu_{f^+}(A_i) - \mu_{f^+}(A_{i+1})\right). \tag{12}$$

Now, the proof of the next claim easily follows from (12) and (7).

Proposition 2 *([17]) Let* $f \in \mathcal{S}$ *and* $\mathbf{m} \in \mathcal{M}$. *Then*

$$BCh(-f, \mathbf{m}) = -BCh(f, \widehat{\mathbf{m}}),$$

where $\widehat{\mathbf{m}} \in \mathcal{M}$ is given by $\widehat{\mathbf{m}}(A, B) = -\mathbf{m}(B, A)$, for all $(A, B) \in Q(X)$.

Jensen type inequality for the bipolar Choquet integral is presented in the next theorem. Here, we give its complete proof. Very recently, the similar proving technic has been presented in [16], however, the following result is more general in the sense that the underlining set functions μ_{f^+} and $\tilde{\mu}_{f^+}$ given by (5) and (6) associated to a bi-capacity need not to be the difference of two fuzzy measures.

Theorem 3 *Let* $\varphi: [-1,1] \to [-1,1]$ *be an odd and strictly increasing function, such that it is convex on* $[0,1]$, *and* $c > 0$. *Let* $f \in \mathcal{S}$ *and* $\mathbf{m} \in \mathcal{M}$. *If there exists a permutation* α *of indexes such that* $|f_{\alpha(i)}| \leq |f_{\alpha(j)}|$, *for all* $i \leq j$, *and for all* $i, j = 1, \dots, n$ *it holds* $\mu_{f^+}(A_i)\mu_{f^+}(A_j) \geq 0$, $|\mu_{f^+}(A_i)| \leq c$ *and* $|\mu_{f^+}(A_1)| = c$ *or* $\tilde{\mu}_{f^+}(A_i)\tilde{\mu}_{f^+}(A_j) \geq 0$, $|\tilde{\mu}_{f^+}(A_i)| \leq c$ *and* $|\tilde{\mu}_{f^+}(A_1)| = c$, *where* $A_i = \{x_{\alpha(i)}, \dots, x_{\alpha(n)}\}$, *then*

$$\varphi\left(\frac{1}{c}\cdot|BCh(f,\mathbf{m})|\right)\leq\frac{1}{c}\cdot|BCh(\varphi(f),\mathbf{m})|.$$

Proof. Let $f\in\mathcal{S}$ and $\mathbf{m}\in\mathcal{M}$. Let α be desired permutation. We have two possible cases:

Case I For all $i=1,\dots,n$ it holds $0\leq\mu_{f^+}(A_i)\leq c$ and $\mu_{f^+}(A_1)=c>0$ or $0\leq\tilde{\mu}_{f^+}(A_i)\leq c$ and $\tilde{\mu}_{f^+}(A_1)=c>0$. By Proposition 1, in both subcases we get $BCh(\varphi(f),\mathbf{m})\geq 0$ and $BCh(f,\mathbf{m})\geq 0$ and if we suppose $BCh(\varphi(f),\mathbf{m})=0$, then it follows $BCh(f,\mathbf{m})=0$.

Now, suppose that $BCh(\varphi(f),\mathbf{m})>0$ and for all $i=1,\dots,n$ it holds $0\leq\mu_{f^+}(A_i)\leq c$ and $\mu_{f^+}(A_1)=c>0$. By Proposition 1 we have $\varphi(\frac{1}{c}|BCh(f,\mathbf{m})|)=\varphi(\frac{1}{c}BCh(f,\mathbf{m}))$

$$\begin{aligned}
&=\varphi\left(\tfrac{1}{c}\textstyle\sum_{i=1}^{n}|f_{\alpha(i)}|\cdot\left(\mu_{f^+}(A_i)-\mu_{f^+}(A_{i+1})\right)\right)\\
&=\varphi\left(\textstyle\sum_{i=1}^{n}|f_{\alpha(i)}|\cdot\left(\frac{\mu_{f^+}(A_i)}{c}-\frac{\mu_{f^+}(A_{i+1})}{c}\right)\right)\\
&\leq\textstyle\sum_{i=1}^{n}\varphi(|f_{\alpha(i)}|)\cdot\left(\frac{\mu_{f^+}(A_i)}{c}-\frac{\mu_{f^+}(A_{i+1})}{c}\right)\\
&=\tfrac{1}{c}\textstyle\sum_{i=1}^{n}|\varphi(f_{\alpha(i)})|\cdot\left(\mu_{f^+}(A_i)-\mu_{f^+}(A_{i+1})\right)\\
&=\frac{1}{c}\cdot BCh(\varphi(f),\mathbf{m})\\
&=\frac{1}{c}\cdot|BCh(\varphi(f),\mathbf{m})|,
\end{aligned}$$

where the inequality holds based on the well-known Jensen's type inequality for ordered weighted means with real weights p_i, such that $0\leq\sum_{i=1}^{k}p_i\leq 1$, for all $k=1,\dots,n-1$ and $\sum_{i=1}^{n}p_i=1$ (see, e.g. [3, 17, 23, 30]).

Analogously we obtain the claim in the second subcase, i.e. if for all $i=1,\dots,n$ it holds $0\leq\tilde{\mu}_{f^+}(A_i)\leq c$ and $\tilde{\mu}_{f^+}(A_1)=c>0$.

Case II For all $i=1,\dots,n$ it holds $-c\leq\mu_{f^+}(A_i)\leq 0$ and $\mu_{f^+}(A_1)=-c<0$ or $-c\leq\tilde{\mu}_{f^+}(A_i)\leq 0$ and $\tilde{\mu}_{f^+}(A_1)=-c<0$. In both subcases, by Proposition 1, we obtain $BCh(\varphi(f),\mathbf{m})\leq 0$ and $BCh(f,\mathbf{m})\leq 0$. Therefore

$$|BCh(\varphi(f),\mathbf{m})|=-BCh(\varphi(f),\mathbf{m}),\quad\text{and}\quad|BCh(f,\mathbf{m})|=-BCh(f,\mathbf{m}).$$

Moreover, if $BCh(\varphi(f),\mathbf{m})=0$, then $BCh(f,\mathbf{m})=0$.

Further, suppose $BCh(\varphi(f),\mathbf{m})<0$ and for all $i=1,\dots,n$ it holds $-c\leq\mu_{f^+}(A_i)\leq 0$ and $\mu_{f^+}(A_1)=-c<0$. By (8) it follows that for all $i=1,\dots,n$ it holds $0\leq\tilde{\tilde{\mu}}_{(-f)^+}(A_i)\leq c$ and $\tilde{\tilde{\mu}}_{(-f)^+}(A_1)=c>0$. Now, from Case I we obtain

$$\varphi(\frac{1}{c}\cdot|BCh(-f,\widehat{\mathbf{m}})|)\leq\frac{1}{c}\cdot|BCh(\varphi(-f),\widehat{\mathbf{m}})|.$$

Finally, by Proposition 2 and the previous inequality, we get

$$\begin{aligned}\varphi\left(\frac{1}{c}|BCh(f,\mathbf{m})|\right) &= \varphi\left(\frac{1}{c}\cdot BCh(-f,\widehat{\mathbf{m}})\right)\\ &= \varphi\left(\tfrac{1}{c}\cdot|BCh(-f,\widehat{\mathbf{m}})|\right)\\ &\le \tfrac{1}{c}\cdot|BCh(\varphi(-f),\widehat{\mathbf{m}})|\\ &= \tfrac{1}{c}\cdot|BCh(\varphi(f),\mathbf{m})|.\end{aligned}$$

Analogously we obtain the claim in the second subcase, i.e. if for all $i=1,\dots,n$ it holds $-c\le\tilde{\mu}_{f^+}(A_i)\le 0$ and $\tilde{\mu}_{f^+}(A_1)=-c<0$. □

We have the next consequence of the previous theorem.

Corollary 3 *Let $\varphi:[-1,1]\to[-1,1]$, $\varphi(1)=1$, be an odd and strictly increasing function, such that it is concave on $[0,1]$, and $c>0$. Let $f\in\mathcal{S}$ and $\mathbf{m}\in\mathcal{M}$. If there exists a permutation α of indexes such that $|f_{\alpha(i)}|\le|f_{\alpha(j)}|$, for all $i\le j$, and for all $i,j=1,\dots,n$ it holds $\mu_{f^+}(A_i)\mu_{f^+}(A_j)\ge 0$, $|\mu_{f^+}(A_i)|\le c$ and $|\mu_{f^+}(A_1)|=c$ or $\tilde{\mu}_{f^+}(A_i)\tilde{\mu}_{f^+}(A_j)\ge 0$, $|\tilde{\mu}_{f^+}(A_i)|\le c$ and $|\tilde{\mu}_{f^+}(A_1)|=c$, where $A_i=\{x_{\alpha(i)},\dots,x_{\alpha(n)}\}$, then*

$$\varphi\left(\tfrac{1}{c}\cdot|BCh(f,\mathbf{m})|\right)\ge\tfrac{1}{c}\cdot|BCh(\varphi(f),\mathbf{m})|. \tag{13}$$

Proof. The claim follows from the fact that φ^{-1} is odd and strictly increasing on $[-1,1]$ and convex on $[0,1]$. □

The last example shows that (13) holds even if the condition $\varphi(1)=1$ is omitted. Notice that if φ is odd, strictly decreasing on $[-1,1]$, $\varphi(1)=-1$, and concave (convex) on $[0,1]$, then $\varphi(|x|)\in[-1,0]$, and $-\varphi$ ($-\varphi^{-1}$ resp.) is odd, strictly increasing on $[-1,1]$ and convex on $[0,1]$. Therefore, as consequences of Theorem 3, we have:

$$\varphi\left(\tfrac{1}{c}\cdot|BCh(f,\mathbf{m})|\right)\underset{(\le)}{\ge}-\tfrac{1}{c}\cdot|BCh(\varphi(-f),\mathbf{m})|.$$

Example 5 *([17]) Let $X=\{x_1,x_2,x_3,x_4\}$ and $\varphi(x)=sign(x)\left(1-e^{-|x|}\right)$, $x\in[-1,1]$, concave on $[0,1]$. Let $f\in$ be $\mathcal{S}$ defined by $f(x_1)=-0.2$, $f(x_2)=0.4$, $f(x_3)=-0.6$, and $f(x_4)=0.8$. We have $|f(x_1)|\le|f(x_2)|\le|f(x_3)|\le|f(x_4)|$, and corresponding A_i and $\mu_{f^+}(A_i)$ are given in Table 1.*

Table 1
Corresponding A_i and $\mu_{f^+}(A_i)$ for α=(1,2,3,4)

$\alpha(i)$	1	2	3	4
$\lvert f_{\alpha(i)}\rvert$	0.2	0.4	0.6	0.8
A_i	X	$\{x_2, x_3, x_4\}$	$\{x_3, x_4\}$	$\{x_4\}$
$\mu_f+(A_i)$	0.6	0.6	0.2	0.4

We compute:

$$\varphi\left(\frac{1}{0.6}\cdot BCh(f,\mathbf{m})\right)=\varphi\left(\frac{1}{0.6}\cdot((0.2-0)\cdot 0.6+(0.4-0.2)\cdot 0.6+\right.$$
$$\left.+(0.6-0.4)\cdot 0.2+(0.8-0.6)\cdot 0.4)\right)$$
$$=1-e^{-\frac{0.36}{0.6}}\approx 0.45119;$$

$$\frac{1}{0.6}\cdot BCh(\varphi(f),\mathbf{m})=\frac{1}{0.6}\cdot((\varphi(0.2)-\varphi(0))\cdot 0.6+(\varphi(0.4)-\varphi(0.2))\cdot 0.6+$$
$$+(\varphi(0.6)-\varphi(0.4))\cdot 0.2+(\varphi(0.8)-\varphi(0.6))\cdot 0.4)$$
$$=\frac{1}{0.6}\cdot((1-e^{-0.2})\cdot 0.6+(e^{-0.2}-e^{-0.4})\cdot 0.6+$$
$$+(e^{-0.4}-e^{-0.6})\cdot 0.2+(e^{-0.6}-e^{-0.8})\cdot 0.4)\approx 0.43650.$$

Therefore, $\varphi\left(\frac{1}{0.6}\cdot|BCh(f,\mathbf{m}|)\right)\geq\frac{1}{0.6}\cdot|BCh(\varphi(f,\mathbf{m}))|$, i.e. the inequality (13) is satisfied.

Conclusions

The Jensen type inequality for the discrete bipolar Choquet, Sugeno and Shilkret integrals with respect to normalized bi-capacities have been proven. The main results are in accordance with the Jensen type inequality for the bipolar pseudo-integrals presented in [30] and with the corresponding inequality for CPT-like integrals studied in the framework of principles for premium calculation in [16]. In the case of non-negative functions, the obtained results are in accordance with the corresponding inequality for the Sugeno integral obtained in [21] and the inequality for Choquet integral studied in [15, 16]. For the first time in the literature dealing with bipolar integrals, the Jensen type of inequality was considered in the recent paper [30]. Therefore, in the future work the application of the obtained results in decision-making problems will be studied.

Acknowledgment

The authors acknowledge the financial support of the Ministry of Education, Science and Technological Development of the Republic of Serbia (the first author: project "Innovative scientific and artistic research from the FTS (activity) domain" Grant No. 451-03-68/2020-14/200156, the second author: Grant No. 451-03-9/2021-14/ 200125).

References

[1] S. Abbaszadeh, M. E. Gordji, E. Pap, A. Szakál: Jensen-type inequalities for Sugeno integral, Inf. Sci. 376 (2017) 148-157

[2] H. Agahi, R. Mesiar, A. Babakhani: Generalized expectation with general kernels on g-semirings and its applications, RACSAM 111 (2017) 863-875

[3] P. S. Bullen: Accentuate the negative, Math. Bohem. 134 (2009) 427-446

[4] D. Denneberg: Non-Additive Measure and Integral, Kluwer Academic, Dordrecht, 1994

[5] G. Choquet: Theory of capacities, Ann. Inst. Fourier 5 (1953/54) 131-295

[6] M. Grabisch: Set Functions, Games and Capacities in Decision Making, Springer, Cham, 2016

[7] M. Grabisch, C. Labreuche: Bi-capacities, Part I: definition, Möbius transform and interaction, Fuzzy Sets Syst. 151 (2005) 211-236

[8] M. Grabisch, C. Labreuche: Bi-capacities, Part II: the Choquet integral, Fuzzy Sets Syst. 151 (2005) 237-259

[9] M. Grabisch, J. L. Marichal, R. Mesiar, Pap, E.: Aggregation Functions (Encyclopedia of Mathematics and its Applications) Cambridge University Press 2009

[10] S. Greco, B. Matarazzo, R. Slowinski: Bipolar Sugeno and Choquet integrals, in: G. Pasi B. De Baets, J. Fodor (Eds.), Workshop on Information Systems (EURO-FUSE 2002), Varenna, Italy (2002) 191-196

[11] S. Greco, R. Mesiar, F. Rindone: Discrete bipolar universal integrals, Fuzzy Sets Syst. 252 (2014) 55-65

[12] S. Greco, F. Rindone: Bipolar fuzzy integrals, Fuzzy Sets Syst. 220 (2013) 21-33

[13] M. Kaluszka, A. Okolewski, M. Boczek: On the Jensen type inequality for generalized Sugeno integral, Inf. Sci. 266 (2014) 140-147

[14] P. Karczmarek, A. Kiersztyn, W. Pedrycz: Generalized Choquet integral for face recognition, Int. J. Fuzzy Syst. 20 (2018) 1047-1055

[15] R. Mesiar, J. Li, E. Pap: The Choquet integral as Lebesgue integral and related inequalities, Kybernetika 46 (2010) 1098-1107

[16] B. Mihailović, E. Pap, M. Štrboja, A. Simićević: A unified approach to the monotone integral-based premium principles under the CPT theory, Fuzzy Sets and Syst. 398 (2020) 78-97

[17] B. Mihailović, M. Štrboja, M. Todorov: The bipolar Choquet g-integrals, in: Proceedings of 17th IEEE International Symposium on Intelligent Systems and Informatics, Subotica (2019) 173-178

[18] E. Pap: Null-Additive Set Functions, Kluwer Academic Publishers, Dordrecht- Boston-London, 1995

[19] E. Pap (ed.): Handbook of Measure Theory, Elsevier Science, Amsterdam, 2002

[20] E. Pap, M. Štrboja: Generalization of the Jensen inequality for pseudo-integral, Inf. Sci. 180 (2010) 543-548

[21] H. Román-Flores, A. Franulič, Chalko-Cano: A Jensen type inequality for fuzzy integrals, Inf. Sci. 177 (2007) 3192-3201

[22] N. Shilkret: Maxitive measure and integration, Indag. Math. 74 (1971) 109-116

[23] J. F. Steffensen: On certain inequalities and methods of approximation, J. Inst. Actuar. 51 (1919) 274-297

[24] M. Štrboja, B. Mihailović: Generalized Minkowski type inequality for pseudo-integral, Math. Slovaca 71(1) (2021) 57-74

[25] M. Štrboja, E. Pap, B. Mihailović: Discrete bipolar pseudo-integrals, Inf. Sci. 468 (2018) 72-88

[26] M. Sugeno: Theory of Fuzzy Integrals and its Applications, Ph.D. Thesis, Tokyo Institute of Technology, 1974

[27] M. Sugeno, T. Murofushi: Pseudo-additive measures and integrals, J. Math. Anal. Appl. 122 (1987) 197-222

[28] M. Todorov, M. Štrboja, B. Mihailović: Bi-capacities based pan-integral, in: Proceedings of 16th IEEE International Symposium on Intelligent Systems and Informatics, Subotica, Serbia (2018) 301-304

[29] M. Todorov, M. Štrboja, B. Mihailović: Jensen type inequality for the bipolar Shilkret and Sugeno integrals, in: Proceedings of 17th IEEE International Symposium on Intelligent Systems and Informatics, Subotica (2019) 179-184

[30] M. Todorov, M. Štrboja, E. Pap, B. Mihailović: Jensen type inequality for the bipolar pseudo-integrals, Fuzzy Sets and Syst. 379 (2020) 82-101

[31] A. Tversky, D. Kahmenam: Advances in prospect theory. Cumulative representation of uncertanity, J. of Risk and Uncertanity 5 (1992) 297-323

Ontological Approach to Automated Analysis of Enterprise Data Storage Systems Log Files

Olga Mamoutova, Mikhail Uspenskiy, Sergey Smirnov, Marina Bolsunovskaya

Peter the Great St. Petersburg Polytechnic University, Polytechnicheskaya st. 29, 194021 St. Petersburg, Russia; {olga.mamoutova, mikhail.uspenskiy, sergey.smirnov, marina.bolsunovskaia}@spbpu.com

Abstract: Enterprise data storage is usually designed to operate as a highly available system, which needs continuous monitoring and diagnosing of a system state. However, applying the traditional approach to administration tasks with manual analysis of event log files is infeasible due to the complexity of such systems. Multiple levels of monitoring and the heterogeneous nature of diagnostic data require an autonomous solution that provides a combination of model-based, knowledge-based and data-based approaches. An ontology-based diagnostic model, that integrates an expert knowledge of diagnostic parameters, typical storage configurations, and common failure modes, can be considered a promising solution for this task. The implementation goal for such an autonomous diagnostic approach would be not to substitute, but to complement existing diagnostic infrastructure. Hence, software and system event log files can be viewed as additional diagnostic data to be analyzed. This paper presents a new approach to event log analysis, which is supported by the ontology-based diagnostic model: structure of supporting ontology classes, text preparation algorithm, key implementation points, and assessments of the data mining algorithm suitability for the task.

Keywords: data storage system; diagnostic model; knowledge-based systems; ontology; event log; data mining

1 Introduction

Companies, which use data storage systems for business-sensitive data, require seamless service delivery and have zero tolerance for data loss, loss of service, and performance degradation [1]. A reason for a data storage system failure can be a hardware component fault, software error, or misconfiguration. As a result, a data storage system usually employs a combination of redundancy techniques and implements a health and fault management strategy to detect and diagnose developing issues and provide access to the data in presence of a possible failure [2].

A typical configuration of an enterprise data storage system includes several enclosures with drives to store data, a cluster of storage controllers to manage user requests and perform service functions, and network infrastructure to connect users, storage controllers and drives [3]. To provide the necessary diagnostic data, continuous monitoring must be performed at all levels of a data storage system. The lowest level of monitoring gets diagnostic data from terminal sources with no data regarding causes of reported states: built-in self-test functions or embedded sensors data. Some examples of such data are S.M.A.R.T. or SCSI diagnostic data for disks, signal quality for a network transceiver, fan speed, and temperature readings. For the next, system-level, monitoring, a hierarchy of distributed tools gathers monitoring data across hardware and software components of the lowest level to get a full operational picture of the system: components health reports, ambient parameters, network performance readings, as well as metrics of storage and computing nodes workload, performance, capacity, and power consumption. Finally, a file or block-level performs service-level monitoring across the corresponding physical, virtual and, if present, cloud components.

Such health and performance monitoring is usually executed by a combination of vendor-specific and third-party software. Monitoring tools gather data by polling status data and recording alarms, errors, and miscellaneous messages. Machine-learning techniques for anomaly detection can provide additional data for analysis. Further diagnostic tasks include error and event correlation, Root Cause Analysis (RCA), and deciding on necessary management procedures. Because of the heterogeneous nature of a diagnostic data and because these diagnostic tasks require a detailed understanding of a system architecture, field experience, and best practices knowledge, diagnostics are primarily performed by an administrator [3]. As a result, monitoring data are often stored in the form of human-readable log files. Section 2 gives a review of current monitoring and diagnostic practices.

The embedded ontological approach is a way towards automation of the diagnostic procedures in a data storage system. Applying autonomous monitoring and embedded diagnostics as part of a self-management strategy for a storage processor results in a faster real-time fault detection as opposed to reactive administrator intervention. When using the presented ontological approach, a hybrid diagnostic model of a particular system is created, including an unstructured heterogeneous expert knowledge in a formalized form, an explicit white-box like reliability model of the data storage system and a black-box-like model in the form of pre-trained machine learning algorithms. Section 3 contains the key details regarding the implementation of the ontological approach. Section 4 contains the details regarding the application of the approach with the traditional event log data.

The scientific contribution of the presented research is the ontological approach that allows to create a sophisticated, but flexible and easily upgradable diagnostic solutions for data storage systems despite a wide range of possible faults of varying origin and importance. This paper extends the work originally presented

in the 17th IEEE International Symposium on Intelligent Systems and Informatics [4] and aims to provide a thorough description of the suggested ontological approach, methods to define symptoms, and its application in case of event log files as monitoring data. It provides results and recommendations based on practical evaluation of the approach for a medium-sized enterprise data storage system.

2 Related Work

2.1 Methods of Data Analysis for Data Storage Diagnostics

Identifying occurring or emerging problems in the form of an event or performance deviation is the first step of diagnosing, which needs the details of logical or physical entities of a system. Storage resource management tools [5] provide an administrator of a data storage system with necessary remote monitoring and diagnosis services: dashboarding, thresholding, and custom policy configuration [6]. Some tools additionally perform data-driven anomaly detection [7-9].

The next step is RCA to diagnose the cause of the detected problem, which allows deciding on further management actions. One way to perform RCA is to manually trace down the history of events in error and configuration log files. A monitoring tool can assist in this task by mapping the detected problem to the network topology, searching for event correlations, and showing the related resources. However, for networks alone, RCA is a challenging task [10], and adding hosts, power supply and storage devices to the systems only adds to its complexity, resulting in hundreds of event types that demand administrator attention. Hence, manual RCA becomes impractical.

An example of automated RCA is IPASS algorithm for Storage Area Networks (SAN) [11], which reconstructs I/O paths and performs an informed search for the root cause of a performance problem. IPASS requires a graph representation of a SAN, which could not be reused as a diagnostic model for another SAN or other data storage system. Another limitation is that IPASS uses only performance metrics and does not account for the health or capacity metrics of the network nodes.

Another example is RCA implemented for IT environments in eG Enterprise [12]. This RCA algorithm discovers dependencies and connections between system components with corresponding health metrics, then creates pairs of relational maps and dataflow graphs to describe them and searches for correlations among connected or dependent problematic components. This approach has a visibility

limitation as it operates at the application level and does not take into account the internal structure of the devices, which limits its insight into problems.

The new approach, presented in this paper, aims to solve the problem of automatic RCA by implementing an embedded service that runs on a storage processor. Such embedded diagnostic leverages visibility of internal organization of a data storage system and allows a storage processor to perform real-time diagnosis and self-management. Furthermore, the new approach uses an ontology to solve the problem of constructing a diagnostic model for arbitrary data storage systems with various redundancy schemes and types of monitoring data and also to introduce heterogeneous expert knowledge into the model.

2.2 Ontologies for Diagnostics

In computer science, ontology is a type of knowledge representation model that is able to formally specify a shared knowledge in a certain subject area. Concepts, objects, and relations between them can be described by a hierarchy of classes and individuals, their attributes, and object and data properties [13].

Ontologies are widely used in the field of technical diagnostics. They provide a unified terminology between communicating distributed diagnostic agents [14], replace a standard way to describe configurations of industrial equipment [15], and describe communicating components in the system [16]. Another popular approach is to augment diagnostic models with ontologies to verify sensor data [16-18].

There are approaches, in which an ontology serves as a core of a diagnostic model. However, they are designed for other knowledge domains: mainly the automotive domain [19-21], but also for steam turbines [22] and ventilation systems [23] – and are not applicable for data storage system diagnosis. For example, Saeed et al. [24] describe a general ontological approach to the active diagnosis of sensors and actuators in embedded systems.

Schoenfisch et al. [25] proposed to perform RCA for IT infrastructures by reasoning over a Markov logic network, obtained from an ontology that models a system being diagnosed. The ontology defines types of components and possible relations between them, including a dependency graph. However, the ontology includes the information only regarding the potential risks for the components, therefore, it cannot be used for fault detection purposes. Moreover, the approach is centered around a user, who constructs a model and performs RCA, which limits its applicability for autonomous embedded diagnosis.

Similarly, to work by Dendani et al. [26], the presented approach resembles a knowledge-based system within a case-based reasoning methodology [27], namely, its case representation and case matching and retrieval aspects. A new ontology at the core of the presented approach aims to support all steps of

diagnosis for a data storage system: monitoring, fault detection, RCA, and deciding on management actions.

2.3 Software Logs as a Source of Diagnostic Data

A typical enterprise data storage system contains multiple server-based nodes, such as storage controllers, fabric controllers, and other components with a sophisticated software ecosystem on top of these hardware components. The software includes operation systems, security and authentication services, data managing services, clustering services, hardware monitoring, and management services. Most of them provide some kind of logging features and, as a result, a typical data storage system generates large volumes of different software logs.

According to their source type, software logs can be classified [28, 29] into event logs, application logs, service logs, and system logs (or into operation system logs, service logs, and application logs as in [30]). System and event logs, such as "dmesg", "faillog" and "messages", are the most obvious sources of diagnostic data, but other types of logs contain useful information as well.

Although the aforementioned logs can be exceptionally important as a source of knowledge about the system's health, there are some difficulties that make them hard to use in enterprise products. Perhaps the main issue, as stated by Zhu [31], is an excessive amount of details in software logs: a typical application log contains a lot of data not related to any particular issue or error. Because of that, during the process of identifying the root cause of a fault, administration staff is forced to manually analyze hundreds of megabytes (or even gigabytes) of event logs, which makes such a procedure extremely time-consuming.

A possible solution to this problem is automated log mining. The most common approach to automated log analysis relies on the interpretation of a log as a structured chain of consecutive events and on log template extraction (see Pande et al. [32], He et al. [33], and Hamooni et al. [34]). These methods usually require some a priori knowledge about the log structure, log message's structure, reasons, and sources of different message types. Hence, some degree of manual analysis of each log type, used as a source of diagnostic data, is still needed.

Another possible approach, presented for example by Bertero et al. [35], handles a software log as raw text data, which can be analyzed using natural language processing methods. As a result, each log type can be used as a source of diagnostic data without prior study. Because of that, although these methods provide less accurate results compared to the methods, based on a log structure analysis, they are more preferable in case of an implementation coupled with an ontological diagnostic model.

3 Ontological Approach to Data Storage System Diagnostics

3.1 Ontology of Data Storage System Health

A set of root disjoint classes and a set of property types as an ontology schema are the basis for the presented diagnostic approach. Each root class has a tree of subclasses that represents related concepts in the data storage reliability domain: for example, subclasses from the *Parameter* tree are the names of known types of monitoring data as diagnostic parameters, subclasses from the *SystemFault* tree are the names of known types of system events. Object properties describe relationships between particular concepts: for example, a relationship *may_lead_to* between two subclasses from the *ComponentFault* indicates that one particular type of fault is known to lead to another type of fault. Figure 1 shows all root classes of the schema and types of object properties that can be used to describe relationships between pairs of subclasses. Data and annotation properties provide specific characteristics of separate concepts to support further implementation of diagnostic procedures.

The target users of the ontology are developers of the diagnostic system, who can be considered experts in the field. They may extend existing core ontology by adding subclasses and object and data properties to describe specific knowledge of data storage systems. Then, in order to represent a hierarchical model for a data storage system being diagnosed, that is declared by a *StorageSystem* individual, they should create individuals of subclasses from *Component* and *StorageSubsystem* trees connected by *consists_of* object properties (see Fig. 1).

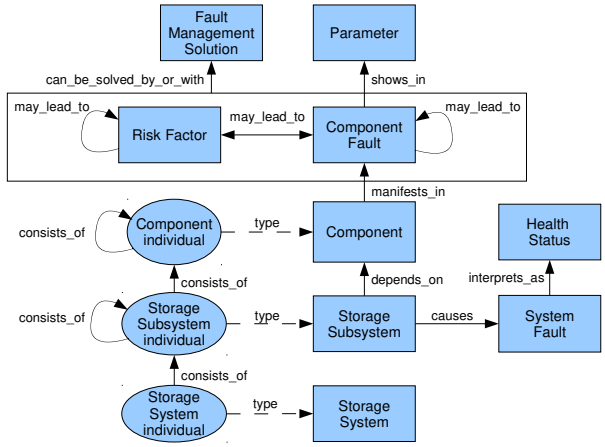

Figure 1

Schema of data storage health ontology

A particular knowledge base derived from this schema should cover the following competencies:

- system configuration competency: what is the current configuration of the data storage system and what are the names of its components and subsystems (*consists_of* object properties);
- symptom competency: which monitoring data may be available and how to identify faults based on the monitoring data (*shows_in_parameter* object properties, also data and annotation properties for subclasses from *Parameter* and *ComponentFault*);
- component operational status competency: how to identify a component's level of performance based on the detected faults (*if_fatal_manifests_in* and *if_warning_manifests_in* object properties);
- subsystem reliability function competency: how a subsystem's operational status depends on its components' statuses (*strongly_depends_on*, *majorly_depends_on,* and *depends_with_ecc_on* object properties);
- root cause competency: what may have caused the fault and which system-level events are caused by the detected faults (*may_lead_to* object properties, also *if_warning_causes* and *if_failed_causes* object properties);
- system health competency: what is the severity level of a system-level event (*interprets_as* object properties);
- management competency (optional): which fault containment procedures can be recommended for the detected faults (*can_be_solved_by_or_with* object properties);
- source information competency (optional): what are the synonyms and translations of specific terms and which sources of information can be referenced (various annotation and data properties).

Besides the support of diagnostics, this ontology can also be used for fault injection during system reliability validation and for a preliminary reliability evaluation at early design stages.

The verification plan for the ontology includes formal coherency and consistency check, checks on compliance with common ontology design rules (with OntOlogy Pitfall Scanner![1]), unit tests, and crowd-sourcing validation. Custom unit tests capture the following requirement: for every individual associated with the current system configuration, the ontology has to have a full path of related object properties to cover all the ontology competencies. Otherwise, a diagnostic model of the system is not complete. On the other hand, if ontology contains a full path for some concept, like a component type or a diagnostic parameter, but the fault

[1] Can be found at http://oops.linkeddata.es/

and health management architecture does not include a corresponding entity, a review of that architecture may be initiated.

The ontology is implemented in Protégé software [36], which is the most often used ontology-editing tool for scientific and academic projects. Currently, the core knowledge base in the form of ontology contains around 2300 axioms and over 500 classes to describe reliability aspects of a data storage system with domain-specific standards, articles, application notes, and in-house expert knowledge as sources of information. The collection of classes includes various components (storage, network, and processing devices, software services), subsystems (storage pool and volume, cluster, network, and other elements of control and data paths), faults (faults by component type, risk factors as environmental factors, human errors or non-monitorable component faults and system faults by subsystem type), extensive set of monitoring parameters (including SMART and SCSI log parameters for disks and typical network interface parameters) and fault management solutions (primarily for network-related faults) [2].

3.2 Knowledge Base Implementation

The recommended approach to implement a particular diagnostic system is to convert a knowledge base from a human-friendly RDF/XML format of an ontology to the N-Quads format of a graph database, which is more appropriate for further machine interpretation. The alternative currently used approaches employ Java frameworks and have limited applicability in the case of embedded implementation. A graph database of choice would be Dgraph (v1.1): compared with alternatives it has an outstanding performance level, is open-source with Apache Public License 2.0, uses Go as a native language and implements GraphQL+– query language[3].

Figure 2 shows the overview of the presented approach. Experts use Protégé as an ontology editor to update the data storage health ontology. Further knowledge manipulations are supposed to be executed by services embedded in a storage controller of a data storage system: custom reporting service provides a system configuration and current monitoring data; a knowledge base builder service converts an ontology to a graph database and supplements it with a system configuration data; and diagnostic service performs the necessary queries to a graph database in order to execute a diagnostic algorithm. Obtained fault detection results and additional interpretation information should be forwarded by a storage processor to an administrator of the system.

[2] Can be found at https://github.com/Mamoutova/data-storage-diagnostic.

[3] Documentation on GraphQL+– can be found at https://docs.dgraph.io/query-language.

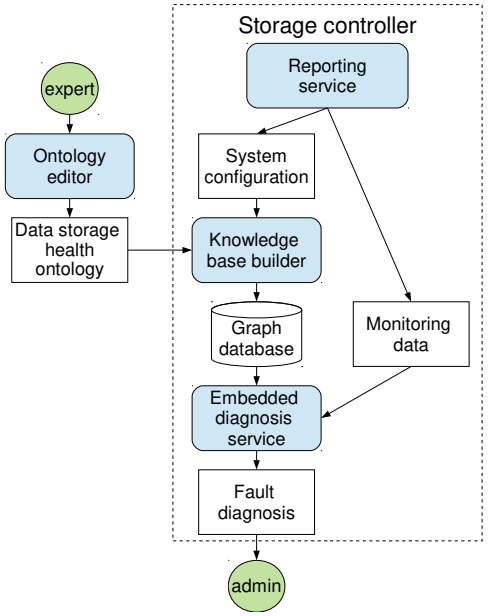

Figure 2
Key elements of the ontological approach to data storage fault diagnosis

To transform an ontology into a graph database, classes and individuals should be converted to graph nodes, while data and object properties – to graph edges. The hierarchical nature of properties can be translated to facets, which allow annotating edges of a graph with arbitrary information.

However, for object properties, the proposed conversion cannot be made directly. According to the Web Ontology Language (OWL) specification, object properties must connect pairs of individuals. On the contrary, the ontology of data storage system health heavily utilizes object properties to connect pairs of subclasses. The latter is properly supported by Protégé as an ontology editor though, with auxiliary *owl:Restriction* classes. Table 1 shows an example description of *if_fatal_manifests_in* object property connecting *Component* and *BadHealth* in the RDF/XML format and a desired corresponding description in the N-Quads format.

Table 1
Example definition of an object property in the RDF/XML and N-Quads formats

Format	Description example

RDF/XML	`<owl:Class rdf:about="urn:#`**`Component`**`">`
	`<rdfs:subClassOf>`
	`<owl:Restriction>`
	`<owl:onProperty`
	`rdf:resource="urn:#`**`if_fatal_manifests_in`**`"/>`

	<owl:someValuesFrom rdf:resource="urn:#**BadHealth**"/> </owl:Restriction> </rdfs:subClassOf> </owl:Class>
N-Quads	<urn:#**Component**><urn:#**if_fatal_manifests_in**><urn:#**BadHealth**>**.**

This simplified schema of a graph database allows streamlining the further implementation of a diagnostic algorithm. Table 2 shows an example of a query to the ontology and a corresponding query to the graph database: both queries search for the name of a system event resulting from the transition of a storage pool to the health level "warning".

Table 2

Queries to knowledge base in the form of ontology (SPARQL language) and in the form of graph database (GraphQL+–)

Query language	Query example
SPARQL (ontology)	SELECT ?event WHERE{ ?entity rdfs:label "StoragePool_id" . ?entity rdfs:subClassOf ?aux . ?aux owl:onProperty ?property . ?property rdfs:label "if_warning_causes" . ?aux owl:someValuesFrom ? event. }

GraphQL+– (graph database)	status (func: uid(StoragePool_uid)) {
	causes
	@facets(eq(rank, if_warning_causes)) {
	name }

Besides simplified queries, this transition from the ontology format to the graph database format allows accelerated machine processing of queries to the knowledge base due to better inherent data indexing. As a result, higher performance of the diagnostic algorithm enables its easier real-time implementation in presence of large amounts of monitoring data.

3.3 Diagnostic Algorithm

The proposed diagnostic algorithm has a modular structure: it uses component operational status and symptom competencies of the ontology to evaluate a component state based on current monitoring data; then it uses system configuration, subsystem reliability function, and root cause competencies to find relevant subsystems and evaluate their states; finally, it uses system health competency to report overall health of a data storage system. Thus, a particular diagnostic procedure can be reconfigured by choosing an appropriate trigger and

order of the function execution: by monitoring changes in diagnostic parameters with a bottom-up approach, or by a massive periodic status check of all subsystems and components with a top-down approach.

The necessary preparation step for the diagnostic algorithm includes the actualization of a system configuration followed by ontology verification. Further execution of the algorithm can be performed by a storage processor in a real-time manner.

For a bottom-up approach, a change in monitoring data of a component triggers algorithm execution. The fault diagnosis algorithm looks like the following, in which every step can be implemented with a corresponding GraphQL+– query:

1) Identify the type of the component and all parent component types.
2) Search for component faults associated with the tree of component types.
3) Search for the fault symptoms.
4) Check whether the current monitoring data confirm any of the symptoms.
5) Evaluate the component health state.
6) Recursively search through the system configuration for the subsystems that include the component and other subsystems that include the found subsystems. For every found subsystem reconstruct its reliability function and evaluate its health state.
8) Identify the names of the system events corresponding to the tuple of subsystem health levels.
9) Interpret the tuple of system events in terms of the overall data storage system health.
10) Search for the associated faults and risk factors for the tuple of detected component faults and system events and search for the corresponding recommended fault containment procedures.

For example, suppose that one of the disks in a system reports an increasing number of corrected errors while having over a year of accumulated power-on hours, which also shows in background scan results. According to the expert knowledge, this indicates an expected degradation of the disk media, which can be interpreted as a warning state of the disk (see Fig. 3). Suppose that the disk is in a storage pool with a 10+2 error correction scheme. When two disks get a warning state, the state of the pool becomes vulnerable. Hence, the states of other storage pools that include this pool and the state of the whole data path become vulnerable as well.

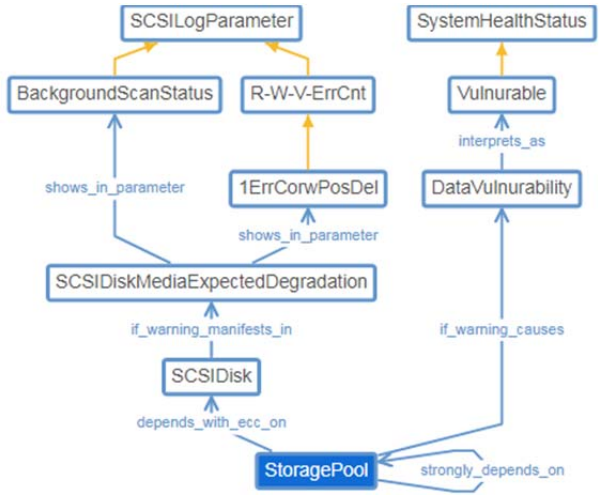

Figure 3

Segment of the ontology of data storage system health regarding health of a storage pool

3.4 Three Types of Symptom Definition

The key to successful fault detection is a thorough description of fault symptoms together with continuous monitoring of corresponding diagnostic parameters. To cover the widest spectrum of symptoms the ontological approach provides several methods to define a symptom: the simple threshold-based method, the complex expression-based method, and the method with external procedures.

The simple threshold-based method can be used, when a monitoring parameter has a fixed range of normal values and unambiguously gives evidence of a fault. A typical example would be a fan failure, which manifests in a zero fan speed. This simple method of symptom definition utilizes data properties of ontology: core ontology schema includes data properties *is_normal_above*, *is_normal_below,* and *is_normal_when* to be used with subclasses from *Parameter*. If a symptom of a fault includes several parameters, values of all parameters have to be abnormal to evidence a fault.

This threshold-based method has several obvious limitations. A data property can define normal values of a parameter only with a simple threshold or as a single value, but cannot be used in a straightforward manner if a range of normal values is a bounded interval or a tuple of values. Moreover, if one parameter has different ranges of normal values for different symptoms, has different significance for different symptoms or a fault manifests in different combinations of parameters' values, this method also fails.

The complex expression-based method of symptom definition overcomes all these limitations. An annotation property *has_symptom_description* for a subclass from *ComponentFault* can store an arbitrary expression to be interpreted in addition to *shows_in_parameter* object properties. In general, such an expression can take any form as long as it unambiguously describes a symptom. *shows_in_parameter* object properties although redundant for the fault identification task can still be used to identify, which parameters should be included in a set of monitored data.

For example, a disk is a component type, whose faults require this expression-based method of symptom definition. Disks perform complex self-diagnosing and report results that demand further analysis. Some of the complex symptoms (based on a report on failure trends by Pinheiro et al. [37]) are shown in Table 3.

When a symptom function is too complex to be expressed in an annotation property, a knowledge base can provide a link to an external procedure. This method with external procedures can also be used, when a fault manifests in some anomaly in the monitoring data and cannot be associated with immediate values of diagnostic parameters, which requires the application of machine learning techniques. In this case, a black-box diagnostic model would be able to detect changes in a component or subsystem performance, while corresponding segments of the ontology would be able to provide further insight into the problem.

Table 3

Examples of symptom descriptions in the ontology of data storage system health

Fault	Symptom description

Damage due to temperature changes	`<owl:Class rdf:about="urn:`**`AbnormalTemperatureDriveDamage`**`">`
	`  <has_symptom_description>` **`Grade`** `= consumer AND (`
	`    `**`Temperature`** `< 30 OR` **`Temperature`** `> 40 AND` **`PowerOnHours`** `>= 3 y )`
	`  </has_symptom_description>`
	`</owl:Class>`

Damaged disc surface	`<owl:Class rdf:about="urn:`**`DriveSurfaceDefects`**`">`
	`  <has_symptom_description>` **`Grade`** `= consumer AND (`
	`    `**`ScanErrorCount`** `> 0 AND` **`PowerOnHours`** `>= 1 y )`
	`  </has_symptom_description>`
	`</owl:Class>`

	`<owl:Class rdf:about="urn:`**`CriticalDriveSurfaceDefects`**`">`
	`  <has_symptom_description>` **`Grade`** `= consumer AND`
	`    ( `**`ScanErrorCount`** `> 0 AND` **`PowerOnHours`** `< 1 m )`
	`  </has_symptom_description>`
	`</owl:Class>`

For these purposes additional *solves_with* and *described_by* pair of object properties is introduced as a method of formal description of implicit relations between diagnostic data and system health (see Fig. 4).

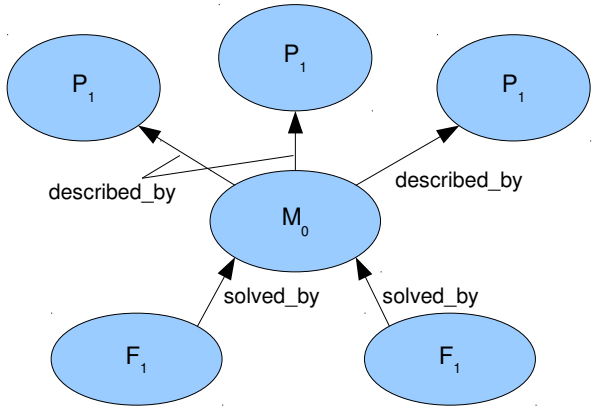

Figure 4
Example of symptoms description with links to external procedure

Properties *described_by* define a set of parameters *{P}* that should be passed to an external procedure M_0. An external procedure should classify the set of the parameter values as one of the probable component fault symptoms *{F}*, defined by *solves_with* property. In the simplest case, such a procedure contains a sequence of "if…else" rules. However, its main purpose is to provide an interface to the trained in advance machine learning models, such as anomaly detection or text classification methods. The assessment of fault event occurrence, made by the external procedure, is considered precise and unambiguous, although machine learning methods usually provide probabilities of various outcomes. In that case, component health is determined by the most probable fault event.

4 Software Logs

The presented paper proposes an approach to software log analysis, which can be used as an external procedure in the process of symptom definition. The proposed approach is based on text preprocessing and classification methods, widely used in the field of natural language processing. A pair of *solves_with* and *described_by* properties takes a set of software logs as diagnostic parameters *{P}*. The parameter values are determined using preprocessing of consecutive message blocks in a given time interval (one minute time interval prior to the current timestamp is recommended). The resulting set *{F, F'}* contains all probable fault events,

corresponding to the parameters from *{P} (F)* and an abstract event *(F')*, for a component state without any faults.

In such a manner a software log can be used as a diagnostic parameter only if it meets certain requirements: it should be stored in plain text and all log messages should have timestamps.

4.1 Log Data Preparation

The proposed fault detection algorithm contains three major steps:

1) Text preprocessing.
2) Calculation of the parameter values.
3) Classification procedure.

The text preprocessing procedure consists of the message text part extraction and text cleaning. Text cleaning is a procedure, commonly used in natural language processing. It includes text tokenization, non-numerical tokens removal, converting tokens to lowercase, removal of the stop-words, stemming, and filtration.

In the second step, the algorithm takes a resulting token array and calculates a final feature vector for each log, combining word embedding and the set of text-level features, presented in Table 4. Word embedding is a one-hot encoding with tf-idf [38] weight coefficients calculation. The text-level features characterize the statistical properties of the whole message block.

Table 4
Text-level log parameters

Parameter	Type
Number of tokens in a given time interval	Int
Number of messages in a given time interval	Int
Average log message length in a given time interval	Float
Average tokens per second in a given time interval	Int
Average messages per second in a given time interval	Int

Finally, the classification procedure uses a classifier pretrained to determine the most probable text class that corresponds to one of the probable fault events. Training and validation data sets should be prepared from log packages, collected during previous fault event occurrences.

4.2 Ontology Extension

The only step of the diagnostic procedure that requires some explicit log structure analysis is the process of splitting a log into a header and raw text parts in order to extract additional information such as timestamps, process identifiers, etc. Log message splitting is based on combinatorial parsing: each log header field has a simple parser, and those individual parsers should be applied in a defined consecutive order. The ontological model has been supplemented with a set of corresponding classes and properties to store the necessary information.

The Message header class *MessageHeaderFormat* contains the *MessageHeaderFormatField* subclass for information about header fields and their extraction priority and the *MessageHeaderFieldDataType* subclass with information about low-level field data types. Each low-level data type is linked to a dedicated individual parser that should be used to extract a header field value. See Fig. 5 with the example for the message.log file.

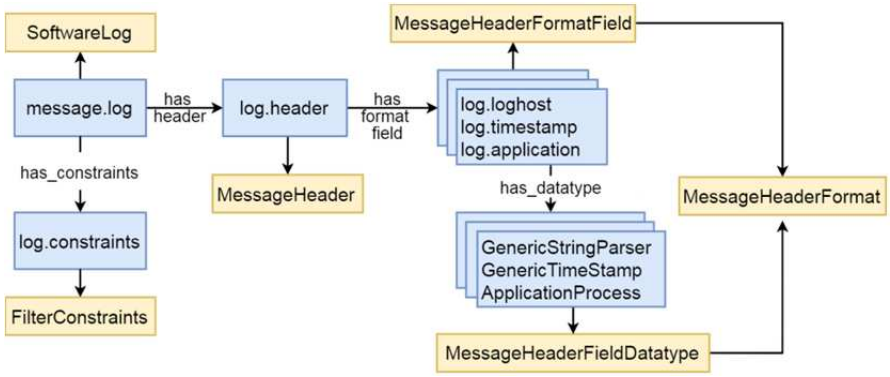

Figure 5

Segment of the ontology of data storage system health regarding message.log header extraction

4.3 Classification Results

The developed approach was evaluated on a dataset of ~ 6000 log packages, each containing up to 116 logs of 33 distinct types. This dataset contains logs, stored after the root cause of a fault investigation, mixed with logs for the healthy system. The dataset consists of 1600 “faulty” log packages with 41 different fault events caused by various problems in a data storage system configuration with two storage processors in a cluster and 16 disk enclosures.

The classification results, presented in Table 5, allow the conclusion that the most suitable classifier algorithm for the dataset is the Random Forest classifier.

Table 5
Classification results

Classifier	Average precision	Average recall	Average f-score	Model training time
Random Forest	0,74	0,71	0,71	183 s
Naïve Bayes	0,48	0,27	0,28	205 s
KNN	0,38	0,39	0,37	166 s
Logistic regression	0,28	0,33	0,28	498 s
SVM	0,23	0,26	0,20	430 s
LSTM	0,47	0,44	0,45	~4 h
GRU	0,24	0,22	0,23	~7 h
LSTM with attention	0,42	0,39	0,40	~ 6 h

Compared with the results acquired by Bertero [35], the presented approach is less accurate, but has the advantage of being able to process logs in almost all formats, analyze text instead of separate messages, and can be a part of an active diagnostic procedure.

Conclusions

The presented ontological approach to embedded diagnostics has been developed with the goal to support autonomous monitoring, diagnosis and self-management within a storage processor with the intent to complement the current data storage system diagnostic portfolio. This approach provides machine representation of the knowledge base in the domain of data storage reliability and diagnostics. The core ontology of the knowledge base provides a schema to store unstructured expert knowledge regarding typical redundancy schemes, symptoms of faults, possible causes of faults, their severity levels, and fault containment procedures. The resulting diagnostic model enables highly heterogeneous monitoring data as diagnostic parameters: for a data storage system they range in types of information, and their sources range in levels of the data storage system hierarchy.

A knowledge base converted from the ontology format to the graph database format is designed to be stored on a storage processor and updated by an administrator when necessary. An embedded implementation of diagnostic model provides necessary visibility of the internal organization of a data storage system. The graph database format provides an increased speed of queries processing. As a result, such direct access of the storage processor to the diagnostic model enables autonomous self-diagnostics at the rate of monitoring data updates. Another significant advantage of the proposed ontological approach is its flexibility, which allows constructing diagnostic models for arbitrary data storage systems.

The limitation of the presented approach is due to no inheritance from existing ontologies, which means that an editing expert has to make a preliminary acquaintance with the new schema of classes and relations.

Another limitation is that the utilization of ontology formalism does not fully comply with the standard OWL 2 specification. In particular, object properties are heavily used to specify relationships between classes, and domain and range properties are used to specify the range of definition for object properties. However, such non-standard use of ontologies is fully supported by the Protégé as an ontology editing tool and serves the objectives of the diagnostics. In this manner, an expert gets a convenient interface for knowledge base editing and after the ontology is converted to a graph database the ontological framework is not used for further processing.

Software logs have proven to be a valuable source of diagnostic data. The proposed approach to automated log mining performs on par with the most popular log analysis techniques without almost any specific research, which makes it an appropriate choice for an external procedure as a part of ontological fault symptom definition.

Thus, the new ontological approach to diagnose data storage systems is based on the formal model-based representation of expert knowledge about data storage system health and employs machine learning algorithms to define relations between health states and parameter values. Compared with the methods that implement only deterministic rules the new approach allows to automatically detect a wider range of fault types, whilst similarly to existing model-based approaches it allows to perform fault localization. The developed prototype of a diagnostic service allows for detection of more than 40 different fault types using log files as a source of diagnostic data, with an average precision of 0.74 and model training time of fewer than 4 minutes. The deterministic part of the implemented ontology-based diagnostic model contains around 2300 axioms, including 25 data and object property types and over 500 classes, with more than 100 referring to the faults in a data storage system.

Acknowledgement

This work was supported by the Ministry of Science and Higher Education of Russian Federation within the framework of the Federal Program “Research and Development in Priority Areas for the Development of the Russian Science and Technology Complex for 2014-2020” (RFMEFI58117X0023).

References

[1] U. Troppens, W. Muller-Friedt, R. Wolafka, R. Erkens, N. Haustein: Business continuity, Storage Networks Explained, 2nd ed., Chichester, United Kingdom, 2009

[2] Common architecture. Storage Management Initiative Specification (SMI-S) v1.8.0 rev. 3, Storage Network Industry Association, 2018

[3] J. Tate, P. Beck, H. H. Ibarra, S. Kumaravel, L. Miklas: Introduction to Storage Area Networks, IBM Redbooks, 2018

[4] O. Mamoutova, M. Uspenskiy, A. Sochnev, S. Smirnov, M. Bolsunovskaya: Knowledge based diagnostic approach for enterprise storage systems, Proceedings of IEEE 17th International Symposium on Intelligent Systems and Informatics, Subotica, Serbia, 2019

[5] V. Filks, G. Ruth: Magic quadrant for storage resource management and SAN management software, G00232275, Gartner, 2012

[6] G. Pruett et al.: BladeCenter systems management software, IBM Journal of Research and Development, Vol. 49, No. 6, 2005, pp. 963-975

[7] S. Gopisetty et al.: Evolution of storage management: transforming raw data into information, IBM Journal of Research and Development, Vol. 52, No. 4.5, 2008, pp. 341-352

[8] C. Ciccotelli et al.: NIRVANA: a non-intrusive black-box monitoring framework for rack-level fault detection, Proceedings of 21st Pacific Rim International Symposium on Dependable Computing, Zhangjiajie, China, 2015, pp. 11-20

[9] R. Kedia, A. Lunawat: Artificial intelligence based storage management architecture, Proceedings of 2018 IEEE International Conference on Cloud Computing in Emerging Markets, Bangalore, India, 2018, pp. 110-114

[10] 2019 top network performance challenges, Industry Survey Findings, Sirkin Research, 2018

[11] D. Breitgand, E. Henis, E. Ladan-Mozes, O. Shehory, E. Yerushalmi: Root-cause analysis of SAN performance problems: an I/O path affine search approach, Proceedings of 9th IFIP/IEEE International Symposium on Integrated Network Management, Nice, France, 2005, pp. 251-264

[12] R. Kannan, S. Ramanathan, S. Subramanian, B. Vaidhinathan: Root-cause approach to problem diagnosis in data networks, U.S. Patent 2009028053 (A1), Jan. 29, 2009

[13] N. F. Noy, D. Mcguinness: Ontology development 101: a guide to creating your first ontology, Stanford Knowledge Systems Laboratory, 2001

[14] M. Albert, T. Langle, H. Worn, M. Capobianco, A. Brighenti: Multi-agent systems for industrial diagnostics, IFAC Proceedings Volumes, Vol. 36, No. 5, 2003, pp. 459-464

[15] R. Muller: Ontologies in automation, M.S. thesis, TU Wien, Vienna, 2008

[16] M. Merdan, M. Vallee, W. Lepuschitz, A. Zoitl: Monitoring and diagnostics of industrial systems using automation agents, International Journal of Production Research, Vol. 49, No. 5, 2011, pp. 1497-1509

[17] L. B. Amor, I. Lahyani, M. Jmaiel: Towards ODRAH: an ontology-based data reliability assessment in mobile health, Proceedings of IEEE/ACS 13th

International Conference of Computer Systems and Applications, Agadir, Morocco, 2016, pp. 1-8

[18] M. Sir, Z. Bradac, V. Kaczmarczyk: Ontology and automation technique, Proceedings of 5th WSEAS international conference on Communications and information technology, Corfu Island, Greece, 2011, pp. 171-174

[19] F. Xu, X. Liu, W. Chen, C. Zhou, B. Cao: Ontology-based method for fault diagnosis of loaders, Sensors, Vol. 18, No. 3, 2018, p. 729

[20] D. G. Rajpathak: An ontology based text mining system for knowledge discovery from the diagnosis data in the automotive domain, Computers in Industry, Vol. 64, No. 5, 2013, pp. 565-580

[21] J. Yi, B. Ji, C. Chen, X. Tian: Employing ontology to build the engine fault diagnosis expert system, Proceedings of WRI World Congress on Computer Science and Information Engineering, Vol. 2, Los Angeles, USA, 2009, pp. 631-635

[22] M. T. Khadir, S. Klai: A steam turbine diagnostic maintenance system based on an evolutive domain ontology, Proceedings of International Conference on Machine and Web Intelligence, Algiers, Algeria, 2010, pp. 360-367

[23] A. Mallak, A. Behravan, C. Weber, M. Fathi, R. Obermaisser: A graph-based sensor fault detection and diagnosis for demand-controlled ventilation systems extracted from a semantic ontology, Proceedings of IEEE 22nd International Conference on Intelligent Engineering Systems, Las Palmas de Gran Canaria, Spain, 2018, pp. 000377-000382

[24] N. T. M. Saeed et al.: ADISTES ontology for active diagnosis of sensors and actuators in distributed embedded systems, Proceedings of IEEE International Conference on Electro Information Technology, Brookings, USA, 2019, pp. 572-577

[25] J. Schoenfisch, C. Meilicke, J. von Stulpnagel, J. Ortmann, H. Stuckenschmidt: Root cause analysis in IT infrastructures using ontologies and abduction in Markov Logic Networks, Information Systems, Vol. 74, May 2018, pp. 103-116

[26] N. Dendani, Med. Khadir, S. Guessoum: Hybrid approach for fault diagnosis based on CBR and ontology: Using jCOLIBRI framework, Proceedings of IEEE International Conference on Complex Systems, Agadir, Morocco, 2012, pp. 1-8

[27] S. H. El-Sappagh, M. Elmogy: Case based reasoning: case representation methodologies, International Journal of Advanced Computer Science and Applications, Vol. 6, No. 11, 2015

[28] What are linux logs? Code examples, tutorials & more, 2017, https://stackify.com/linux-logs/

[29] Marcel: 12 critical linux log files you must be monitoring, 2018, https://www.eurovps.com/blog/important-linux-log-files-you-must-be-monitoring/

[30] Linux logging basics – the ultimate guide to logging, https://www.loggly.com/ultimate-guide/linux-logging-basics/

[31] J. Zhu et al.: Tools and benchmarks for automated log parsing, Proceedings of IEEE/ACM 41st International Conference on Software Engineering: Software Engineering in Practice, Montreal, Canada, 2019, pp. 121-130

[32] A. Pande, V. Ahuja: WEAC: word embeddings for anomaly classification from event logs, Proceedings of IEEE International Conference on Big Data, Boston, USA, 2017, pp. 1095-1100

[33] P. He, J. Zhu, S. He, J. Li, M. R. Lyu: An evaluation study on log parsing and its use in log mining, Proceedings of 46th Annual International Conference on Dependable Systems and Networks, 2016, pp. 654-661

[34] H. Hamooni et al.: LogMine: fast pattern recognition for log analytics, Proceedings of 25th ACM International Conference on Information and Knowledge Management, New York, USA, 2016, pp. 1573-1582

[35] C. Bertero: Experience report: log mining using natural language processing and application to anomaly detection, Proceedings of IEEE 28th International Symposium on Software Reliability Engineering, Toulouse, 2017, pp. 351-360

[36] M. A. Musen: The Protege project: a look back and a look forward, AI Matters, Vol. 1, No. 4, 2015, pp. 4-12

[37] E. Pinheiro, W.-D. Weber, L. A. Barroso: Failure trends in a large disk drive population, Proceedings of 5th USENIX Conference on File and Storage Technologies, Berkeley, USA, 2007, p. 2

[38] G. Salton, C. Buckley: Term-weighting approaches in automatic text retrieval, Information Processing & Management, No. 24, 1988, pp. 513-523

Comparison of Derivative-free Method and Finite-difference Method for Singular Systems

Sandra Buhmiler[1], Sanja Rapajić[2], Slavica Medić[1], Nataša Duraković[1], Tatjana Grbić[1]

[1]University of Novi Sad, Faculty of Technical Sciences, Trg Dositeja Obradovića 6, 21000 Novi Sad, Serbia

[2] University of Novi Sad, Faculty of Sciences, Trg Dositeja Obradovića 3, 21000 Novi Sad, Serbia

e-mails: sandrabu@uns.ac.rs, sanja@dmi.uns.ac.rs, slavicam@uns.ac.rs, natasa.durakovic@uns.ac.rs, tatjana@uns.ac.rs

Abstract: In this paper, the derivative-free method for solving singular systems is compared with the classical finite-difference method for nonlinear systems. Since the convergence rate of an iterative method to singular solution drops down, the convergence can be accelerated by forming the bordered system. Left and right singular vectors of the finite-difference approximation of the Jacobian are used for the construction of the bordered system. The local algorithm for finding a solution is tested on several examples and compared with the finite-difference method. The obtained numerical results, which are promising, indicate fast local convergence of the proposed derivative-free method and point out that it has better performances than the finite-difference method.

Keywords: nonlinear system; singular system; bordered system; finite-difference approximation

1 Introduction

Consider the nonlinear system

$$F(x) = 0, \tag{1}$$

where $F: \mathbb{R}^n \to \mathbb{R}^n$, $F(x) = (F_1(x), F_2(x), \dots, F_n(x))^T$ and let x^* be the solution of (1). Nonsingularity of the Jacobian matrix $F'(x^*)$, namely nonsingularity of the problem, allows one to use Newton's method for finding the solution of the system (1). Newton's method is one of the most popular iterative methods because of its local quadratic convergence. However, Newton's method is very expensive since in every iteration the Jacobian matrix should be calculated. That is why

quasi-Newton (QN) methods have been developed. In every iteration, QN methods use the Jacobian approximation, which is obtained by updating the previous one, using basic matrix operations.

When the Jacobian matrix $F'(x^*)$ is singular, the problem is singular and the convergence rate of an iterative method decreases. One of the most important results about the convergence of Newton's method in the singular case, [1], shows that the region of the acceptable initial points has changed, compared to the regular case. Convergence rate of the component that corresponds to the null space of the Jacobian $F'(x^*)$ is slower and it affects the convergence of the entire iterative sequence. These results were extended to singular problems having higher-order singularities, [2], [3]. A more detailed convergence analysis of Newton's method can be found in [4], while similar results for the convergence of QN methods are given in [5], [6], [7].

To accelerate convergence to the singular solution, one can modify the method or modify the problem. The acceleration of Newton's method in several ways can be found in [8]. Modifications of the method such as including mid-iteration or including second derivative, Hessian, can speed up the convergence. The modifications with mid-iteration are given for Newton's method, [9], inexact Newton's method, [7], and Shamanski's method, [10]. Based on these modifications, in [11], two modifications of the arbitrary QN method are suggested and tested for Thomas', [12], Broyden's, [13], and Martinez's, [14], methods. The other methods which use the second derivative are proposed in [15], [16], [17].

Constructing the bordered system, the initial singular system is transformed into the regular one by inserting additional variables. For problems having isolated solutions and Jacobian rank deficiency $q = 1$, the construction of the bordered system is proposed in [18], although the method given in [8] can be used to accelerate the convergence to the solution that is not singular. Under certain conditions, imposing additional variables to the singular problem leads to rapid convergence to the solution. The construction of the bordered system for the problems with Jacobian $F'(x^*)$ having rank deficiency $q \geq 1$ can be found in [8], [19], and [20].

In [21], the bordered system was formed using left and right singular vectors of the Jacobian $F'(\bar{x})$, where $\bar{x}$ is close enough to the solution x^*. The fast local algorithm was proposed and its convergence to the solution of the initial problem was theoretically proven and applied on several numerical examples. Since in many applications, function $F(x)$ is not available analytically and direct evaluation of the Jacobian and Hessian is not possible, the bordered system and fast local and global algorithm for finding its solution were presented in [22], using finite-difference approximations. Both algorithms have very good characteristics, like fast local convergence around the solution.

In order to construct the derivative-free method to define a bordered system, the algorithm that uses left and right singular vectors of the finite-difference approximation of the Jacobian close to the solution is proposed in [23]. The algorithm was tested on two singular examples and numerical results show that all good properties are preserved. In this paper, we want to compare the features of this algorithm with the classical finite-difference method for nonlinear systems since both algorithms are completely derivative-free and can be applied to problems when the function is not given analytically.

The paper is organized in the following way. Some preliminaries are given in the second section. The third section presents the construction procedure of the bordered system using singular vectors of the Jacobian's finite-difference approximation. The derivative-free algorithm that uses only approximations of the Jacobian and Hessian both in defining and solving the bordered system is also presented. Numerical examples are given in the fourth section, where the local character of the algorithm and its very fast convergence in the neighbourhood of the solution are illustrated and compared with the finite-difference method.

2 Preliminaries

This section contains some basic definitions which are necessary.

Definition 1: [15]

Tensor $T \in \mathbb{R}^{n\times n\times n}$ is composed of n horizontal faces $H_k \in \mathbb{R}^{n\times n}$, $k = 1, \dots, n$, where $[H_k]_{i,j} = [\mathrm{T}]_{i,j,k}$.

Products between tensor $T \in \mathbb{R}^{n\times n\times n}$ and vector $v \in \mathbb{R}^n$ are defined in the following way

$Tv = ((H_1 v)^T, (H_2 v)^T, \dots, (H_n v)^T)^T \in \mathbb{R}^{n\times n}$,

$v^T T = (v^T H_1, v^T H_2, \dots, v^T H_n)^T \in \mathbb{R}^{n\times n}$.

For symmetric matrices $H_1, H_2, \dots, H_n$, the product is commutative, i.e., $Tv = v^T T$.

Let $F''(x) \in \mathbb{R}^{n\times n\times n}$ be the second G-derivative of $F(x)$ composed by n horizontal faces $H_k(x)$, where $H_k(x)$ is Hessian matrix of component $F_k(x)$, $k = 1,2, \dots, n$. Then,

$F''(x)v = ((H_1(x)v)^T, (H_2(x)v)^T, \dots, (H_n(x)\, v)^T)^T \in \mathbb{R}^{n\times n}$.

For $\xi > 0$, the finite-difference approximations of Jacobian $F'(x)$ and Hessian $H_k(x)$, denoted by $D(x, \xi)$ and $H_k(x, \xi)$, are defined by

$$[D(x,\xi)]_{i,j} = \frac{F_i\left(x+\xi e_j\right) - F_i\left(x-\xi e_j\right)}{2\xi}, \tag{2}$$

$$[H_k(x,\xi)]_{i,j} = \frac{F_k\left(x+\xi e_i+\xi e_j\right) - F_k\left(x+\xi e_i-\xi e_j\right) - F_k\left(x-\xi e_i+\xi e_j\right) + F_k\left(x-\xi e_i-\xi e_j\right)}{4\xi^2}, \tag{3}$$

for $i,j = 1,2,\dots,n$ and e_j, e_i being the j −th and i −th unit vector, respectively.

Thus, the finite-difference approximation of $F''(x) \in \mathbb{R}^{n\times n\times n}$, denoted by $F''(x,\xi) \in \mathbb{R}^{n\times n\times n}$, is composed by n horizontal faces $H_k(x,\xi), k = 1,2,\dots,n$, defined by (3).

Throughout the paper, the Euclidean norm denoted by $\|.\|$ will be used. Besides, the infinity norm, denoted by $\|.\|_{\infty,}$ will also be used in the fourth section.

3 Bordered System and Algorithm

We will assume that function F satisfies the following conditions:

A1: F is twice continuously differentiable and $F''(x)$ is Lipschitz continuous in some neighbourhood of the solution, $\mathcal{B}(x^*,\varepsilon)$.

A2: Jacobian $F'(x^*)$ has rank $r = rank\ F'(x^*) = n-q$, for $1 \le q \le n$.

A3: There exists a nonzero vector $\mu^* \in N((F'(x^*))^T)$ and a basis $\{\eta_1^*, \eta_2^*, \dots, \eta_q^*\}$ of the null space $N(F'(x^*))$ such that $q \times q$ matrix

$$[\eta^*]^T[(\mu^*)^T F''(x^*)]\eta^* \equiv [\eta_1^*, \eta_2^*, \dots, \eta_q^*]^T[(\mu^*)^T F''(x^*)][\eta_1^*, \eta_2^*, \dots, \eta_q^*]$$

is nonsingular.

SVD factorization gives

$$D(\bar{x},\xi) = \bar{U}(\bar{x})\bar{\Sigma}(\bar{x})\bar{V}^T(\bar{x})$$

$$= [\bar{u}_1(\bar{x}), \dots, \bar{u}_n(\bar{x})]diag\left(\bar{\sigma}_1(\bar{x}), \bar{\sigma}_2(\bar{x}), \dots, \bar{\sigma}_n(\bar{x})\right)[\bar{v}_1(\bar{x}), \dots, \bar{v}_n(\bar{x})]^T,$$

where $\bar{u}_1(\bar{x}), \dots, \bar{u}_n(\bar{x})$, $\bar{v}_1(\bar{x}), \dots, \bar{v}_n(\bar{x})$ are left and right singular vectors and $\bar{\sigma}_1(\bar{x}), \bar{\sigma}_2(\bar{x}), \dots, \bar{\sigma}_n(\bar{x})$ are corresponding singular values.

Since the singular values are evaluated in descending order

$$\bar{\sigma}_1(\bar{x}) \ge \bar{\sigma}_2(\bar{x}) \ge \cdots \ge \bar{\sigma}_n(\bar{x}) \ge 0$$

and singular values are well conditioned, for $\bar{x} \in \mathcal{B}(x^*,\varepsilon)$ there are q small but nonzero singular values $\bar{\sigma}_{n-q+1}(\bar{x}), \dots, \bar{\sigma}_n(\bar{x})$ of $D(\bar{x},\xi)$.

From singular vectors that correspond to small singular values $\bar{\sigma}_{r+1}(\bar{x}) \ge \cdots \ge \bar{\sigma}_n(\bar{x}) \ge 0$, matrices $\bar{R}(\bar{x}), \bar{L}(\bar{x}) \in \mathbb{R}^{n\times q}$ are formed using

$\bar{R}(\bar{x}) = [\bar{u}_{r+1}(\bar{x}), \dots, \bar{u}_n(\bar{x})]$

and

$\bar{L}(\bar{x}) = [\bar{v}_{r+1}(\bar{x}), \dots, \bar{v}_n(\bar{x})]$.

Matrix $\bar{A}_\xi(x, \bar{x}) \in \mathbb{R}^{(n+q)\times(n+q)}$ is defined using matrices $\bar{R}(\bar{x})$ and $\bar{L}(\bar{x})$

$$\bar{A}_\xi(x, \bar{x}) = \begin{bmatrix} D(x,\xi) & \bar{R}(\bar{x}) \\ \bar{L}^T(\bar{x}) & 0 \end{bmatrix}, \tag{4}$$

where $D(x, \xi)$ is an approximation of $F'(x)$ given by (2).

For $x \in \mathcal{B}(x^*, \varepsilon)$ let $\bar{\eta}(x, \xi) \in \mathbb{R}^{n\times q}$, $\bar{h}(x, \xi) \in \mathbb{R}^{q\times q}$, $\bar{\mu}(x, \xi) \in \mathbb{R}^n$ and $\bar{g}(x, \xi) \in \mathbb{R}^q$ be the solutions of the following systems

$$\bar{A}_\xi(x, \bar{x}) \begin{bmatrix} \bar{\eta}(x,\xi) \\ \bar{h}(x,\xi) \end{bmatrix} = \begin{bmatrix} 0 \\ E_q \end{bmatrix}, \tag{5}$$

$$\bar{A}_\xi{}^T(x, \bar{x}) \begin{bmatrix} \bar{\mu}(x,\xi) \\ \bar{g}(x,\xi) \end{bmatrix} = \begin{bmatrix} 0 \\ \alpha \end{bmatrix}, \tag{6}$$

where $E_q \in \mathbb{R}^{q\times q}$ is an identity matrix and $\alpha \in \mathbb{R}^q$ is a randomly chosen vector.

We expect matrix (4) to be nonsingular and obtained numerical results confirm that. This guarantees the uniqueness of the solutions of systems (5) and (6). Using $\bar{\eta}(x, \xi)$ from (5) and $\bar{\mu}(x, \xi)$ from (6), the $q \times q$ matrix

$\bar{B}_\xi(x, \alpha) \equiv \bar{\eta}^T(x, \xi)\,[\bar{\mu}^T(x, \xi)\, H(x, \xi)]\,\bar{\eta}(x, \xi)$

is formed and it will be used in the algorithm for finding the solution of the bordered system.

The bordered system is defined by

$$\boldsymbol{F}(x, \lambda) = \begin{bmatrix} F(x) + \bar{R}(\bar{x})\lambda \\ \bar{g}(x, \xi) \end{bmatrix} = 0, \tag{7}$$

where $\bar{g}(x, \xi)$ is the solution of the system (6). Vector $\lambda \in \mathbb{R}^q$ corresponds to the relaxation parameter that makes the problem more stable, [8].

The local derivative-free algorithm for solving (7), proposed in [23], is given below.

Algorithm:

Step 0: Choose $x_0 \in \mathbb{R}^n$ and a small parameter $\xi > 0$.

Step 1: Set $\bar{x} = x_0$ and $k = 0$.

Step 2: Compute $D(\bar{x}, \xi)$ using (2), evaluate its SVD, and determine the value of q to form matrices $\bar{R}(\bar{x})$ and $\bar{L}(\bar{x})$.

Step 3: Generate a random vector $\alpha \in \mathbb{R}^q$ and set $\lambda_0 = 0 \in \mathbb{R}^q$.

Repeat Step **4** – **Step 7** until convergence is obtained.

Step 4: Compute $D(x_k, \xi)$ defined by (2) and form $\bar{A}_\xi(x_k, \bar{x})$ defined by (4).

Step 5: Find solutions to the following systems

$$\bar{A}_\xi(x_k, \bar{x})\, Y = \begin{bmatrix} -(F(x_k) + \bar{R}(\bar{x})\lambda_k) \\ 0 \end{bmatrix},$$

$$\bar{A}_\xi(x_k, \bar{x}) \begin{bmatrix} \bar{\eta}\,(x_k, \xi) \\ \bar{h}\,(x_k, \xi) \end{bmatrix} = \begin{bmatrix} 0 \\ E_q \end{bmatrix},$$

$$\bar{A}_\xi{}^T(x_k, \bar{x}) \begin{bmatrix} \bar{\mu}\,(x_k, \xi) \\ \bar{g}\,(x_k, \xi) \end{bmatrix} = \begin{bmatrix} 0 \\ \alpha \end{bmatrix}.$$

Step 6: Compute the matrix

$$\bar{B}_\xi(x_k, \alpha) = \bar{\eta}^T\,(x_k, \xi)\,[\bar{\mu}^T\,(x_k, \xi)\,H(x_k, \xi)]\,\bar{\eta}\,(x_k, \xi)$$

and solve the linear system

$$\bar{B}_\xi(x_k, \alpha)\, W = \bar{g}(x_k, \xi) - \bar{\eta}^T\,(x_k, \xi)\,[\bar{\mu}^T\,(x_k, \xi)\,H(x_k, \xi)]\,Y_1.$$

Step 7: Update step

$$\begin{bmatrix} dx \\ d\lambda \end{bmatrix} = Y + \begin{bmatrix} \bar{\eta}\,(x_k, \xi) \\ \bar{h}\,(x_k, \xi) \end{bmatrix} W,$$

update iteration

$$\begin{bmatrix} x_{k+1} \\ \lambda_{k+1} \end{bmatrix} = \begin{bmatrix} x_k \\ \lambda_k \end{bmatrix} + \begin{bmatrix} dx \\ d\lambda \end{bmatrix}$$

and update k, i.e., $k = k + 1$.

Like in [21] and [22], it is sufficient to determine the solutions $Y = [Y_1 \quad Y_2]^T \in \mathbb{R}^{n+q}$, $\bar{\eta}\,(x, \xi) \in \mathbb{R}^{n \times q}$, $\bar{h}\,(x, \xi) \in \mathbb{R}^{q \times q}$, $\bar{\mu}\,(x, \xi) \in \mathbb{R}^n$ and $\bar{g}\,(x, \xi) \in \mathbb{R}^q$ of the corresponding linear systems in Step 5 and $W \in \mathbb{R}^q$ in Step 6 to update the iteration in Step 7.

In [21] and [22] the bordered system was formed using SVD factorization of $F'(\bar{x})$ for $\bar{x} \in \mathcal{B}(x^*, \varepsilon)$, more precisely using left and right singular vectors of $F'(\bar{x})$. Besides, using the Jacobian matrix $F'(\bar{x})$ in [21] and its finite-difference approximation $D(\bar{x}, \xi)$ in [22], the bordered system was constructed. Nonsingularity of the defined system was proven and fast algorithms for solving it were proposed in [21] and [22].

The local characteristic of the algorithm given in [21] was numerically tested. To achieve fast convergence, the initial iterate has to be very close to the solution, and since the solution is usually not known this was a big disadvantage of the algorithm.

The Jacobian and Hessian matrices were approximated by finite-differences in [22]. Thus, the calculations of derivatives were avoided and application of the algorithm for problems with function, which is not defined analytically is included. The local convergence of the algorithm constructed in that way was proven. To overcome the difficulty of selecting the initial approximation, the local algorithm was combined with a globally convergent descent algorithm with finite-difference approximations. In the beginning, while the current iterate is far away from the solution, the descent algorithm with finite-differences and Armijo rule was used. This prevents large steps. When the step is too small, it was assumed that the current iterate is close to the solution and a local algorithm was applied, taking the current iterate to be the initial approximation.

The algorithms presented in [22] are not completely derivative-free since SVD of the Jacobian $F'(\bar{x})$ and the corresponding singular vectors are used to define bordered system. The previously defined algorithm is constructed using singular vectors of the finite-difference approximation $D(\bar{x}, \xi)$ of Jacobian. This algorithm, proposed in [23], is completely derivative-free and its local characteristic is confirmed on some numerical examples. Furthermore, like in [22], one can exploit the fast local convergence of this algorithm by combining it with a globally convergent method, which will lead to the globally convergent derivative-free method.

In this paper, the local characteristics of the proposed derivative-free algorithm are examined in more detail and compared with the classical finite-difference method.

The rank deficiency q of the Jacobian $F'(x^*)$ is used for defining matrix (4) in Step 4 of the algorithm. The corresponding value of q is unknown and one way to determine this value, [20], is to overestimate it since it is known that in that case, any iterative sequence will not converge. The next step is to decrease the value until the convergence is obtained, but keeping in mind that convergence will occur in case the value of q is underestimated.

The SVD decomposition of $F'(\bar{x})$ implies that there are q small but nonzero singular values, so one can conclude that q is equal to the number of small singular values of finite-difference approximation $D(\bar{x}, \xi)$. Since these values are evaluated in descending order, it is easy to count them and predict the value of q.

4 Numerical Results

We tested the proposed derivative-free algorithm on some relevant examples from [21] and [22], with different starting approximations, and compared it with the classical finite-difference method. The obtained numerical results are presented in this section. We consider that the current iterate x_k generated by both algorithms is a good approximation of the solution if it satisfies $\|F(x_k)\| \leq 10^{-6}$ for the

maximum number of iterations equal to 30. The rate of convergence is determined through the quotient

$$d_k = \frac{\|x^* - x_k\|}{\|x^* - x_{k-1}\|}.$$

The Jacobian and Hessian are approximated by finite-differences with parameter $\xi = 10^{-5}$.

Example 1: Function $F: \mathbb{R}^2 \to \mathbb{R}^2$ is defined by

$$F(x_1, x_2) = \begin{bmatrix} x_1^2 - x_2 \\ x_1^2 + x_2^2 \end{bmatrix}.$$

The singular solution of equation (1) is $x^* = (0,0)^T$. The Jacobian matrix is

$$F'(x_1, x_2) = \begin{bmatrix} 2x_1 & -1 \\ 2x_1 & 2x_2 \end{bmatrix},$$

and since

$$F'(0,0) = \begin{bmatrix} 0 & -1 \\ 0 & 0 \end{bmatrix},$$

the rank deficiency of the Jacobian at the solution is q=1. Moreover, the null space of the Jacobian, $N(F'(0,0))$, is generated by $\eta^* = (1,0)^T$. One characteristic of singular systems is that all components do not converge at the same rate. Slower convergence of the components that correspond to the null space also slows down the convergence of the entire iterative sequence. In this example, the first component is slower than the second one.

In order to examine a local characteristic of the derivative-free algorithm defined in the previous section, iterative sequences generated with three starting points are presented in the following tables. These iterative sequences are compared with the iterative sequences generated by the finite-difference method, using the same starting approximations.

Table 1 presents the iterative sequence generated by the finite-difference method. Since the method is applied to the singular system, slower convergence of the first component is clearly indicated. The convergence rate of the finite-difference method drops from superlinear to linear, which is indicated through the quotient d_k that converges to 0.5.

Table 1

$x_0 = (0.5,0.7)^T$

k	$[x_k]_1$	$[x_k]_2$	$\|F(x_k)\|$	d_k
1	4.541e-01	2.041e-01	2.479e-01	0.578855
2	2.596e-01	2.959e-02	7.808e-02	0.524862
3	1.314e-01	8.274e-04	2.385e-02	0.502899

4	6.572e-02	6.918e-07	6.107e-03	0.500029
5	3.285e-02	7.395e-12	1.526e-03	0.500038
6	1.642e-02	7.396e-17	3.817e-04	0.500076
7	8.219e-03	2.059e-20	9.554e-05	0.500152
8	4.112e-03	-6.512e-21	2.385e-05	0.500304
9	2.058e-03	2.636e-22	5.993e-06	0.500607
10	1.031e-03	2.635e-22	1.505e-06	0.501211
11	5.184e-04	5.187e-23	3.800e-07	0.502411

The iterative sequence generated by our algorithm is presented in Table 2. We can point out that both components of the iterative sequence converge to the solution at the same speed, which affects the convergence of the whole iterative sequence. The quotient d_k converges to 0, which means that superlinear convergence is obtained. The number of iterations needed for the convergence is smaller than in the case when the finite-difference method is applied. All of these indicate that our method is faster than the finite-difference method.

Table 2

α=8.90903, $x_0 = (0.5, 0.7)^T$

k	$[x_k]_1$	$[x_k]_2$	$\|F(x_k)\|$	d_k
1	-9.416e-02	4.026e-01	4.293e-01	0.48075
2	1.218e-02	1.450e-01	1.463e-01	0.351867
3	2.166e-03	3.244e-02	3.245e-02	0.223456
4	1.774e-04	2.473e-03	2.473e-03	0.076274
5	-1.548e-06	1.673e-05	1.673e-05	0.006775
6	8.821e-11	7.774e-10	7.774e-10	0.000046

Similar results are obtained for starting approximations being closer to the solution and generated iterative sequences are presented in Tables 3-6. Iterative sequences generated by the finite-difference method are given in Table 3 and Table 5, while Table 4 and Table 6 contain the sequences generated by our derivative-free algorithm.

Table 3

$x_0 = (0.3, 0.4)^T$

k	$[x_k]_1$	$[x_k]_2$	$\|F(x_k)\|$	d_k
1	2.981e-01	8.889e-02	9.679e-02	0.62224
2	1.603e-01	6.708e-03	3.199e-02	0.515782
3	8.030e-02	4.441e-05	9.088e-03	0.500443
4	4.015e-02	2.423e-09	2.279e-03	0.500031
5	2.008e-02	2.424e-14	5.699e-04	0.500062
6	1.004e-02	2.246e-19	1.426e-04	0.500124
7	5.023e-03	-5.733e-21	3.569e-05	0.500249

8	2.514e-03	1.042e-21	8.941e-06	0.500497
9	1.259e-03	1.958e-22	2.244e-06	0.500992
10	6.323e-04	-1.588e-23	5.654e-07	0.501977

Table 4

α=5.85264, $x_0 = (0.3, 0.4)^T$

k	$[x_k]_1$	$[x_k]_2$	$\|F(x_k)\|$	d_k
1	2.165e-02	5.342e-02	5.305e-02	0.11529
2	5.878e-04	1.651e-03	1.651e-03	0.030412
3	6.050e-07	1.714e-06	1.714e-06	0.001036
4	6.508e-13	1.852e-12	1.852e-12	0.000001

Table 5

$x_0 = (0.02, 0.02)^T$

k	$[x_k]_1$	$[x_k]_2$	$\|F(x_k)\|$	d_k
1	1.962e-02	3.848e-04	3.851e-04	0.693812
2	9.816e-03	1.518e-07	1.361e-04	0.500228
3	4.906e-03	1.541e-12	3.405e-05	0.500255
4	2.457e-03	1.540e-17	8.543e-06	0.500509
5	1.231e-03	3.353e-22	2.144e-06	0.500101
6	6.182e-04	-8.818e-23	5.404e-07	0.502022

Table 6

α=6.99077, $x_0 = (0.02, 0.02)^T$

k	$[x_k]_1$	$[x_k]_2$	$\|F(x_k)\|$	d_k
1	7.179e-04	-3.413e-04	3.418e-04	0.028106
2	-5.090e-07	-4.919e-07	4.919e-07	0.000890

All iterative sequences were generated with starting points close enough to the solution, so the convergence of both methods is obtained. Iterative sequences generated by the finite-difference method need more iterations for the convergence than our method since the system is singular and slower convergence of the first component slows down the convergence of the whole sequence. The convergence rate of sequences presented in Table 1, Table 3, and Table 5 is linear since d_k converges to 0.5.

The sequences generated by our derivative-free algorithm, given in Table 2, Table 4, and Table 6, indicate that both components converge to the solution at the same speed. The rate of the convergence is superlinear since the quotient d_k converges to 0. Faster convergence of our method is a consequence of the fact that the singular system is transformed into the regular one using the bordered system.

To illustrate the local characteristics of the algorithm in detail, we tested it with much more starting points close to the solution and compared the number of

iterations obtained by our derivative-free method with the one required for the convergence when the finite-difference method is applied. The algorithms were tested with starting approximations of the form

$x_0 = (\pm i \cdot 0.1, \pm j \cdot 0.1)^T,$

for $i, j = 0, 1, \ldots, 10$. Since starting points with $i, j = 0, 1, \ldots, 5$ are close enough to the solution, both algorithms have fast convergence for these initial points with $i, j = 0, 1, \ldots, 5$, so only these results are presented in Table 7.

The first column of

Table 7 contains the first component of the initial approximation, $[x_0]_1$, while the first row contains the second component, $[x_0]_2$. Each table field presents the number of iterations for our derivative-free algorithm and the number of iterations for the finite-difference method (given in brackets), generated with the starting point x_0.

Table 7

The number of iterations for derivative-free algorithm and (finite-difference method) with initial point x_0

	-0.5	-0.4	-0.3	-0.2	-0.1	0	0.1	0.2	0.3	0.4	0.5
-0,5	30(28)	9(13)	6(12)	6(11)	6(11)	7(11)	9(11)	16(11)	30(11)	6(11)	6(11)
-0,4	27(28)	8(13)	7(12)	7(11)	6(11)	5(10)	6(10)	6(11)	6(11)	5(11)	5(11)
-0,3	16(28)	7(14)	7(12)	6(11)	6(10)	5(10)	5(10)	5(10)	4(11)	5(11)	5(11)
-0,2	20(29)	7(14)	6(12)	6(11)	5(10)	5(9)	5(10)	4(10)	4(11)	5(11)	5(12)
-0,1	18(30)	6(15)	6(13)	5(11)	5(10)	4(8)	4(9)	4(24)	4(11)	5(11)	5(12)
0	7(4)	5(29)	4(27)	4(25)	3(23)	1(1)	3(22)	4(24)	4(25)	5(26)	5(26)
0,1	18(30)	6(15)	6(13)	5(11)	5(10)	4(8)	4(9)	4(10)	4(11)	5(12)	5(12)
0,2	21(29)	7(14)	6(12)	5(11)	5(10)	5(9)	5(10)	4(10)	4(11)	5(11)	5(12)
0,3	16(28)	7(13)	7(11)	6(11)	6(10)	5(10)	5(10)	5(10)	4(11)	5(11)	5(11)
0,4	30(28)	8(13)	7(12)	6(11)	6(11)	5(10)	6(10)	6(11)	6(11)	5(11)	5(11)
0.5	30(28)	9(13)	6(12)	6(11)	6(11)	7(11)	9(11)	15(11)	30(11)	14(11)	14(11)

Table 7 shows that our derivative-free method is much faster than the finite-difference method for almost all starting points.

Example 2: Function $F: \mathbb{R}^3 \to \mathbb{R}^3$ is defined by

$$F(x_1, x_2, x_3) = \begin{bmatrix} x_1^3 + x_1 x_2 \\ x_2 + x_2^2 \\ x_1^2 + x_3^2 \end{bmatrix}$$

with $x^* = (0,0,0)^T$ being a singular solution of equation (1) and Jacobian matrix

$$F'(x_1, x_2, x_3) = \begin{bmatrix} 3x_1^2 + x_2 & x_1 & 0 \\ 0 & 1 + 2x_2 & 0 \\ 2x_1 & 0 & 2x_3 \end{bmatrix}.$$

Null space of the Jacobian $F'(0,0,0)$ is generated by vectors $\{(1,0,0)^T, (0,0,1)^T\}$. Since

$$F'(0,0,0) = \begin{bmatrix} 0 & 0 & 0 \\ 0 & 1 & 0 \\ 0 & 0 & 0 \end{bmatrix},$$

the rank deficiency is $q = 2$, so we tested our algorithm for $q = 2$ and $q = 1$.

Iterative sequences generated by our method with starting approximation $x_0 = (0.2, 0.5, 0.7)^T$ and two values of q are presented in Table 8 and Table 9.

Table 8

q=2, α=$(9.59492, 6.55741)^T$, $x_0 = (0.2, 0.5, 0.7)^T$

k	$[x_k]_1$	$[x_k]_2$	$[x_k]_3$	$\|F(x_k)\|$	d_k
1	6.066e-03	1.335e-01	2.370e-04	1.513e-01	0.151379
2	3.544e-03	1.409e-02	-1.192e-09	1.429e-02	0.108739
3	4.194e-05	1.987e-04	-1.036e-08	1.988e-04	0.013975
4	9.338e-09	4.045e-08	-1.242e-10	4.045e-08	2.043e-04

The predicted value $q = 2$ is given in Table 8. The first three columns indicate that all components of generated sequence converge to the solution at the same speed and the convergence is fast. The quotient d_k converges to 0 indicating that the convergence rate is superlinear, as it is the rate of convergence of the finite-difference method in regular case.

In Table 9 the predicted value is $q = 1$ and it does not coincide with the real value. The bordered system is formed but it is still singular. Since the first and the third components correspond to null space, the convergence of these components is visibly slower than the convergence of the second component, and this is the characteristic of a singular system. Linear convergence indicated with quotient d_k is the rate of convergence of the finite-difference method in a singular case.

Table 9

q=1, α=0.357117, $x_0 = (0.2, 0.5, 0.7)^T$

k	$[x_k]_1$	$[x_k]_2$	$[x_k]_3$	$\|F(x_k)\|$	d_k
1	-6.366e-02	1.320e-01	4.096e-01	2.279e-01	0.492652
2	-5.903e-03	1.317e-02	2.076e-01	4.515e-02	0.478336
3	-1.196e-04	1.609e-04	1.038e-01	1.078e-02	0.499062
4	-4.087e-05	2.450e-08	5.193e-02	2.697e-03	0.499999
5	-2.241e-05	-5.175e-14	2.596e-02	6.742e-04	0.5
6	-1.274e-05	-4.681e-16	1.298e-02	1.685e-04	0.5
7	-7.322e-06	-1.222e-16	6.491e-03	4.214e-05	0.5
8	-3.877e-06	-5.539e-17	3.245e-03	1.053e-05	0.5
9	-1.241e-06	-3.548e-17	1.622e-03	1.633e-06	0.5
10	1.424e-06	-3.032e-17	8.114e-04	6.584e-07	0.5

Similar results are obtained when our algorithm is applied with starting points $x_0 = (0.1, 0.3, 0.5)^T$ and $x_0 = (0.05, 0.05, 0.05)^T$. Generated sequences with $q = 2$ are shown in Table 10 and Table 12, while Table 11 and Table 13 present sequences with $q = 1$.

Table 10

q=2, α=$(7.43132, 3.92227)^T$, $x_0 = (0.1, 0.3, 0.5)^T$

k	$[x_k]_1$	$[x_k]_2$	$[x_k]_3$	$\|F(x_k)\|$	d_k
1	7.221e-03	5.768e-02	1.747e-05	6.100e-02	0.0982596
2	6.399e-04	3.004e-03	-1.095e-08	3.013e-03	0.0528371
3	1.772e-06	9.095e-06	-1.073e-09	9.095e-06	0.0030170
4	4.958e-11	8.379e-11	-2.982e-12	8.379e-11	1.051e-05

Table 11

q=1, α=6.55478, $x_0 = (0.1, 0.3, 0.5)^T$

k	$[x_k]_1$	$[x_k]_2$	$[x_k]_3$	$\|F(x_k)\|$	d_k
1	-8.594e-02	5.847e-02	2.810e-01	1.064e-01	0.506488
2	-3.820e-02	2.887e-03	1.416e-01	2.170e-02	0.489566
3	-1.912e-02	2.929e-06	7.077e-02	5.374e-03	0.499767
4	-4.790e-03	-2.292e-07	3.538e-02	1.343e-03	0.499977
5	-4.790e-03	-2.843e-08	1.768e-02	3.358e-04	0.499989
6	-2.398e-03	-3.563e-09	8.844e-03	8.396e-05	0.499994
7	-1.201e-03	-4.460e-10	4.421e-03	2.099e-05	0.499997
8	-6.035e-04	-5.579e-11	2.209e-03	5.247e-06	0.499999
9	-3.043e-04	-6.978e-12	1.104e-03	1.311e-06	0.500001
10	-1.547e-04	-8.734e-13	5.514e-05	3.280e-07	0.500005

Table 12

q=2, α=$(1.71187, 7.06046)^T$, $x_0 = (0.05, 0.05, 0.05)^T$

k	$[x_k]_1$	$[x_k]_2$	$[x_k]_3$	$\|F(x_k)\|$	d_k
1	-5.553e-03	2.396e-03	-5.114e-06	2.402e-03	0.0698435
2	-7.163e-05	5.112e-06	9.571e-08	5.112e-06	0.0118738
3	-1.248e-08	1.054e-11	1.250e-09	1.054e-11	0.0001747

Table 13

q=1, α=0.318328, $x_0 = (0.05, 0.05, 0.05)^T$

k	$[x_k]_1$	$[x_k]_2$	$[x_k]_3$	$\|F(x_k)\|$	d_k
1	-3.161e-02	2.306e-03	2.092e-02	2.724e-03	0.438628
2	-1.649e-02	7.491e-06	9.792e-03	3.679e-04	0.504906
3	8.403e-03	9.893e-08	4.665e-03	9.238e-05	0.50113
4	4.232e-03	1.321e-08	2.286e-03	2.314e-05	0.500522
5	2.125e-03	1.705e-09	1.129e-03	5.791e-06	0.500263

6	1.066e-03	2.161e-10	5.586e-04	1.448e-06	0.500136
7	5.354e-04	2.722e-11	2.750e-04	3.623e-07	0.500081

When the rank deficiency is underestimated, the bordered system is still singular and its characteristics can be recognized in Table 11 and Table 13. The quotient d_k converges to 0.5, which guarantees linear convergence and convergence of the first and the third components are slower than the second one.

Faster convergence is obtained when the predicted value is equal to the real value of rank deficiency, i.e., $q = 2$, which can be seen from Table 10 and Table 12. All components converge to the solution at the same speed and the convergence rate of the whole sequence is superlinear.

Table 14 indicates linear convergence of the finite-difference method and presents the obtained results with starting approximations x_0 and the number of iterations, k, needed to achieve a good approximation of the solution. The norm of the function value in the last generated iteration, denoted by $\|F(x_k)\|$, and the quotient d_k are also presented in **Hiba! A hivatkozási forrás nem található.**. Compared to the results presented in Table 8, Table 10 and Table 12, the finite-difference method requires more iterations to achieve convergence than our derivative-free algorithm. That was expected since for $q = 2$ the iterative sequences in Table 8, Table 10 and Table 12 converge to the regular solution of the bordered system. Besides, compared to the results given in Table 9, Table 11 and Table 13, the finite-difference method is also slower than our derivative-free method, although for $q = 1$ both systems are singular.

Table 14

x_0	k	$[x_k]_1$	$[x_k]_2$	$[x_k]_3$	$\|F(x_k)\|$	d_k
$(0.2,0.5,0.7)^T$	15	6.973e-04	2.486e-63	-1.709e-04	5.155e-07	0.632681
$(0.1,0.3,0.5)^T$	15	3.993e-04	1.459e-65	-4.328e-04	3.468e-07	0.509358
$(0.05,0.05,0.05)^T$	11	9.101e-04	7.834e-51	-3.55e-04	9.543e-07	0.533782

Example 3: Function $F: \mathbb{R}^4 \to \mathbb{R}^4$ is defined by

$$F(x_1, x_2, x_3, x_4) = \begin{bmatrix} x_1 + x_1x_2 + x_2^2 \\ x_1^2 - 2x_1 + x_2^2 \\ x_1 + x_3^2 \\ x_1^2 + x_4^2 \end{bmatrix}.$$

The solution of equation (1) is $x^* = (0,0,0,0)^T$ and the Jacobian matrix is

$$F'(x_1, x_2, x_3, x_4) = \begin{bmatrix} 1 + x_2 & x_1 + 2x_2 & 0 & 0 \\ 2x_1 - 2 & 2x_2 & 0 & 0 \\ 1 & 0 & 2x_3 & 0 \\ 2x_1 & 0 & 0 & 2x_4 \end{bmatrix}.$$

Null space of the Jacobian

$$F'(0,0,0,0) = \begin{bmatrix} 1 & 0 & 0 & 0 \\ -2 & 0 & 0 & 0 \\ 1 & 0 & 0 & 0 \\ 0 & 0 & 0 & 0 \end{bmatrix}$$

is generated by the set of vectors $\{(0,1,0,0)^T, (0,0,1,0)^T, (0,0,0,1)^T\}$. The rank deficiency is $q = 3$, so we tested our algorithm with $q = 3, q = 2$, and $q = 1$. The obtained results are given in the following tables.

Table 15show the components of the solution approximation that satisfies the convergence criterion generated by our algorithm with three different starting approximations x_0. The number of iterations required to obtain this approximation is denoted by k, while q is the predicted value of rank deficiency.

Table 15

$x_0 = (0.4, 0.6, 0.6, 0.6)^T$

q	k	$[x_k]_1$	$[x_k]_2$	$[x_k]_3$	$[x_k]_4$	$\|F(x_k)\|$	d_k
1	10	1.219e-13	1.710e-03	2.480e-12	-1.604e-03	4.874e-06	0.5
2	10	-6.392e-23	8.271e-04	8.538e-19	-1.802e-18	9.675e-07	0.5
3	4	1.892e-11	-1.545e-10	3.738e-11	6.029e-10	4.635e-11	1.315e-05

Table 16

$x_0 = (0.3, 0.2, 0.2, 0.2)^T$

q	k	$[x_k]_1$	$[x_k]_2$	$[x_k]_3$	$[x_k]_4$	$\|F(x_k)\|$	d_k
1	9	1.237e-21	7.211e-04	-1.897e-18	6.353e-04	8.389e-07	0.5
2	9	-9.578e-23	7.160e-04	-8.334e-19	8.653e-18	8.389e-07	0.5
3	3	3.685e-11	1.865e-10	2.176e-10	-2.361e-11	9.026e-11	6.221e-06

Table 17

$x_0 = (0.2, 0.05, 0.05, 0.05)^T$

q	k	$[x_k]_1$	$[x_k]_2$	$[x_k]_3$	$[x_k]_4$	$\|F(x_k)\|$	d_k
1	10	-3.066e-24	1.781e-04	-3.252e-19	7.493e-04	5.633e-07	0.5
2	8	3.008e-23	7.152e-04	-2.302e-16	1.790e-16	7.235e-07	0.5
3	3	-1.435e-10	1.282e-10	1.424e-10	-1.173e-12	3.516e-10	8.405e-06

It is clear from the tables above that underestimating the value of q results in the singularity of the bordered system, so the rate of convergence is not the same for all components of the iterative sequence. If the predicted value is $q = 1$ then the second component $[x_k]_2$ and the fourth component $[x_k]_4$ converge slower than the first and third components. Assuming $q = 2$, the convergence of the second component, $[x_k]_2$, is slower than others. In both cases, the slower convergence of mentioned components affects the linear convergence of the whole iterative sequence, indicated by the quotient d_k. When the predicted value is equal to the real value of rank deficiency, i.e., $q = 3$, the superlinear convergence is obtained and all components converge to the solution with the same speed.

The results obtained using the finite-difference method for three starting approximations x_0 are presented in Table 18. The linear convergence resulting from the singularity of the problem in all three cases is indicated by the quotient d_k, as well as the slower convergence of the second, third and fourth components of the iterative sequence. All of these point out that our method is faster than the finite-difference method.

Table 18

x_0	k	$[x_k]_1$	$[x_k]_2$	$[x_k]_3$	$[x_k]_4$	$\|F(x_k)\|$	d_k
$(0.4, 0.6, 0.6, 0.6)^T$	11	-2.671e-23	3.9e-04	3.28e-04	4.48e-04	3.142e-07	0.50316
$(0.3, 0.2, 0.2, 0.2)^T$	10	3.090e-23	3.8e-04	3.87e-04	7.47e-04	6.144e-07	0.502216
$(0.2, 0.05, 0.05, 0.05)^T$	11	1.718e-24	1.07e-04	2.23e-04	4.97e-04	2.530e-07	0.503339

Furthermore, we compared residuals $\|x_k - x^*\|_\infty$ gained with our algorithm and $\|x_k - x^*\|_\infty^{fd}$ when the finite-difference method is applied on a singular system, where x_k is the approximation of the solution that satisfies the stopping criterion. These results are presented in the following table.

Table 19

The residuals

ex	x_0	q	$\|x_k - x^*\|_\infty$	$\|x_k - x^*\|_\infty^{fd}$
1	$(0.5,0.7)^T$	1	7.774e-10	5.183e-04
	$(0.3,0.4)^T$	1	1.852e-12	6.323e-04
	$(0.02,0.02)^T$	1	5.090e-07	6.182e-04
2	$(0.2, 0.5,0.7)^T$	1	8.114e-04	6.973e-04
		2	4.045e-08	
	$(0.1, 0.3,0.5)^T$	1	5.514e-04	4.328e-04
		2	8.379e-11	
	$(0.05, 0.05,0.05)^T$	1	5.354e-04	9.101e-04
		2	1.248e-08	
3	$(0.4, 0.6, 0.6, 0.6)^T$	1	4.277e-04	4.487e-04
		2	8.271e-04	
		3	6.029e-10	
	$(0.3, 0.2, 0.2, 0.2)^T$	1	7.211e-04	7.479e-04
		2	7.160e-04	
		3	2.176e-10	
	$(0.2, 0.05, 0.05, 0.05$	1	7.493e-04	4.975e-04
		2	7.152e-04	
		3	1.435e-10	

Table 19 points out that our derivative-free algorithm is more accurate since the residuals are much smaller than the residuals generated by the finite-difference method. This is the consequence of the regularity of the bordered system.

Moreover, the slower convergence of the components that correspond to the null space affects the slower convergence of the whole iterative sequence obtained by the finite-difference method.

Considering the obtained numerical results, we can conclude that the proposed derivative-free algorithm is faster than the classical finite-difference method. It has better characteristics both in the case when the predicted value of q corresponds to the real value and in the case when the value of q is underestimated. The number of iterations needed for the convergence is smaller when our method is applied and the obtained approximation of the solution is more accurate than the one obtained by the finite-difference method.

Conclusions

A local derivative-free algorithm for solving bordered system and finding a singular solution is compared with the classical finite-difference method for nonlinear systems. It is numerically shown in several examples that left and right singular vectors of the finite-difference approximation of the Jacobian can be used to define the bordered system. Numerical experiments indicate fast local convergence of the proposed method. Moreover, the obtained numerical results point out that our derivative-free method is promising, successful, and has better performances than the classical finite-difference method. Theoretical convergence of the proposed algorithm will be considered in further research.

Acknowledgement

The authors are partially supported by Chair of Mathematics, Department of Fundamental Disciplines, Faculty of Technical Sciences, through the Project ”Teorijska i primenjena matematika u tehničkim i informatičkim naukama” and Project 142-451-2102/2019 of the Provincial Secretariat for Higher Education and Scientific Research.

References

[1] G. Reddien, “On Newton's method for singular problems,” *SIAM Journal on Numerical Analysis,* Vol. 15, No. 5, pp. 993-996, 1978

[2] D. Decker and C. Kelley, “Newton's method at singular points. I,” *SIAM Journal on Numerical Analysis,* Vol. 17, No. 1, pp. 66-70, 1980

[3] D. Decker and C. Kelley, “Newton's method at singular points. II,” *SIAM Journal on Numerical Analysis,* Vol. 17, No. 3, pp. 465-471, 1980

[4] D. Decker, H. Keller and C. Kelley, “Convergence rates for Newton's method at singular points,” *SIAM Journal on Numerical Analysis,* Vol. 20, No. 2, pp. 296-314, 1983

[5] D. Decker and C. Kelley, “Sublinear convergence of the chord method at singular point,” *Numerische Mathematik,* Vol. 42, pp. 147-154, 1983

[6] D. Decker and C. Kelley, “Broyden's method for a class of problems having singular Jacobian at the root,” *SIAM Journal on Numerical Analysis,* Vol. 22, No. 3, pp. 566-573, 1985

[7] C. Kelley and Z. Xue, “Inexact Newton methods for singular problems,” *Optimization Methods and Software,* Vol. 2, No. 3-4, pp. 249-267, 1993

[8] A. Griewank, “On solving nonlinear equations with simple singularities or nearly singular solutions,” *SIAM Review,* Vol. 27, No. 4, pp. 537-563, 1985

[9] C. Kelley and R. Suresh, “A new acceleration method for Newton's method at singular points,” *SIAM Journal on Numerical Analysis,* Vol. 20, No. 5, pp. 1001-1009, 1983

[10] C. Kelley, “A Shamanskii-like acceleration scheme for nonlinear equations at singular point,” *Mathematics of Computation,* Vol. 47, pp. 609-623, 1986

[11] S. Buhmiler, N. Krejić and Z. Lužanin, “Practical Quasi-Newton algorithms for singular nonlinear systems,” *Numerical Algorithms,* Vol. 55, pp. 481-502, 2010

[12] S. Thomas, “Sequential Estimation Techniques for Quasi-Newton Algorithms,” Cornell University, Ithaca, 1975

[13] G. Broyden, “A class of methods for solving nonlinear simultaneous equations,” *Mathematics of Computation,* Vol. 19, pp. 577-593, 1965

[14] J. Martínez, “A quasi-Newton method with modification of one column per iteration,” *Computing,* Vol. 3, pp. 353-362, 1984

[15] R. Schnabel and P. Frank, “Tensor methods for nonlinear equations,” *SIAM Journal on Numerical Analysis,* Vol. 21, No. 5, pp. 815-843, 1984

[16] A. Bouaricha and R. Schnabel, “Tensor methods for large, sparse nonlinear least squares problems,” *SIAM Journal on Scientific Computing,* Vol. 21, pp. 1199-1221, 1999

[17] D. Feng, P. Frank and R. Schnabel, “Local convergence analysis off tensor methods for nonlinear equations,” *Mathematical Programming,* Vol. 62, pp. 427-459, 1993

[18] H. Weber and W. Werner, “On the Accurate Determination of Nonisolated Solutions of Nonlinear Equations,” *Computing,* Vol. 26, pp. 315-326, 1981

[19] A. Griewank and G. Reddien, “Characterization and computation of generalized turning points,” *SIAM Journal on Numerical Analysis,* Vol. 21, No. 1, pp. 176-185, 1984

[20] P. Rabier and G. Reddien, “Characterization and computation of singular points with maximum rank deficiency,” *SIAM Journal on Numerical Analysis,* Vol. 23, No. 5, pp. 1040-1051, 1986

[21] Y. Shen and T. Ypma, "Newton's method for singular nonlinear equations using approximate left and right nullspaces of the Jacobian," *Applied Numerical Mathematics,* Vol. 54, pp. 256-265, 2005

[22] S. Buhmiler, S. Rapajić, S. Medić and T. Grbić, "Finite-difference method for singular nonlinear systems," *Numerical algorithms,* Vol. 79, No. 1, pp. 65-86, 2018

[23] S. Buhmiler, S. Rapajić, M. Lukić, S. Medić, N. Duraković and T. Grbić, "Derivative-free method for singular systems," in *SISY 2019*, Subotica, 2019

Multiple Components Fixed Point Iteration in the Adaptive Control of Single Variable 2nd Order Systems

Hemza Redjimi[†], József K. Tar[†,‡,⋆]

[†]Doctoral School of Applied Informatics and Applied Mathematics,
[‡]University Research, Innovation and Service Center,
Antal Bejczy Center for Intelligent Robotics (ABC iRob),
[⋆]John von Neumann Faculty of Informatics,
Institute of Applied Mathematics,
Óbuda University, H-1034 Budapest, Bécsi út 96/B, Hungary
E-mail: hemza.redjimi@phd.uni-obuda.hu, tar.jozsef@nik.uni-obuda.hu

Abstract: In various fields of applications as robotics, life sciences, chemistry, typical nonlinear systems are controlled for the description of which only imprecise and often partial system models are available and the model-based approaches have to be completed by either robust or adaptive solutions for the compensation of the effects of the models' imperfectness and imprecisions. An alternative approach transformed the control task into a fixed point iteration and tried to solve it in real-time on the basis of Banach's fixed point theorem. This approach does not require complete state estimation. However, it needs feeding back noisy signals that may corrupt the quality of such adaptive controllers. In the preliminary investigations in [1] this multiple variable solution was utilized for the control of a single variable 1st order system so that it yielded some noise filtering possibility. In the present paper this method is extended for the control of single input - single output 2nd order dynamical systems by applying it to shorter time series of the state variable. The operation of this method is investigated via numerical simulations for the control of a strongly nonlinear, oscillating dynamical system, the van der Pol oscillator that further was modified with the introduction of time-delay effects. The simulations are promising.

Keywords: Modeling Errors; Measurement Noise; Adaptive Control; Fixed Point Iteration-based Adaptive Control; Banach Space; van der Pol Oscillator; Time Delay;

1 Introduction

In the adaptive control of nonlinear systems the model linearization around some "point of operation" can work well if the controlled system's actual state dwells in the close vicinity of this point. In more general cases, e.g. in robotics, the dynamic properties of the system drastically vary with the state variables and such a simple

approach is not satisfactory. In such cases the prevailing controller design method is Lyapunov's 2nd or "direct" method he elaborated for the investigation of the stability of motion of nonlinear systems in his PhD Thesis [2]. In the sixties of the past century the translation of his work (originally written in Russian) became known in the western world (e.g. [3]), and after the nineties it became the "number 1 design method" for adaptive controllers. Some relevant early work is for example [4]. The main point in this ingenious design methodology is that though it is impossible to obtain the solution of the equations of motion of the controlled system in "closed analytical form", various stability properties can be defined and guaranteed without knowing all the "details" of the solution. For this purpose sophisticated estimation techniques have been developed.

In spite of the development of the numerical techniques Lyapunov's method is quite relevant in our days since for the description of the behavior of the unstable systems the "validity" of the numerical solutions is always limited in time. With regard to the application of Lyapunov's "estimation techniques", for a given particular problem a particular Lyapunov function has to be constructed, and this function has to be kept between upper and lower limits determined by some "type κ" functions of the norm of the trajectory tracking error. In this manner "global" or "uniformly global" stability properties can be guaranteed. Furthermore, if it can be guaranteed that the time-derivative of the Lyapunov function is "negative enough", "global asymptotic" or "uniformly global asymptotic stability" can be guaranteed. In control technology normally quadratic Lyapunov functions are used for which the asymptotic stability can be proved by the use of Barbalat's lemma (e.g. [5]). In the control systems that suffer from time-delay effects the Lyapunov-Krasovskii functional can be used in the controller design (e.g. [6]) that mathematically corresponds to some extension of the Lyapunov function.

In control applications the Lyapunov function-based design can be criticized from certain practical points of view [7] as follows:

a) it works by meeting *satisfactory conditions* instead of *necessary and satisfactory* ones, therefore "too restrictive" properties have to be proved for its use,

b) in the Lyapunov function-based design approach the main "design intent" is guaranteeing only stability or asymptotic stability without paying appropriate attention to the initial phase of the motion; for instance, in life sciences these "transients" may have lethal consequences, therefore they deserve more attention than that they obtain in this "conventional" design methodology; more precisely, in the resulting control signal some "fragments" of the Lyapunov function normally are present; these fragments contain numerous free parameters for which wide ranges of settings can guarantee the stability (even asymptotic stability), while they considerably influence the initial phase of the motion, too; to achieve appropriate operation these free parameters cannot be "trivially tuned", so their setting may need the application of evolutionary methods (e.g. [8]);

c) the Lyapunov function normally uses each component of the state variable,

so for the application of this methodology these components must be either directly measured or at least estimated; reliable estimation is possible only in the possession of satisfactory number of independent sensor signals; if no such sensors are available –that is a typical situation in life sciences and other technical fields–, such estimations can be made by the use of certain "system models" that themselves are not very precise or reliable; with regard to this problem it is just enough to refer to the different insulin – glucose system models that contain various numbers of compartments (e.g. [9]) or the latest modeling and measuring efforts developed for turbo jet engines (e.g. the utilization of the near magnetic field [10], thermal imaging [11]) for the control of which rather "practical" than mathematically too sophisticated control approaches as the "Situational Control" [12] or robust methods [13] can be applied.

In an alternative technique suggested in [14], the control task was transformed into iteratively finding the solution of a fixed point problem as follows. By the use a purely kinematic design, the appropriate *"Desired"* time-derivative of the generalized coordinate of the system under control (it is referred to as the "relative order of the control task") is calculated by the use of lower order derivatives and the time-integral of the tracking error. Since this derivative abruptly can vary with the control signal, by its use a "slowly meandering" fixed point can be constructed that can be so tracked that during each digital control cycle only one step of the adaptive iteration can be completed. The method's scheme is outlined in Fig. 1. In the box named *"Kinematic Block"* an arbitrary design can be applied for the desired time-derivative of the generalized coordinate. In the case of a first order system the system's response $r(t) \equiv \dot{q}(t)$, and the desired $\dot{q}^{Des}(t)$ has to guarantee that $\left|q^N(t) - q(t)\right| \to 0$ as $t \to \infty$, *if it is realized*. For instance, by using the *integrated tracking error* a PI-type feedback can be constructed by using a constant $\Lambda > 0$ as

$$\left(\frac{\mathrm{d}}{\mathrm{d}t} + \Lambda\right)^2 e_{int}(t) \equiv \left(\frac{\mathrm{d}}{\mathrm{d}t} + \Lambda\right)^2 \int_{t_0}^{t} \left[q^N(\xi) - q(\xi)\right] \mathrm{d}\xi \equiv 0 \quad \Rightarrow \tag{1a}$$

$$\dot{q}^{Des}(t) = \Lambda^2 e_{int}(t) + 2\Lambda e(t) + \dot{q}^N(t) \ , \tag{1b}$$

in which $e(\xi) \stackrel{def}{=} q^N(\xi) - q(\xi)$ is the tracking error, and its integral from t_0 (the commencement of the control action) to the actual time t is given within (1a). It worths noting that further integration of the integrated error in (1) in principle can be used together with a higher power of the operator $\left(\frac{\mathrm{d}}{\mathrm{d}t} + \Lambda\right)$ that could lead to "more fluctuations" in the transient part of the error. However, taking into account that the sequence of multiple integrals can be expressed by a single formula as the *Riemann-Liouville n-fold integral* (e.g. [15]), and that on this basis, by the generalization of this formula, various *fractional order integrals and derivatives* can be introduced that can produce nice monotonic error relaxation, fractional order controllers can be constructed. (A survey on the history of fractional calculus can be found in [16].) The fractional order controllers recently became very popular in robotics (e.g. [17]), in the control of flexible systems (e.g. [18]), in vibration damping (e.g. [19]) and generally in relation with feedback problems (e.g. [20]).

Returning to the scheme depicted in Fig. 1, if the available model is not precise, the $\dot{q}^{Des}(t)$ value is deformed into $\dot{q}^{Def}(t) \neq \dot{q}^{Des}(t)$ to achieve or at least better approximate the $\dot{q}(t) = \dot{q}^{Des}(t)$ situation. This case corresponds to the more precise realization of the tracking strategy formulated in (1). The aim is to approach it via iteration in which $u(t)$ immediately generates the actual $\dot{q}(t)$. Normally in the *"Delay"* boxes only 1 cycle time lag can be calculated that means that the system adaptively learns by computing the deformation in control cycle $n+1$ by considering the applied deformed value and the response obtained for it in cycle n. The iteration can be commenced with $\dot{q}^{Def}(t_{ini}) = \dot{q}^{Des}(t_{ini})$. If the controlled system has well known delay effects, the appropriate delays in these boxes can be modified accordingly, however, because in this case the controller learns from more or less obsolete observed data, some precision degradation in the control can be expected [21].

Mathematically the iterative deformations are calculated on the basis of Banach's fixed point theorem [22] according to which *"in a linear, normed, complete metric space" (i.e. Banach space* $\mathbb{B}$) the sequence generated by the contractive map $\Phi : \mathbb{B} \mapsto \mathbb{B}$ as $\{x_0, x_1 = \Phi(x_0), \ldots, x_{n+1} = \Phi(x_n), \ldots\}$ has a unique limit point $x_\star$ so that $x_n \to x_\star \in \mathbb{B}$. This limit point is a fixed point of $\Phi(x)$, that is $\Phi(x_\star) = x_\star$. By definition $\Phi(x)$ is contractive if $\exists 0 \leq K < 1$ so that $\forall x, y \in \mathbb{B}$ $\|\Phi(x) - \Phi(y)\| \leq K\|x - y\|$. Into the block *"Adaptive Deformation"* an appropriate function must be placed that realizes this contractive map. For higher order control essentially the same structure can be used. For instance, in the case of 2^{nd} order systems as fully actuated robots, PD- or PID-type feedback structures suggested in Fig. 1 can be applied in the *"Kinematic Block"* in the case of the *Resolved Acceleration Rate Control* (e.g. [23]).

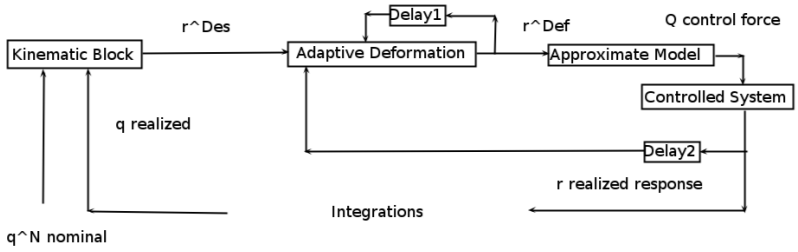

Figure 1
The structure of the *"Fixed Point Transformation-based Adaptive Controller"* (the adaptive deformation can be realized by the use of various fixed point transformations, and the system's response r can be an arbitrary order time-derivative of the generalized coordinates of the controlled system)

However, in our case, the higher order derivative is fed back, too. Such feedback also appears in the *"Acceleration Feedback Controllers"* (e.g. [24]) but in a quite different manner. These cited examples testify that in spite of the expectation that feeding back second time-derivatives may introduce too much noise into the control process, these methods can work. For instance, the above structure was successfully applied in [25] in the realization of the adaptive control of a cheap speed-controlled electric motor manufactured by a Chinese company without having the

precise mathematical model of the motor. The adaptive loop was realized by a simple Arduino embedded microcontroller without using any sophisticated noise filtering technique. For testing adaptivity the rotating axle of the motor was picked by the fingers of the designer so varying the viscous damping in the system in real-time.

In the block *"Adaptive Deformation"* various functions can be placed. In [25] the single variable function introduced in [14] was applied. Later multiple variable functions were introduced by Dineva [26], and an abstract rotations-based software block was suggested in [27] by Csanádi et al. In this approach special orthogonal matrices were applied that were computed according to a generalization of the Rodrigues formula invented in 1840 [28] in the following manner. In the case of a vector transformation $b \in \mathbb{R}^n$ to vector $a \in \mathbb{R}^n$ ($\|a\| \neq \|b\|$), via introducing a *"buffer dimension"* the vectors $B \in \mathbb{R}^{n+1}$ and $A \in \mathbb{R}^{n+1}$ can be introduced with the components: for $s \in \{1,\ldots,n\}$, $B_s = b_s$, $A_s = a_s$, and $B_{n+1} = \sqrt{R^2 - \|b\|^2}$, $A_{n+1} = \sqrt{R^2 - \|a\|^2}$. Evidently, $\|A\| = \|B\|$, therefore in the $n+1$ dimensional space these vectors can be rotated into each other. Furthermore, in the $n+1$ dimensional space the rotation operator that rotates B into A can be easily constructed (the details were published in [27], and a simple interpolation between the two positions can be obtained by a factor $\lambda_a \in [0,1]$ by rotating with $\lambda_a \varphi$ instead of φ that is the angle between the two vectors.

The noise sensitivity of the method generally can be reduced by various noise filtering techniques that can apply smoothed signals in the *"Kinematic Block"* for the calculation of the "Desired" time-derivatives, and for smoothing the observed response, too. In the present paper the idea that was investigated for a 1st order single variable system in [1] is extended to the adaptive control of a 2nd order one with the calculation of the *"desired"* 2nd order derivatives from pre-filtered terms. The paper is structured as follows: in Section 2 the dynamic model of the controlled system is detailed. Section 3 reveals the simulation results. The paper is closed with the conclusions and the acknowledgement section.

2 The Dynamic Model of the van der Pol Oscillator

In 1927 van der Pol modeled the nonlinear oscillations of an externally excited triode [29]. This model later served as a popular paradigm of nonlinear systems in control technology because it had an unstable equilibrium point in the state $q(0) = 0$, $\dot{q}(0) = 0$. If some small external perturbation kicks the system's state out of this equilibrium point, it produces nonsinusoidal oscillations that have to be "curbed" by the controller. In this paper this model is considered to be a "mathematical construction" only with a nondimensional "generalized coordinate" $q(t)$, and physical interpretation is given only to the variable of time t measured in $[s]$ units. In similar manner, the control signal $u(t)$ remains without physical interpretation. The original van der Pol model is further modified by the introduction of some delay time τ in the equations of motion given in (2). Certain parameters have some "physical analogy" like the *"inertia"*, the *"spring stiffness"* and the *"damping parameter"*. The *"separator parameter" a* determines the border between excitation and damping the strength of which is determined by parameter b_1. Parameter b_2 corresponds

to the traditional viscous damping model.

$$\ddot{q}(t) = \frac{-kq(t-\tau) + b_1\left(q(t-\tau) - a^2\right)\dot{q}(t-\tau) - b_2\dot{q}(t-\tau) + u(t)}{m} \quad , \tag{2}$$

with the parameter values given in Table 1.

Table 1
The system parameters (the "Exact" values), and the "Approximate" values utilized in the simulations

System	**Dynamic Parameters**		
Model	***Parameter***	***Exact Val.***	***Approx. Val.***
k	"Spring stiffness"[a]	150.0	100.0
m	"Inertia"[a]	1.5	1.0
τ	Delay time (s)	6×10^{-3}	10×10^{-3}
a	Separator [a]	1.2	1.0
b_1	Excitation/Damping parameter [a]	1.5	1.0
b_2	"Damping parameter" [a]	2.5	2.0
δt	Cycle time (s)	0.001	Not applicable

[a]The units are compatible with (2).

For using this model, *in the simulations* the exact q, $\dot{q}$ values were considered by applying Euler integration utilizing the $\ddot{q}$ value provided by the *exact dynamic model of the system*. For the controller the noisy observed value of $q(t)$ denoted by $\tilde{q}(t)$ was used as an input. It was simulated by the Julia language code as

"`q_noisy_mem[i]=q[i]+NoiseAmpl*2*(0.5-rand())`"

in which even noise distribution was applied. This noisy value was filtered as $\overline{\tilde{q}(t)}$ by minimizing the following quadratic error in the digital control step i according to a_0, a_1, and a_2, and using the filtered values as in (3b) and (3c).

$$S \stackrel{def}{=} \sum_{s=1}^{L}\left(\sum_{\ell=0}^{2} a_\ell s^\ell - \tilde{q}(i-L+s)\right)^2 \tag{3a}$$

$$\overline{\tilde{q}}(i) = \sum_{\ell=0}^{2} a_\ell L^\ell \ , \ldots, \ \overline{\tilde{q}}(i-L+1) = \sum_{\ell=0}^{2} a_\ell 1^\ell \tag{3b}$$

$$\dot{\overline{\tilde{q}}}(i) \approx \frac{\overline{\tilde{q}}(i) - \overline{\tilde{q}}(i-1)}{\delta t} \quad . \tag{3c}$$

In the possession of the filtered $\left\{\overline{\tilde{q}}(i), \ldots, \overline{\tilde{q}}(i-1)\right\}$ and the "desired" $\ddot{q}^{Des}(i)$ ***for the desired next step*** $q^{NextDes}(i+1)$ the approximation in (4)was applied.

$$\ddot{q}^{Des}(i) \approx \frac{q^{NextDes}(i+1) - 2\overline{\tilde{q}}(i) + \overline{\tilde{q}}(i-1)}{\delta t^2} \text{ leading to} \tag{4a}$$

$$q^{NextDes}(i+1) = \ddot{q}^{Des}(i)\delta t^2 + 2\overline{\tilde{q}}(i) - \overline{\tilde{q}}(i-1) \quad . \tag{4b}$$

From the "deformed buffer" the "deformed 2nd time-derivative" was approximated as

$$\ddot{q}^{Def}(i) \approx \frac{q^{Def}(L) - 2q^{Def}(L-1) + q^{Def}(L-2)}{\delta t^2} \quad . \tag{5}$$

In the sequel simulation results will be presented.

3 Simulation Results

The numerical estimations applied in Section 2 are mathematically justified if the buffer length L is small enough in the sense that during the time interval of length $L\delta t$ the variation of the state in the free motion of the system to be controlled, that of the nominal trajectory to be tracked, and the variation of the unknown external disturbances "of no stochastic origin" are not very significant. If the controller can work under such conditions the effects of the stochastic noises can be investigated in a next step. Since for the calculation of the 2nd time-derivatives at least 3 measured values are necessary, the *minimal reasonable buffer length* that can make some filtering is about 5.

3.1 Investigation of The Effects of The Buffer Length in Noise-free Cases

Figures 2 and 3 reveal that the modeling errors and the external disturbances of non-stochastic origin with the PID-type control of $\Lambda = 2s^{-1}$ result in poor trajectory tracking in the case of the non adaptive controller. With the adaptive parameters $R = 10^4$ and $\lambda_a = 0.9$ the "adaptive counterparts" of these diagrams are given in Figs. 4 and 5. Figure 6 reveals more finer details on the operation of the adaptive controller: the adaptive deformation is considerable and almost perfectly guarantees the realization of $\ddot{q}^{DesFilt}$. The $L = 5$ buffer length evidently does not cause considerable obsolescence in the calculation of the adaptive deformation.

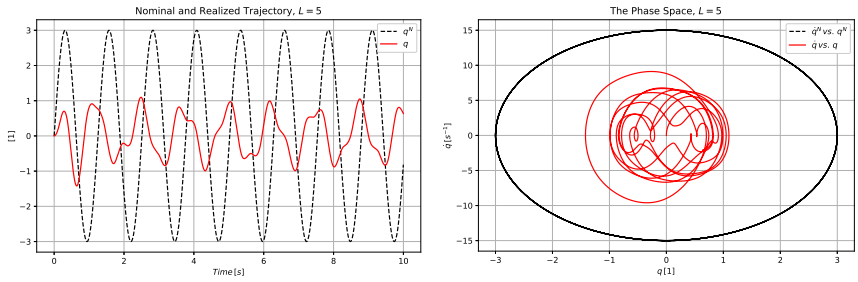

Figure 2
The trajectory and phase trajectory tracking of the non adaptive controller for a PID control with $\Lambda = 2s^{-1}$ with the buffer length $L = 5$

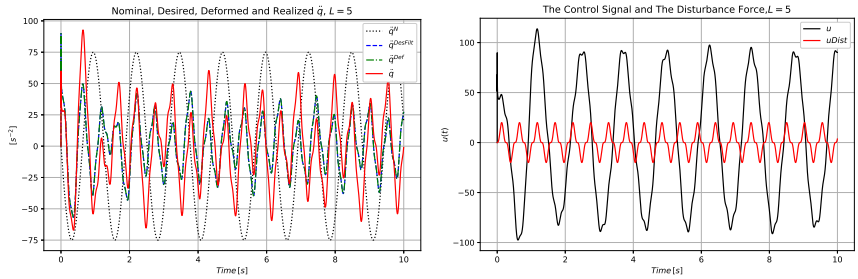

Figure 3
The 2nd time-derivatives and the control forces of the non adaptive controller for a PID control with $\Lambda = 2\,s^{-1}$ with the buffer length $L = 5$

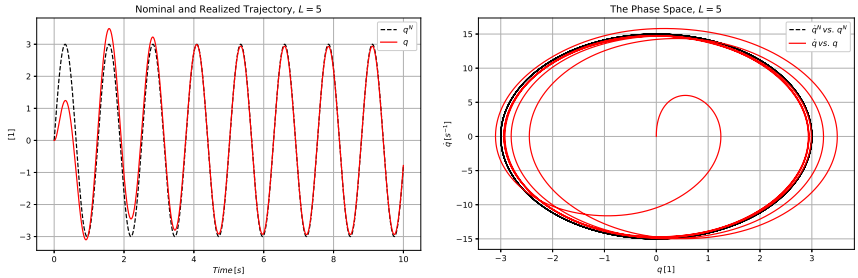

Figure 4
The trajectory and phase trajectory tracking of the adaptive controller for a PID control with $\Lambda = 2\,s^{-1}$ with the buffer length $L = 5$

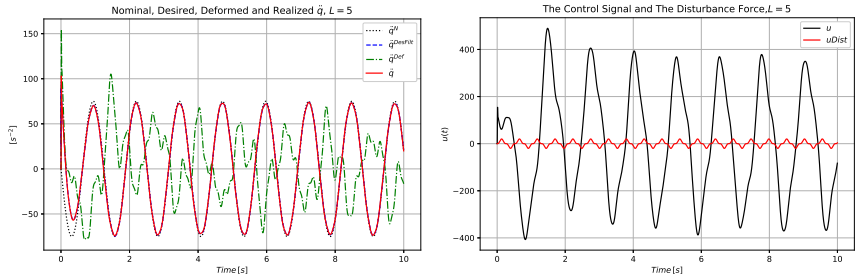

Figure 5
The 2nd time-derivatives and the control forces of the adaptive controller for a PID control with $\Lambda = 2\,s^{-1}$ with the buffer length $L = 5$

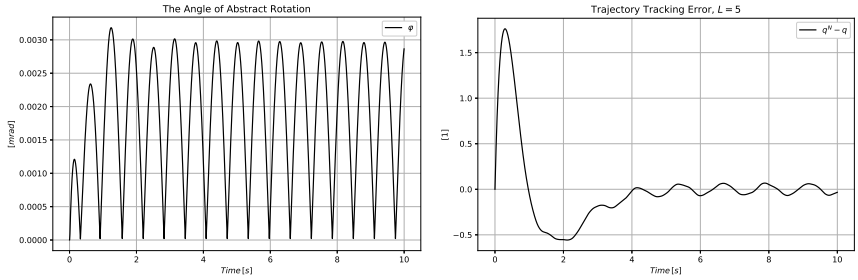

Figure 6
The angle of the abstract rotation and the trajectory tracking error of the adaptive controller for a PID control with $\Lambda = 2\,s^{-1}$ with the buffer length $L = 5$

If the buffer length is increased to $L = 25$, according to Fig. 7 the behavior of the nonadaptive controller shows drastic modification. The same can be stated for the adaptive controller according to the Fig. 8. So the buffer length $L = 25$ is evidently too large for these dynamical signals.

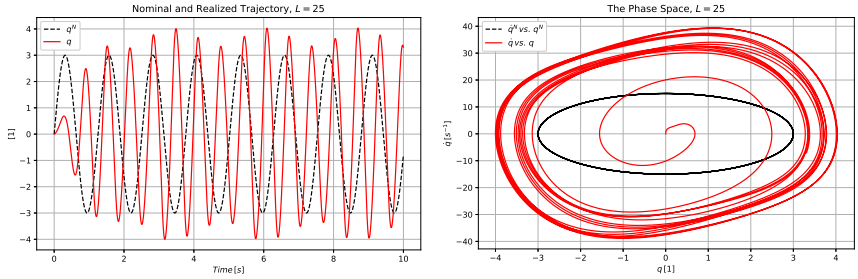

Figure 7
The trajectory and phase trajectory tracking of the non adaptive controller for a PID control with $\Lambda = 2\,s^{-1}$ with the buffer length $L = 25$

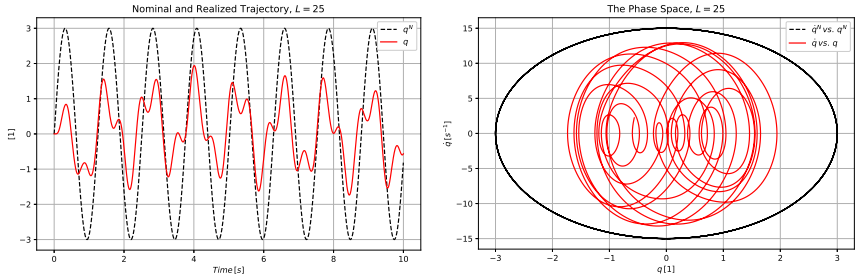

Figure 8
The trajectory and phase trajectory tracking of the adaptive controller for a PID control with $\Lambda = 2\,s^{-1}$ with the buffer length $L = 25$

Decreasing the buffer length to $L = 10$ provides rather acceptable result for the adaptive controller as it is revealed by Fig. 9, while according to Fig. 10 the non adaptive controller remains quite inappropriate.

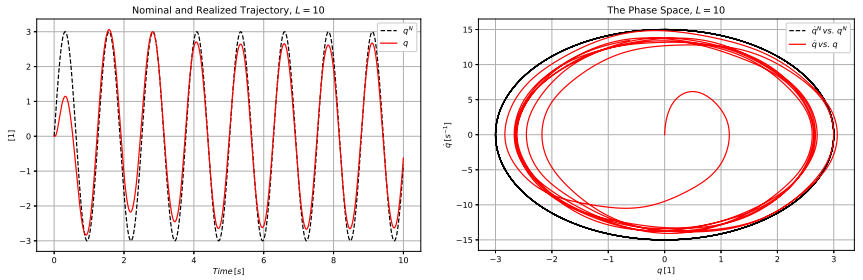

Figure 9
The trajectory and phase trajectory tracking of the adaptive controller for a PID control with $\Lambda = 2\,s^{-1}$ with the buffer length $L = 10$

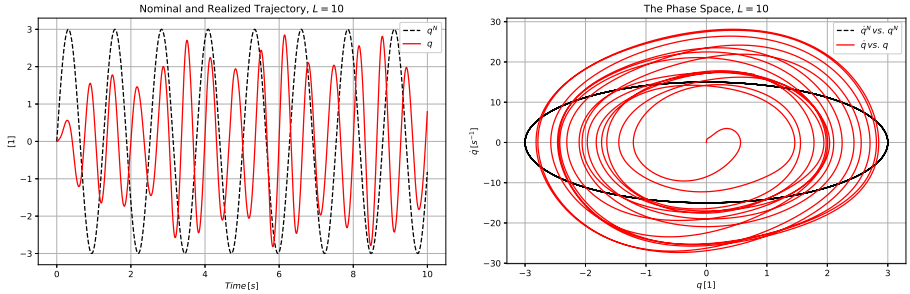

Figure 10
The trajectory and phase trajectory tracking of the non adaptive controller for a PID control with $\Lambda = 2\,s^{-1}$ with the buffer length $L = 10$

Following these preparations it seems to be expedient for considering the additional effects of measurement noises for the buffer lengths $L = 5$ and $L = 10$.

3.2 Investigation of The Effects of Measurement Noises

In these investigations the noise amplitude was selected to be 0.02. Figure 11 reveals that the non-adaptive controller is quite inappropriate, while according to Fig. 12 the adaptive solution behaves quite well.

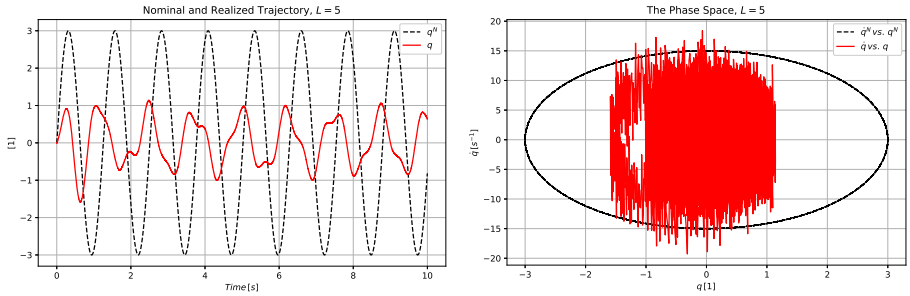

Figure 11
The trajectory and phase trajectory tracking of the non adaptive controller for a PID control with $\Lambda = 2s^{-1}$ with the buffer length $L = 5$ in the case of measurement noises

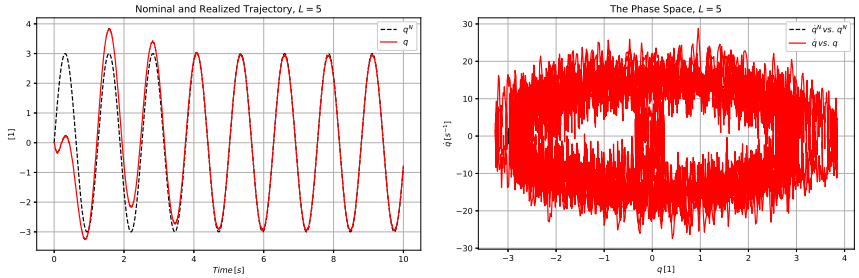

Figure 12
The trajectory and phase trajectory tracking of the adaptive controller for a PID control with $\Lambda = 2s^{-1}$ with the buffer length $L = 5$ in the case of measurement noises

To the buffer length $L = 10$ Figs. 13, 14, and 15 belong. The adaptive controller evidently was found to be more precise than the non adaptive one, in spite of the noisy feedback.

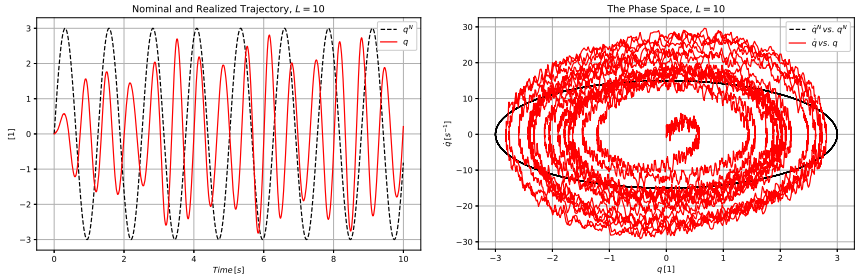

Figure 13
The trajectory and phase trajectory tracking of the non adaptive controller for a PID control with $\Lambda = 2s^{-1}$ with the buffer length $L = 10$ in the case of measurement noises

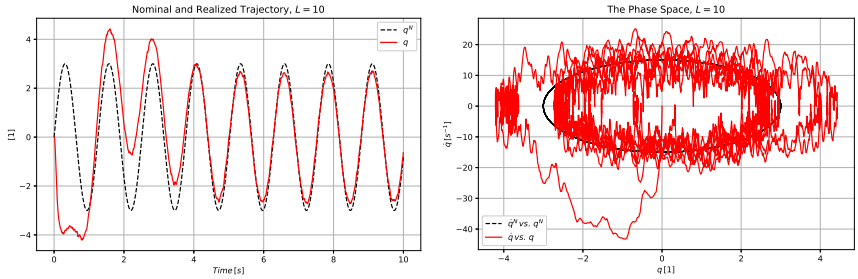

Figure 14
The trajectory and phase trajectory tracking of the adaptive controller for a PID control with $\Lambda = 2\,s^{-1}$ with the buffer length $L = 10$ in the case of measurement noises

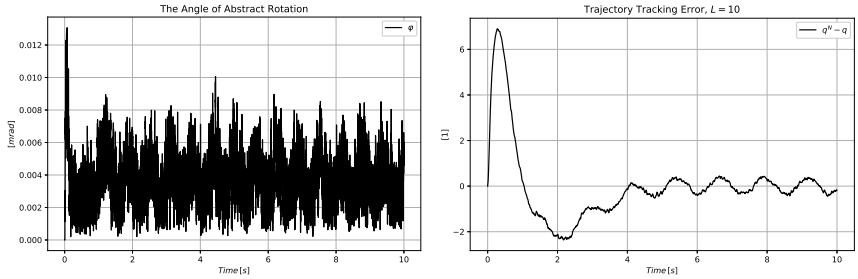

Figure 15
The angle of the abstract rotation and the trajectory tracking error of the adaptive controller for a PID control with $\Lambda = 2\,s^{-1}$ with the buffer length $L = 10$ in the case of measurement noises

For a better comparison it makes sense to consider the 2$^{\text{nd}}$ time-derivatives and the control signals. Figures 16 and 17 reveal that both the 2$^{\text{nd}}$ time-derivatives and the control signals varied in the same order of magnitude.

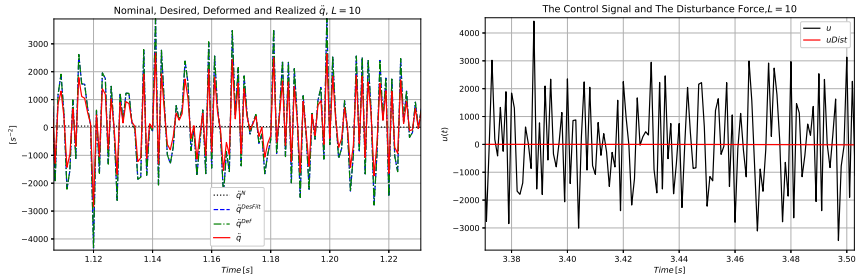

Figure 16
The 2$^{\text{nd}}$ time-derivatives and the control forces of the non adaptive controller for a PID control with $\Lambda = 2\,s^{-1}$ with the buffer length $L = 10$ in the case of measurement noises (zoomed in excerpts)

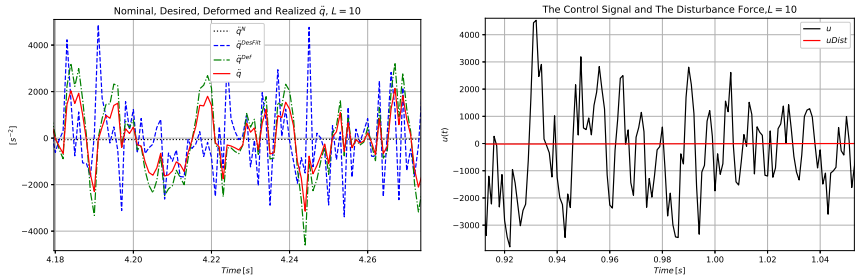

Figure 17
The 2nd time-derivatives and the control forces of the adaptive controller for a PID control with $\Lambda = 2\,s^{-1}$ with the buffer length $L = 10$ in the case of measurement noises (zoomed in excerpts)

It can be guessed that the division by δt^2 in the estimation of the 2nd time-derivatives may cause huge values, and consequently, huge control signal values. It was interesting to see what happens if the time-resolution is reduced by using $\delta t = 10^{-2}\,s$ and simultaneously the buffer length is reduced to $L = 5$. According to Figs. 18, 19, and 20 the rougher time-resolution made the adaptive controller better because considerably smaller control signal were applied in the calculations. Figures 21, and 22 testify that the non adaptive controller provides less precise tracking though the control signals and the 2nd time-derivatives are of the same order of magnitude in the adaptive and the nonadaptive cases.

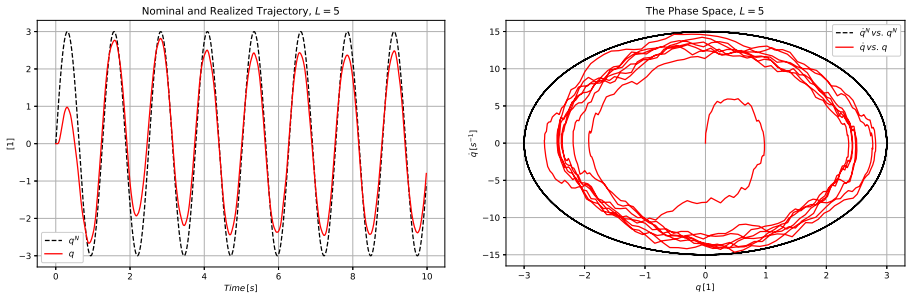

Figure 18
The trajectory and phase trajectory tracking of the adaptive controller for a PID control with $\Lambda = 2\,s^{-1}$ with the buffer length $L = 5$ in the case of measurement noises using $\delta t = 10^{-2}\,s$

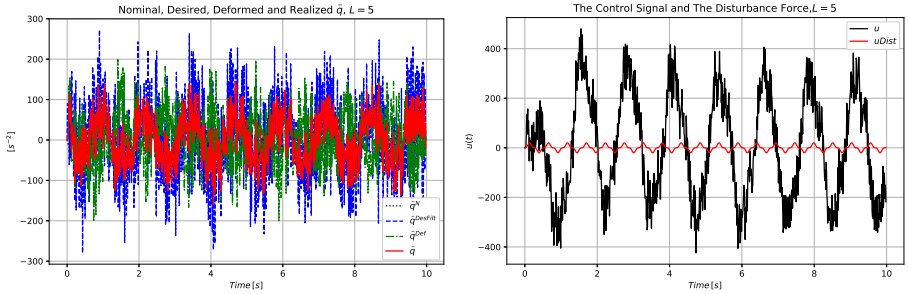

Figure 19
The 2nd time-derivatives and the control forces of the adaptive controller for a PID control with $\Lambda = 2\,s^{-1}$ with the buffer length $L = 5$ in the case of measurement noises using $\delta t = 10^{-2}\,s$

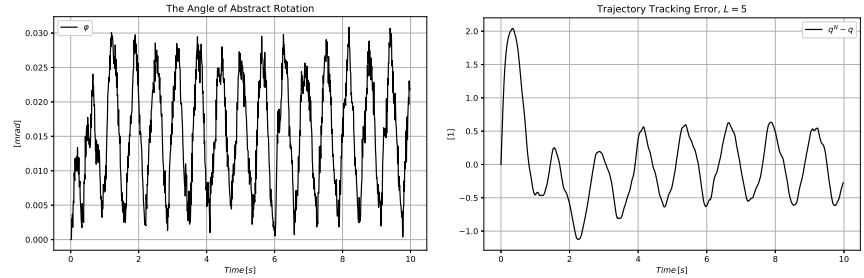

Figure 20
The angle of the abstract rotation and the trajectory tracking error of the adaptive controller for a PID control with $\Lambda = 2\,s^{-1}$ with the buffer length $L = 5$ in the case of measurement noises using $\delta t = 10^{-2}\,s$

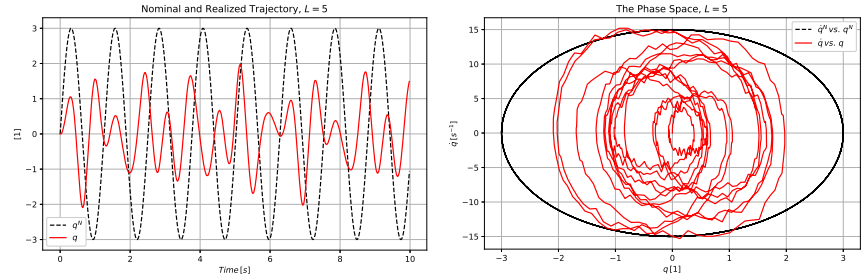

Figure 21
The trajectory and phase trajectory tracking of the non adaptive controller for a PID control with $\Lambda = 2\,s^{-1}$ with the buffer length $L = 5$ in the case of measurement noises using $\delta t = 10^{-2}\,s$

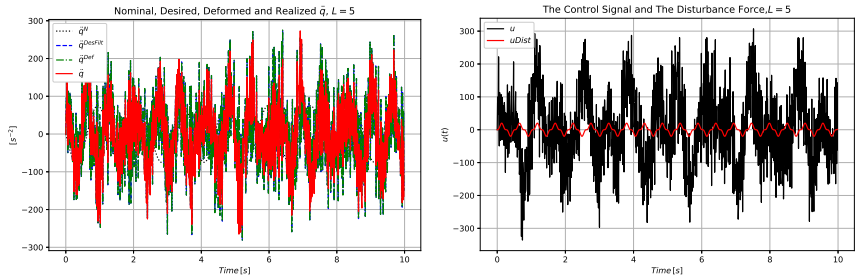

Figure 22
The 2nd time-derivatives and the control forces of the non adaptive controller for a PID control with $\Lambda = 2\,s^{-1}$ with the buffer length $L = 5$ in the case of measurement noises using $\delta t = 10^{-2}\,s$

3.2.1 Conclusions

In this paper, following the the preliminary investigations in [1] that considered the possible use of multivariable fixed point transformations in the adaptive control of single variable 1st order dynamical systems with some special noise filtering technique, the investigations were extended to 2nd order dynamical systems. For this purpose the van der Pol oscillator model was modified with the inclusion of time-delay effects.

As a conclusion it can be stated that in spite of the fact that the fixed point iteration-based method feeds back the noisy 2nd derivatives that are estimated by the controller in a finite element approximation, the operation of the adaptive solution is superior to the nonadaptive one that feeds back only lower order, therefore less noisy numerically estimated time-derivatives.

It can be concluded, too, that it is expedient tho choose the possible roughest discrete time resolution that can be allowed by the dynamics of the nominal motion to be tracked, and by the kinematically calculated PID-type error feedback correction terms to keep the occurring control signals at some low, realistic level. Any refinement in the time resolution increases the amplitude of the fluctuating control signal that is similar to the chattering effect occurring in the Robust Variable Structure / Sliding Mode Controllers.

3.2.2 Acknowledgement
This work was supported by the *Doctoral School of Applied Informatics and Applied Mathematics* of Óbuda University.

References

[1] H. Redjimi and J. K. Tar, The Use of Multiple Components Fixed Point Iteration in the Adaptive Control of Single Variable Systems, In Proc. of the 2019 IEEE 17th International Symposium on Intelligent Systems and Informatics (SISY), Subotica, Serbia, 2019, pp. 000267-000272

[2] A.M. Lyapunov, A General Task about the Stability of Motion. (in Russian), Ph.D. Thesis, University of Kazan, Tatarstan (Russia), 1882

[3] A.M. Lyapunov, Stability of Motion, Academic Press, New-York and London, 1966

[4] Jean-Jacques E. Slotine and W. L, Applied Nonlinear Control, Prentice Hall International, Inc., Englewood Cliffs, New Jersey, 1991

[5] M. Hou, G. Duan, and M. Guo, New versions of Barbalat's lemma with applications, J. Control Theory Appl, 2010, Vol. 8, No. 14, pp. 545-547

[6] V.B. Kolmanovskii, S.-I. Niculescu, and D. Richard, On the Lyapunov-Krasovskii functionals for stability analysis of linear delay systems, International Journal of Control, 1999, Vol. 72, No. 4, pp. 374-384

[7] J.K. Tar, J.F. Bitó, and I.J. Rudas, Replacement of Lyapunov's Direct Method in Model Reference Adaptive Control with Robust Fixed Point Transformations, In Proc. of the 14^{th} IEEE Intl. Conf. on Intelligent Engineering Systems, Las Palmas of Gran Canaria, Spain, 2010, pp. 231-235

[8] I. Sekaj and V. Veselý, Robust Output Feedback Controller Design: Genetic Algorithm Approach, IMA J Math Control Info, 2005, Vol. 22, No. 3, pp. 257-265

[9] E. Friis-Jensen, Modeling and Simulation of Glucose-Insulin Metabolism, PhD Thesis, Technical University of Denmark, Kongens Lyngby, Denmark, 2007

[10] R. Andoga and L. Főző, Near Magnetic Field of a Small Turbojet Engine. Acta Physica Polonica, 2017, Vol. 131, No. 4, pp. 1117-1119

[11] R. Andoga, L. Főző, M. Schrötter, M. Češkovič, S. Szabo, R. Bréda, and M. Schreiner, Intelligent thermal imaging-based diagnostics of turbojet engines. Applied Sciences, 2019, Vol.9, No. 2253, pp. 1-22 9(2253):1–22

[12] R. Andoga, L. Főző, J. Judičák, R. Bréda M., S. Szabo, R. Rozenberg, and M. Džunda, Intelligent situational control of small turbojet engines. International Journal of Aerospace Engineering, 2018 (Article ID 8328792), pp. 1–16

[13] R. Andoga, L. Főző, R. Kovács, K. Beneda, T. Moravec, and M. Schreiner, Robust control of small turbojet engines. Machines, 2019, Vol. 7, No. 3, pp. 1–14

[14] J.K. Tar, J.F. Bitó, L. Nádai, and J.A. Tenreiro Machado, Robust Fixed Point Transformations in Adaptive Control Using Local Basin of Attraction, Acta Polytechnica Hungarica, 2009, Vol. 6, No. 1, pp. 21-37

[15] J. Munkhammar, Riemann-Liouville Fractional Derivatives and the Taylor-Riemann Series, Department of Mathematics, Uppsala University, Sweden, 2004

[16] J.A. Tenreiro Machado and V. Kiryakova, The Chronicles of Fractional Calculus, Fract. Calc. Appl. Anal, 2017, Vol. 20, No. 2, pp. 307-336

[17] J.A. Tenreiro Machado and B.P. Moghaddam, A Robust Algorithm for Nonlinear Variable-Order Fractional Control Systems with Delay, International

Journal of Nonlinear Sciences and Numerical Simulation, 2016, Manuscript ID: IJNSNS.2016.0094, pp. 1-7

[18] Silviu Folea, Robin De Keyser, Isabela R. Birs, Cristina I. Muresan, and Clara Ionescu, Discrete-Time Implementation and Experimental Validation of a Fractional Order PD Controller for Vibration Suppression in Airplane Wings, Acta Polytechnica Hungarica, 2017, Vol. 14, No. 1, pp. 191-206

[19] P. Lanusse, T. Poinot, O. Cois, A. Oustaloup, and J.C. Trigeassou, Tuning of an Active Suspension System using a Fractional Controller and a Closed-Loop Tuning, In Proc. of the 11th International Conference on Advanced Robotics (ICAR 2003), Coimbra, Portugal, 2003, pp. 258-263

[20] H. Redjimi and J.K. Tar, Extrapolated State Estimation in Fixed Point Transformation-based Adaptive Control Using Fractional Order Feedback, In Proc. of the IEEE 16th World Symposium on Applied Machine Intelligence and Informatics, February 7-10, 2018, Košice, Herl'any, Slovakia, pp. 27-32

[21] H. Redjimi and J.K. Tar, On the Effects of Time-Delay on Precision Degradation in Fixed Point Transformation-based Adaptive Control, In the Proc. of the 2017 IEEE 30th Jubilee Neumann Colloquium, November 24-25, 2017, Budapest, Hungary, pp. 125-130

[22] S. Banach, Sur les opérations dans les ensembles abstraits et leur application aux équations intégrales (About the Operations in the Abstract Sets and Their Application to Integral Equations) Fund. Math, 1922, Vol. 3, pp. 133-181

[23] Behzad Dariush, Ghassan Bin Hammam, and David Orin, Constrained Resolved Acceleration Control for Humanoids, In Proc. of the 2010 IEEE/RSJ International Conference on Intelligent Robots and Systems, October 18-22, 2010, Taipei, Taiwan, pp. 710-717

[24] Qiang Wang, Hua-Xiang Cai, Yong-Mei Huang, Liang Ge, Tao Tang, Yan-Rui Su, Xiang Liu, Jin-Ying Li, Dong He, Sheng-Ping Du, and Yu Ling, Acceleration feedback control (AFC) enhanced by disturbance observation and compensation (DOC) for high precision tracking in telescope systems, Research in Astronomy and Astrophysics, 2016, Vol. 16, No. 8, p. 124

[25] T. Faitli, Investigation of Control Methods for a Speed-controlled Electric Motor (BSc Thesis, Supervisor: J.K. Tar), Óbuda University, Donát Bánki Faculty of Mechanical and Safety Engineering, Institute of Mechatronics and Autotechnics, Budapest, Hungary, 2018

[26] A. Dineva, J.K. Tar, and A.R. Várkonyi-Kóczy, Novel Generation of Fixed Point Transformation for the Adaptive Control of a Nonlinear Neuron Model, In proc. of the IEEE International Conference on Systems, Man, and Cybernetics, October 10-13, 2015, Hong Kong, pp. 987-992

[27] B. Csanádi, P. Galambos, J.K. Tar, Gy. Györök, and A. Serester, In the Proc. of the 2018 IEEE International Conference on Systems, Man, and Cybernetics (SMC2018), October 7-10, 2018, Miyazaki, Japan, pp. 2577-2582

[28] O. Rodrigues, Des lois géometriques qui regissent les déplacements d' un systéme solide dans l' espace,et de la variation des coordonnées provenant de ces déplacement considérées indépendent des causes qui peuvent les produire (Geometric laws which govern the displacements of a solid system in space: and the variation of the coordinates coming from these displacements considered independently of the causes which can produce them), J. Math. Pures Appl, 1840, Vol. 5, pp. 380-440

[29] B. van der Pol, Forced oscillations in a circuit with non-linear resistance (reception with reactive triode), The London, Edinburgh, and Dublin Philosophical Magazine and Journal of Science, 1927, Vol. 7, No. 3, pp. 65-80

Indoor Atlas Service as a Tool for Building an Interior Navigation System

Martin Štancel, Ján Hurtuk, Michal Hulič, Jakub Červeňák

Department of Computers and Informatics, Faculty of Electrical Engineering and Informatics, Technical University of Košice
Letná 9, 04001 Košice, Slovak Republic
martin.stancel@tuke.sk, jan.hurtuk@tuke.sk, michal.hulic@tuke.sk, jakub.cervenak@student.tuke.sk

Abstract: Indoor navigation is a technology challenge relatively difficult to tackle. This paper examines and describes the implementation of a new approach to indoor navigation using the IndoorAtlas service, which was used to design and implement a prototype application. This is based on the positioning of mobile phone devices, and with the help of the aforementioned service, specific properties of the building are obtained – these include the magnetic fingerprints, a result of the interaction of the Earth's magnetic field with the ferromagnetic materials used in the construction of buildings. In our case, this service was used in correlation with the Java programming language for the Android platform. The publication also contains experiments carried out on the premises of the selected building. Several main measures were made. In the selected environment, the completed measurements demonstrated, that the proposed application fullfils the criteria of a fully functional indoor navigation, with average deviation within the parameters specified by the manufacturer.

Keywords: indoor navigation; IndoorAtlas; geomagnetic localization; shortest path algorithms

1 Introduction

Over the past few decades, satellite positioning systems have proven to be a reliable and highly accurate outdoor navigation tool. This trend has forced the market to focus also on indoor positioning, to allow navigation in buildings and similar spaces. Even today, this kind of navigation is still a big challenge and there are still no reliable and sufficiently precise technical solutions in this respect. Therefore, the question is: what makes outdoor and indoor navigation so different, when – in theory – most positioning systems use a similar principle and could be used not only for outdoor but also for indoor purposes. In fact, the indoor use of outdoor positioning systems presents completely different and inconsistent results,

and, in certain cases, outdoor navigation systems cannot even be applied indoors. From a technical point of view, indoor navigation is much more complex due to the reasons as objects in the rooms, such as furniture and the walls themselves, contribute to significant signal reflections, non-life-of-sight conditions [1], high attenuation, dispersion and possible reflection of the signal due to higher obstacle density, short-term signal changes due to the presence of humans, pets, etc. (repositioning of furniture, new furnishings, opening and closing of doors, etc.) and very high demands on measurement accuracy.

On the other hand, it can be stated that the issue of indoor positioning also has some positive aspects. The area used for positioning is significantly smaller. It can be stated, that temperature fluctuations are not as significant, for normally, room temperature is within a certain – almost constant – range. The geometry of the mapped rooms – with the exception of furnishings and other inserted objects can be considered as simple (perpendicular walls, etc.). Compared to car-based navigation systems, it uses slower speeds and dynamics – by at least an order of magnitude.

From a research point of view, indoor navigation is also of great interest due to the lack of sufficient indoor results produced by today's dominant outdoor positioning technology – GNSS. There is no indoor positioning system achieving the excellent global outdoor results of GNSS, high accuracy, short signal delays, high availability, high-level of integration and low setup costs. Several different approaches have been made including Chaur-Heh Hsieh At al. [2] who developed four deep neural networks implemented with multi-layer perceptron (MLP) [3] [4] and one-dimensional convolutional neural network (1D-CNN) to estimate the location of a subject in a room.

Creating a navigation system to overcome the aforementioned deficiencies requires a device – in this case, an intelligent device (mobile phone, tablet) containing the necessary sensors to determine the location while guaranteeing users the simplicity, comfort, availability and – especially – the accuracy of measurement. Most modern phones have a built-in accelerometer, light sensors, and sensors capable of detecting magnetic fields [5]. These sensors are monolithic and mutually independent, unlike sensors connected into a network of distributed, mutually dependent or mutually interacting sensors. These built-in sensors have great potential for developing diverse applications.

The purpose of this paper is to present the proposed indoor navigation system for the Android platform, having low setup and operating costs. The presented application would allow to determine the indoor position of the user and navigate users through the indoor space, according to the selected parameters. The proposed indoor navigation solution will consist of two logically separated parts: device positioning and calculation of the shortest route from source to destination. Development of the aforementioned interior navigation system can be divided into several steps:

- analysis of available technology used for indoor positioning,
- analysis of suitable shortest-path-calculation algorithms,
- design of an indoor navigation solution using the IndoorAtlas API [6], based on magnetic fingerprinting – mapping of unique magnetic profiles resulting from the interaction of the Earth's magnetic field with steel and other ferromagnetic materials used in the construction of modern buildings,
- implementation of the proposed solution,
- evaluation of functionality using real-world testing.

2 Related Works

The technology used so far to solve the problem of indoor positioning can be divided into three categories, representing three different physical principles as inertial positioning using an accelerometer and a gyroscope to meter angular momentum, positioning technology based on mechanical waves using (ultra)sound or positioning technologies based on electromagnetic waves using optical, infrared, microwave and radio spectrum. Several papers have been developed to research these various approaches, document their pros and cons, and ultimately develop systems based on previously mentioned technologies in order to confirm the main functionality. Detailed comparisons of the existing technologies are made in [11], [19], [21], [22].

2.1 Positioning Technologies Using Camera Systems

Optical indoor positioning systems can be categorized as egomotion systems [7] obtaining the position of a moving camera, or static systems in which the camera determines the positions of objects moving in the images. As the application is designed for smartphones supporting the Android platform, we will focus on egomotion systems. One of these systems is the Mobile Visual Indoor Positioning System [8] using a distributed architecture. The mobile application creates photos of its surroundings and then sends them to a server that compares the submitted photos with a database of properly localized and oriented photographs of the environment, taken during the initial calibration phase. The server component uses the Speeded Up Robust Features comparison algorithm [9], which provides fast, memory-efficient extraction and description of recognition points from a local photograph. After executing the algorithm, the server component has the most probable photograph, including points of interest and a reference photograph stred in the database. Since the position of the reference photo, stored in the database,

usually differs from the position where the current photograph was taken from, a geometric correction scheme is applied. This is based on the application of a formula stating that the distance between two photographs of the same object taken from different distances from the object is proportional to the distance of the two points on the photograph. The mobile app does not depend on specific infrastructure. The whole system can be presented as cheap and relatively efficient. On the other side, the system for its functionality needs a series of photos with a high amount of recognizable points for exact positioning. Therefore, it is not sufficient to use it with positioning situated in open empty spaces. Another disadvantage lies in bad light conditions presented on mentioned photographs and in situations, where the scene can be often changed (e.g. furniture position changing).

2.2 Positioning Based on LED Lighting

A solution based on this technology is Philips Indoor Positioning. This system uses LED lamps producing energy-efficient and high-quality light, while using Philips Visible Light Communication [10] technology to transmit unique codes [11], which are then detected by the smartphone. The accuracy of positioning depends on the accuracy of the light sensor tilt angle metering. This system modulates the intensity of the optical LED light to transmit data and receives light through the light sensor of the mobile phone. Data from different light sources can be received at the same time. This is possible due to the spatial separation of the light rays emitted by various LED sources using lenses, provided that the light sensor is directed towards the light source. The system also consists of the control software and the cloud solution, which can identify code and therefore computes the exact position of the smartphone. Aside from the system mentioned above, Philips comes with Indoor Positioning System, which uses BTLE (Bluetooth Low Energy) sensors. These sensors are used to in-pocket notifications for route tracking, even without the need for active use of the mobile phone [11]. Positioning based on LED lightning represents one of the most reliable solutions because the radio and electromagnetic interferences do not have any impact on system stability. One of the huge disadvantages lies, however, in relatively huge costs connected to realization.

2.3 Positioning Mechanism Using Inertial Force

This system [12] is based on the capabilities of modern mobile phones equipped with an accelerometer, a compass, a camera, and an Internet connection. The data read from the smartphone sensors, in conjunction with the location map, provides the current position independently of the pre-installed positioning systems using the Dead reckoning technique [13].

After starting the application, the user uses the integrated camera to scan the QR code located on the particular floor. Based on the URL encoded in the QR code, the application will download an indoor vector map of the particular floor from the dedicated server along with the user's initial position on the map, corresponding to the position where the user captured the QR code. If the user moves, the application will draw its location as a continuous line on the downloaded floor plan, step-by-step. Using the data generated by the smartphone accelerometer, the system records the number of steps taken by the user. A step is detected as a pair of positive and negative values returned by the accelerometer. The current user orientation is determined by the digital compass. The initial orientation is determined when scanning the code, perpendicular to the floor plan. The whole system can be considered as less effective due to several factors. Length of the step is computed based on step acceleration force. Therefore, the end-user can with simulated movements force the system to count imaginery steps and eventually disrupt the computation. Also, occurring errors are cumulative and are increased with every next step of the end user [12].

2.4 Positioning Using Ultrasound or Radio Waves

This solution is based on the use of sound and radio waves to accurately determine the location of the user. As one of the practical examples can be stated is the system based on Wi-Fi signal. For the functionality of the system [14], beacons – static units installed on the ceilings – are required. The ultrasonic beacon periodically emits ultrasonic pulses and radio frequency messages with a unique identification code. By applying the Time-of-Arrival principle [15] on receiving information from another beacon and the speed of sound corrected for indoor air temperature, the receiver calculates its distance from the respective beacons. Since radio frequency messages propagate through space 10^6 times faster than ultrasound, the receiver calculates the distance of the receiver to the beacon based on the time elapsed between the start of the radio frequency message and the corresponding ultrasonic impulse. The receiver position can then be determined based on the coordinates of the beacons and the measured distances. Then, using trilateration or multilateration, it is possible to calculate the position of the smartphone in space, knowing the distances to several known beacons. However, using this system to track the end user can be considered as not suitable because the ultrasound is sensitive to temperature fluctuations and multipath signals bouncing.

2.5 Positioning Techniques Utilizing Magnetic Fields

Modern buildings containing steel and other ferromagnetic materials in their structures have unique, spatially dependent magnetic fingerprints that can be used for positioning purposes. Unique magnetic fields arise from the interaction of the

Earth's magnetic field with ferromagnetic materials. The non-constant surrounding magnetic fields produce different magnetic profiles, depending on the path taken by the user. One of the systems using this principle for positioning is IndoorAtlas. The application uses the IndoorAtlas API to communicate with the positioning service. The API sends the processed data of the smartphone sensors to the positioning service, which then calculates the current position and forwards it back to the applications via the API. This technology represents an innovative indoor positioning approach that can be used on its own or in collaboration with other technologies to improve accuracy. IndoorAtlas is a software positioning service that – in terms of hardware – requires only a smartphone equipped with built-in sensors to operate. In modern buildings, the accuracy of this technology ranges from 0.1 m to 2 m [6]. The service itself is based on the Microsoft Windows Azure Cloud platform. Before using the service, it is needed to generate a magnetic map of the indoor spaces, which are intended to be navigated through. Indoor Atlas has come with a complete solution including:

- IndoorAtlas Plans – web application designed to use for adding and managing individual floor plans,
- IndoorAtlas Map Creator – mobile app designed to measure magnetic fields and uploading measured values into the database,
- IndoorAtlas API – serves as a mediator for extracting the location.

3 Algorithms for Finding the Optimal Path

In navigation systems, it is necessary to determine the most optimal path from node A to node B passing through nodes X_0 …. X_n. Graph algorithms whose core is common are used for this. As the navigation system is to serve only in indoor conditions, algorithms that look for the shortest path in an unoriented edge-rated graph. Routing algorithms scan graphs from the starting node through neighboring nodes until they reach the destination [20].

3.1 Dijkstra's Algorithm

Dijkstra's algorithm stores all nodes in the priority queue sorted by distance from the source - in the first iteration, only the source has a distance of 0, all other nodes are infinite. In each step, the algorithm selects the highest priority node from the queue, which is the node with the lowest distance from the already processed part and places it among the processed nodes. It then goes through all of its unprocessed descendants, adds them to the queue if they are not already occupied, and verifies that they are no closer to the resources than they were before they were processed. The algorithm terminates when all nodes are

processed. The total asymptotic time complexity of Dijkstra's algorithm is O (n^2) [20].

3.2 Floyd-Warshall Algorithm

The Floyd-Warshall algorithm has a distance matrix at the input, let's call it D^0. If the edge of length l leads between two nodes (i, j), then this matrix contains exactly this value on the index (i, j). On the diagonal, this matrix has only zeros, and on other indices that do not correspond to an infinity edge. In other words, this matrix contains the distances of the nodes that do not pass through any intermediary. In each iteration of the Floyd-Washall algorithm, this matrix is recalculated to express the distance of all pairs of nodes through a gradually increasing set of potential intermediaries. Simply put, matrix D^1 will express the distance of all nodes with the possibility of using one (given) intermediary, D^2 distance with possible use of two (given) intermediate nodes, D_m with the possibility of using *m* intermediate nodes. Because the values from which the elements of the new matrix are calculated cannot be overwritten during the transformation, it is enough to use exactly one matrix for D^i and D^{i+1} in the implementation itself. The total asymptotic time complexity of Dijkstra's algorithm is O (n^2) [20].

3.3 Bellman-Ford Algorithm

The Bellman-Ford algorithm uses the edge relaxation method, which determines the currently set value of the shortest distance from node S. If the value at node is found to be higher than the value from the current node plus the edge rating from the current node to the node we would like to change its value, then the change (decrease) of this value is made. The main difference from Dijkstra's algorithm lies in the way passage chart. If all successors of one node using Dijkstra's algorithm are passed, then this node is closed and then the algorithm no longer modifies it. This does not happen in the Bellman-Ford algorithm, as it does not close these nodes immediately, but passes all nodes several times and gradually adjusts the values of the shortest path distances. The complexity of the algorithm is O ($V .E$), where V represents a number of nodes and E number represents of edges [20].

3.4 Conclusion

The dynamics of interior conditions can be considered relatively low. **The Bellman-Ford algorithm** makes it possible to find the shortest path in a graph that also contains negative edges, which is irrelevant for our system, as the distances between individual nodes should correspond to the real distance between the given geographical coordinates.

The Floyd-Warshall algorithm provides finding the shortest path from any starting node to any end node in a single run, which is redundant for our system and would be wasted on performance. Finding the shortest path from one given start node to a single end node is suitable for proposed system and therefore the use of **Dijkstra's algorithm** is the optimal solution for the proposed system.

4 Comparison of Indoor Position Technologies

Mobile phone camera localization is not the optimal way to obtain a location for a presented solution. The use of cameras would not guarantee the reliable operation of the proposed system in poor lighting conditions, or in buildings with large rooms, where the system would have difficulty identifying a sufficient number of recognition points.

To determine the position using **Philips Visual Light Communication technology**, it is necessary to install LED lights in every place in the interior where we want to obtain the position of the mobile phone. The use of this technology would ensure accuracy and reliability, but for the presented system, we need to find a solution that has the lowest possible implementation costs and does not require any additional installation of equipment. Therefore, the use of this technology is not again suitable for the presented system.

Another option lies in localization, which uses the **accelerometer and compass of the smartphone** to calculate the position of the device. It is not necessary to have additional hardware for the proper functioning of this technology, which can be considered asi a big advantege. However, calculating the distance from the initial position using an accelerometer to estimate the step length is a source of large error in determining the exact position. The user could also simulate walking with certain movements, which would lead to a malfunction of the system. This technology is inaccurate and therefore, it cannot be considered suitable for integration into the proposed system.

There are several limitations to calculate the **positions using ultrasound and radio waves (e.g.)**. The system is sensitive to temperature fluctuations and multi-way signal reflection. The operation of the system requires the installation of beacons that transmit ultrasound and radiofrequency messages. All these negatives make this technology unreliable and unusable for our system.

When using a system that would determine the user's position using bluetooth beacons, the installation of bluetooth beacons would be required for the system to work. To achieve good results, it would be necessary to install these lighthouses in the vicinity distances and so as to cover the whole area in which we want to locate the user. This technology is expensive and again unnecessarily complicated for the proposed system.

Use the unique magnetic field in the interior to determine the position of the mobile device is a technology whose installation costs are virtually zero. This technology is represented by **IndoorAtlas**. No installation of equipment is required to implement this solution. This technology is able to work in a wide variety of conditions. Only a smartphone equipped with sensors that are able to record the values of the magnetic field in individual parts of the mapped space is needed for operation. The used smartphone needs only Internet access to receive updates about the current location. The positioning accuracy of this system varies in the range of 0.1 meters to 2 meters. Due to the low implementation costs, sufficient accuracy, and efficiency, this technology is the optimal solution for a given problem.

Table 1 presented below compares the main features of previously stated technologies, which can be considered as essential for the further proposed system.

Table 1
Comparison of the selected technologies [11] [19] [21] [22]

	Bluetooth Beacons Positioning Technology	**Wi-Fi or Ultrasound Based Solution**	**IndoorAtlas Solution**	**Philips Visual Light Communication Solution**	**Egomotion Systems**
Location precision	2 m	5 m	0.1 m - 2 m	5 cm	5 cm – 1,5m
Maintenance	Average	Average	Easy	Easy	Average
Installation costs	Average / High	High	Low	Average / High	Varies
Signal change sensitivity	Sensitive	Sensitive	Sensitivity based mainly on electronic noise / fast moving metal objects (elevators)	Sensitive	Sensitive to light conditions and frequently changing environment

5 Proposed System Architecture

The most important element of the presented system is to divide the project itself into logical partitions, separating the retrieval of the indoor position using data from the IndoorAtlas API [6] and obtaining the smallest route using Dijkstra's algorithm [7]. The following figure shows the distribution of these logical parts of the project.

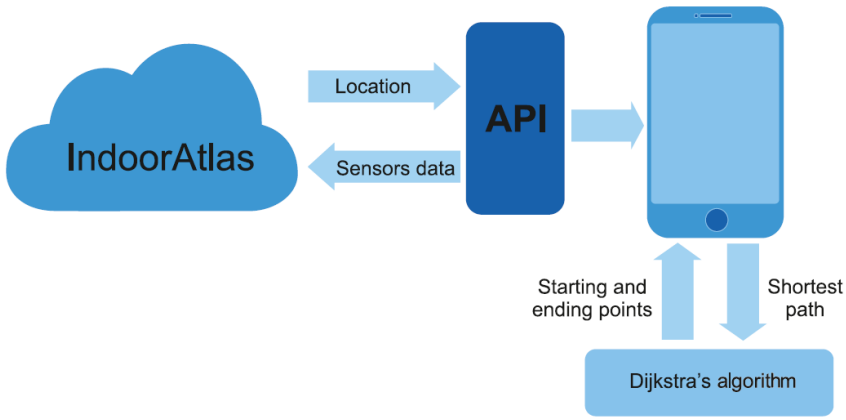

Figure 1
The proposed system architecture

The application operation principle is shown in Figure 2; this also depicts various situations that may arise when the user interacts with the application:

- a point inside the building is set as the starting point of the user's route,
- the current position is set as the starting position upon initiating navigation.

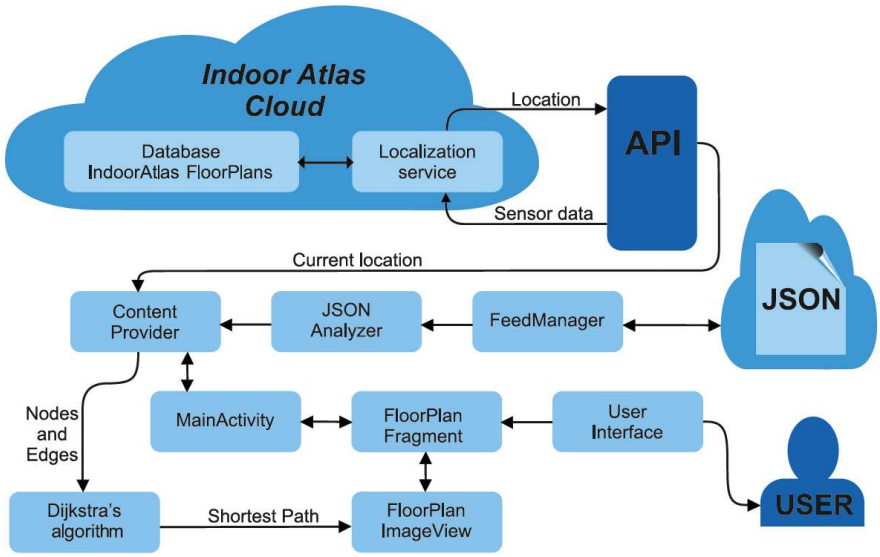

Figure 2
Basic principles of the proposed application

- In the first case, Dijkstra's algorithm determines the shortest distance between two points, while determining the user's position is not necessary because the algorithm uses only the vertices and edges of the processed graph as its input. The graph data can be accessed via an HTTP request, which returns a JSON object that is then analyzed by the analyzer, storing all necessary object references in memory. This method allows fast run-time access to files and data.
- In the second case, the IndoorAtlas API determines the current position as the starting position when the application starts. Again, Dijkstra's algorithm is being used, so a vertex with the latitude and longitude information of the user has to be added to the graph. In this case, we also need to know the floor where the user of our application is located.

6 Positioning with IndoorAtlas

The IndoorAtlas API provides positioning options using magnetic sensors of smart devices in several ways:

- a map of the particular building floor is added to the GPS coordinates,
- when collecting data during the calibration phase,
- when calculating the position itself.

[6] states that the source of the earth's magnetic field is highly conductive liquid iron rotating around the outer core of the Earth. The magnetic field generated by these magnetic currents is magnetic field *B*. The magnitude of magnetic field *B* is based on the surface area and can be described as a variable magnetic density.

The relationship between these is as follows:

$$1\frac{Wb}{m^2} = 1T = 10000Ga \tag{1}$$

The magnetic sensor of the smart device measures the variable magnetic density, and, based on this information, determines the direction of the cardinal direction: north. It is very important to note that the north of the magnetic field does not equal the geodetic north of Earth. Geodetic north points to the north pole that Earth rotates around, while magnetic north is the position of the geomagnetic field. This position is beyond the axis of the globe. The angle between the geodetic north and the magnetic north is the magnetic declination [16].

The magnetic declination keeps changing and varies depending on the position on the globe. The total intensity of the magnetic field F consists of the X (North), Y

(East), and Z (Down) components. The horizontal part H consists only of the components X and Y. Slope I describes the angle between H and F. Slope D is equal to the angle as shown in Figure 3.

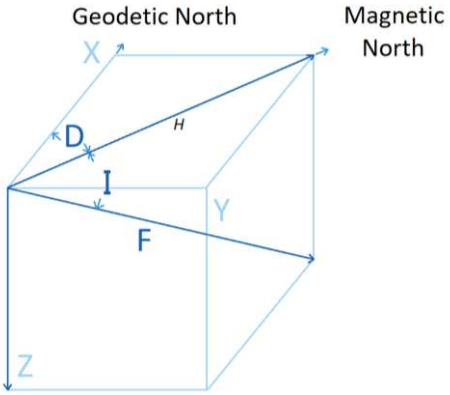

Figure 3
Parameters of the Earth's magnetic field

7 Optimal Path Calculation

To calculate the shortest distance between two points in real-time, Dijkstra's algorithm was used; the first point is the starting point of the positioning and the second point is the position the user wants to navigate to.

This algorithm is one of the basic algorithms in graph theory [7]. In the proposed system, the real world is mapped to a graph of vertices and edges on which Dijkstra's algorithm performs calculations. The application then communicates with the server using a JSON object, the date of which is then used to analyze the information stored in the content provider. The graph extracts the vertices and edges of the real world from the database.

7.1 Assignment of the Building Floor Plan to GPS Coordinates

The user position acquisition process begins by adding the building floor plan – in PNG or JPEG format – to IndoorAtlas Maps using the IndoorAtlas FloorPlans web application. This application allows easy assignment of building floor plans to the corresponding geographic coordinates, which allows the use of the geographic coordinate system in the application. To increase positioning accuracy, it is very important to set the length and width of the building to its actual dimensions, as IndoorAtlas actually calculates the distances relative to these

dimensions. IndoorAtlas Floor Plans allows adding a floor mask – in which black are the areas allowing device positioning, while walls and obstacles, where the device position cannot be determined, are drawn in white.

7.2 Position Calculation

For positioning, IndoorAtlas uses pattern matching – in this, it uses measured data to overcome the cumulative position estimation error. The pattern matching technique consists of two phases:

- an offline training phase,
- an online tracking and positioning phase.

During the offline training phase, a database of variable magnetic density measurements at specific points in the building is built. The data collected by the magnetic sensor are sent to the IndoorAtlas positioning service via the API; here, they are stored in the fingerprint database from which the fingerprint map is then created for the mapped building. In IndoorAtlas terminology, this fingerprint map is the IndoorAtlas FloorPlans system. The IndoorAtlas FloorPlans web service evaluates and provides information on the following:

- convergence distance – the distance to travel to accurately position the device,
- the positioning error indicating the possible distance from the current location,
- map coverage indicating the area that has been mapped and can be used for positioning the device.

Based on information from [6], during this phase, it is important to secure in several conditions:

- The device calibration is required during fingerprinting on a regular basis to ensure data quality (the calibration screen will pop up automatically when calibration is necessary).
- Set start point and end point to draw a path on the floor plan.
- Stand at the start point, tap the record button, and then start walking immediately towards the end point.
- Stop recording when you reach the end point.
- Walk at a steady pace (without changing the speed too much) and in a straight line following the path.
- Keep the phone directed straight ahead in front of the person performing the operation.
- Keep the device at least 50 cm away from the wall.

Figure 4 shows an example of the convergence distance in the mapped part of the building.

Figure 4
Convergence distance in the mapped part of the building

The data contained in the fingerprint database serve as reference points for the positioning phase. During the positioning phase, the current variable magnetic density, measured by the smartphone, is compared with all measurements stored in the fingerprint database. When the current data match the fingerprint in the database, it is highly probable that the user's position corresponds to the position where the fingerprint data were acquired from.

7.3 Graph Nodes

In the presented system, graph nodes will represent points on the respective floor of the building and the corresponding edges to create a logical map of the paths among the various points in the building. Each graph node (vertex) will have the following six parameters:

- an identifier, specifying a unique node,
- the node name,
- the node latitude,
- the node longitude,
- the floor of the node,
- a flag stating whether the node is a real position in the building or just a logical node needed for further calculations.

7.4 Graph Edges

In the presented system, graph edges represent a path from a node to another node. Each edge has the following four parameters:

- an identifier, specifying a unique edge,
- the starting node of the edge,
- the final node of edge,
- the distance between the nodes, calculated as the actual distance between the geographical coordinates.

7.5 Database of Geographical Graph Nodes

The IndoorAtlas service also provides a web service called FloorPlans that allows the acquisition of geographic graph nodes. Also, it is able to create so-called transition points – the system determines the latitude and longitude of these. It is important to perform this step with utmost accuracy, as the transition points also reflect the real-world situation. This method is an implementation of the haversine formula:

$$a = sin^2(\frac{\Delta\phi}{2}) + cos\phi_1 * cos\phi_2 * sin^2(\frac{\Delta\lambda}{2}) \tag{2}$$

$$c = 2 * \arctan 2(\sqrt{a}, \sqrt{(1-a)}) \tag{3}$$

$$d = R * c \tag{4}$$

where ϕ is the latitude, λ is the longitude and R is the ground radius in meters.

After calculating the distance between the current position and the compared node, the system verifies if the calculated distance is less than the smallest distance. If so, it is necessary to verify whether the edge connecting the node representing the current position and the compared node is valid. It may happen that the edge connecting the node closest to the current position and the node representing the current position pass through a wall. Such problems are solved programmatically by reading the downloaded IndoorAtlas FloorPlan plan as a bitmap. There, a path represents the edge connecting the compared node and the current position node is created. Later, the color of each pixel on the path is compared with the color used to highlight the walls. If the path does not contain wall color pixels, the edge is valid. If the previous condition is met, the shortest distance will be equal to the distance between the node of the current position and the currently compared node.

7.6 Results of the Propositioned Application Testing

Positioning accuracy was tested by two phases of measurements that were carried out in the premises of the selected building in Košice, Slovakia. The first phase of the measurements was conducted within one room (short distance measuring) and the second one was measured within the building (long-distance measuring).

The first phase: two points were selected in a room and were localized using the IndoorAtlas service. These points were selected so that one point could be reached from another only by an imaginary line (depicted in blue). Data from the IndoorAtlas API helped to determine the positions of the points between the two selected points. Then, the data were extracted and used to create the graphs of the positions achieved. The measurements were carried out in two different rooms. The accuracy of the first measurement is shown in Figure 5, while the accuracy of the second measurement is depicted in Figure 6.

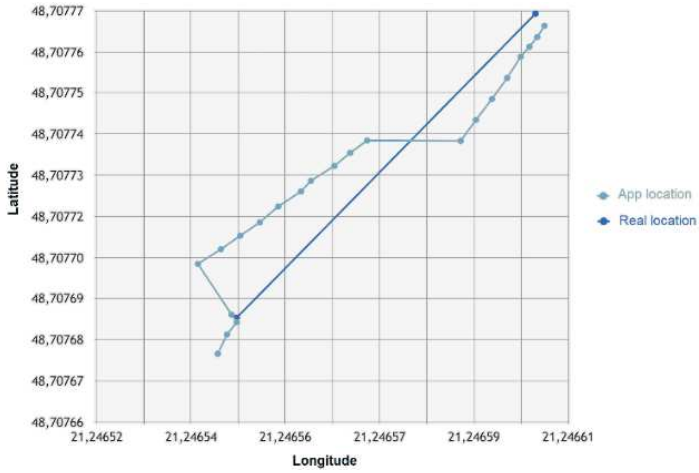

Figure 5
The first measurement of the phase one

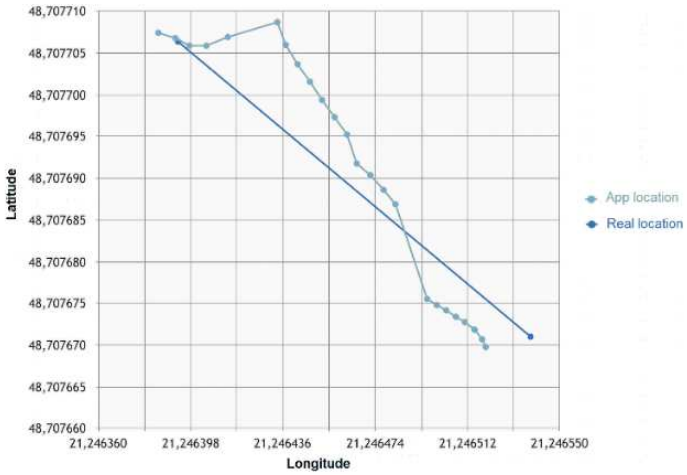

Figure 6
The second measurement of the phase one

Due to the small indoor distances, the curvature of the Earth need not be taken into account, so the measured distances may be mapped to the Cartesian coordinate system. Then, the distance of the individual points from the line representing the real trajectory of movement is calculated. The distance of the points from which it was not possible to construct a perpendicular to the particular segment of the actual trajectory is calculated as the distance of the particular point from the start point or end point of the direct trajectory. The distance of the points, from which it was possible to construct a perpendicular to a particular segment of the real trajectory is calculated using the distance of the particular point from the line, expressed as follows:

$$d = \frac{|A.M_x + B.M_y + C|}{\sqrt{A^2 + B^2}} \tag{5}$$

The linear equation was constructed using the start and end points of the straight path. The distance of the points from the line was expressed in degrees and therefore had to be converted to centimeters using the haversine formula.

In the first measurement of phase one, the average deviation from the actual travel path was 80.72 cm. In the second measurement of phase two, the deviation amounted to 58.24 cm. The total mean deviation of the two measurements of phase one was 69.48 cm. This deviation may be due to several factors:

- although during testing, the authors attempted to move between the two selected points as directly as possible with the smart device placed in an upright position, perpendicular to the chest, there is still a chance of inaccurate measurements due to imperfect straight forward movement,

- measurement deviations may also be affected by electromagnetic waves present by nearby electrical equipment;
- measurements were not performed using a device that IndoorAtlas recommends for positioning.

The second phase: the theory behind the second phase of the measurements is pretty much the same as phase one except the fact that the conducted experiments were held within the whole building across the various rooms. Each of the measurements in this phase brings similar results to phase one and exact trajectories are shown in Figure 7 and Figure 8.

In the first measurement of the phase two, the average deviation from the actual travel path was 75.15 cm. In the second measurement of the phase two, the deviation amounted to 81.63 cm. The total mean deviation of the two measurements of phase two was 78.39 cm. This deviation may be due to the same factors mentioned earlier.

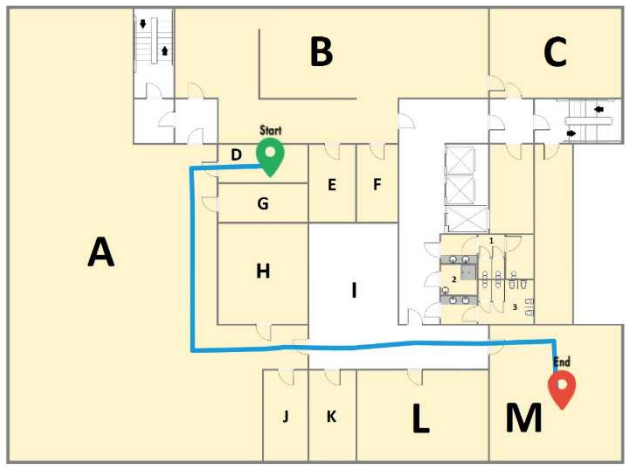

Real floor plan

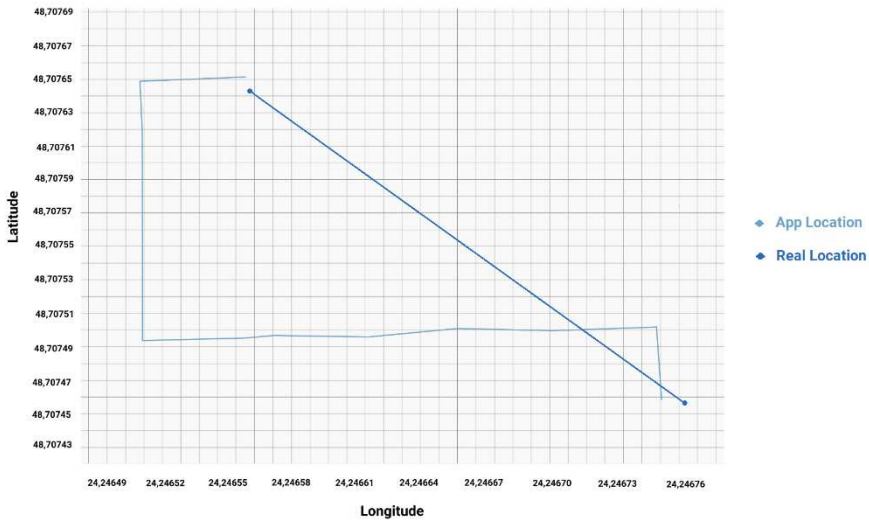

Figure 7
The first measurement of the phase two

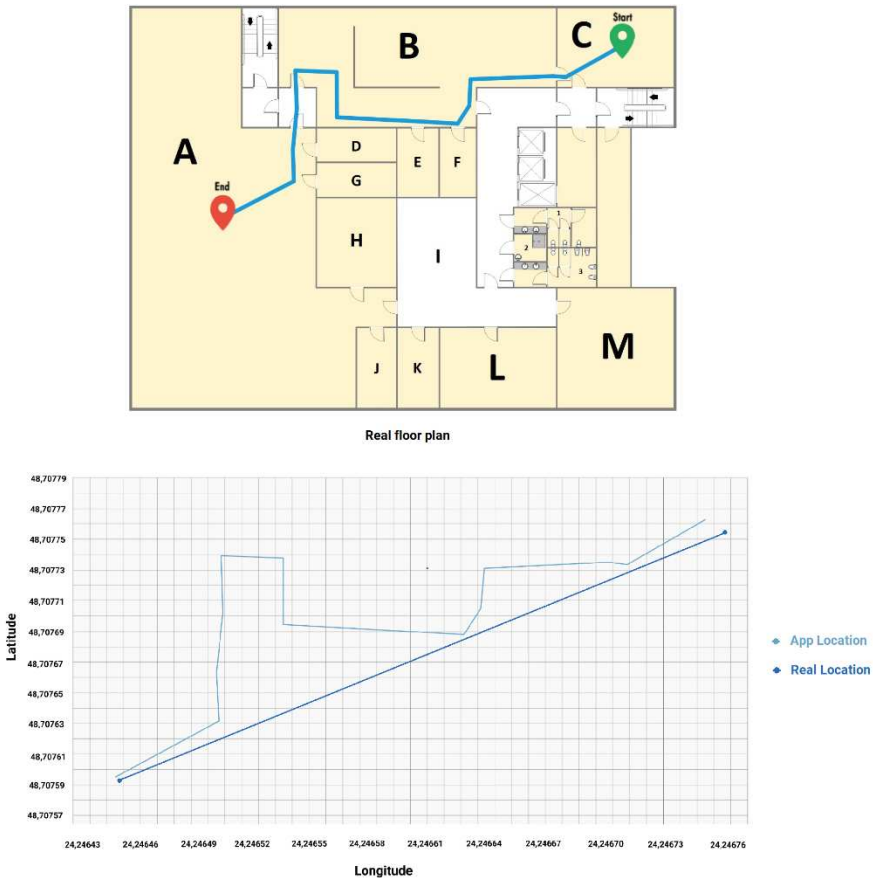

Figure 8
The second measurement of the phase two

8 Achieved Results

All the measurements were conducted within the selected building in Košice, Slovakia. During the process, there was a constant indoor ambient temperature of 23 °C. As mentioned in Section 4, Table 1, the producer of the IndoorAtlas library gives the accuracy of the library between 0.1 m to 2 m, which was successfully confirmed by our experiments. Table 2 below shows the complete results of the experimental part of the paper.

Table 2
Complete results of the measurements

Deviation	1. measurement	2. measurement	mean
Phase one	80.72 cm	58.24 cm	69.48 cm
Phase two	75.15 cm	81.63 cm	78.39 cm
All			73.935 cm

Conclusions

The presented article proposes an experimentally verified indoor navigation solution based on positioning using the Earth's magnetic field. Using the magnetic sensors present in mobile smart devices, the resulting program measures the properties of the surrounding magnetic field and then integrates it with the IndoorAtlas positioning service to determine the position of the device. The location is calculated by comparing the current data collected by the smart device sensor and the data stored in the IndoorAtlas database as Floor Plans. The shortest possible path is calculated using Dijkstra's algorithm. In the testing process of the proposed experimental solution, two phases of the measurements were performed with the results summarized in Section 8. The producer of the IndoorAtlas library gives the accuracy of 0.1 m to 2 m which was successfully confirmed by the conducted experiments. In future testing and fine-tuning, the following steps would be beneficial to the application, to allow the most precise positioning:

- Since measurements were made only using a single smart device type, future research could include measurements using several devices equipped with magnetic sensors. Later, it individual measurements could be compared to determine which smart device and/or magnetic sensor is more useful in this type of navigation.
- It would be useful to compare the performance and calibration of the magnetic sensors of smart devices and to select devices having the sensors with the highest sensitivity and also suitable for interaction with the IndoorAtlas service.
- Verification or elimination of the assumptions mentioned in section 5.6 regarding the possible impacts on measurement accuracy would be beneficial.
- It would be worth trying to implement solution mechanisms in conjunction with other algorithms designed to find the shortest path in the graph.
- It would also be appropriate to implement security mechanisms [17] [18].

Acknowledgement

This work was supported by the Faculty of Electrical Engineering and Informatics at the Technical University of Košice under contract No. FEI-2021-76: A modern interpreter of predicate linear logic formulas.

References

[1] M. P. Wylie, J. Holtzman, "The non-line of sight problem in mobile location estimation," in Proc. of 5th International Conference on Universal Personal Communications (ICUPC), MA, USA, 1996, pp. 827-831

[2] C. Hsieh, J. Chen and B. Nien, "Deep Learning-Based Indoor Localization Using Received Signal Strength and Channel State Information," in IEEE Access, Vol. 7, pp. 33256-33267, 2019

[3] N. Ádám, A. Baláž, E. Pietriková, E. Chovancová, and P. Feciľak, "The Impact of Data Representationson Hardware Based MLP Network Implementation," Acta Polytechnica Hungarica, Vol. 15, No. 2, pp. 69-88, 2018

[4] L. Vokorokos and N. Ádám, "Modeling of feedforward neural network in PAHRA architecture," in Proceedings of the 9th WSEAS International Conference on Simulation, Modelling and Optimization, Budapest, Hungary, 2009, pp. 446-451

[5] H. Falaki, et al, "Diversity in smartphone usage," in Proc. of the 8th International Conference on Mobile Systems, Applications, and Services, CA, USA, 2010, pp. 179-194

[6] IndoorAtlas, "Build seamless location-based experiences today," cited on 5th of May 2019, Available online: <https://www.indooratlas.com/>

[7] B. V. Cherkassky, A. V. Goldberg, T. Radzik, "Shortest paths algorithms: Theory and experimental evaluation," in: Mathematical programming, Vol. 73, No. 2, 1996, pp. 129-174

[8] R. F. Brena, J. P. García-Vázquez, C. E. Galván-Tejada, D. Muñoz-Rodriguez, C. Vargas-Rosales, and J. Fangmeyer, "Evolution of indoor positioning technologies: a survey," *Journal of Sensors*, Vol. 2017, Article ID 2630413, 21 pages, 2017

[9] H. Bay, T. Tuytelaars, and L. Van Gool, "SURF: Speeded Up Robust Features," in *Computer Vision – ECCV 2006*, Berlin, Heidelberg, 2006, pp. 404-417

[10] M. Afzalan and F. Jazizadeh, "Indoor Positioning Based on Visible Light Communication: A Performance-Based Survey of Real-World Prototypes," *ACM Comput. Surv.*, Vol. 52, No. 2, May 2019, doi: 10.1145/3299769

[11] M. Kaluža, K. Beg, B. Vukelić: Analysis of an indoor positioning systems *Zbornik Veleučilišta u Rijeci*, Vol. 5 (2017), No. 1, pp. 13-32

[12] S. Nishiguchi et al., “Reliability and validity of gait analysis by android-based smartphone,” Telemedicine and e-Health, Vol. 18, No. 4, pp. 292-296, 2012

[11] D. K. Son, E. Cho, I. Moon, Z. Ghassemlooy, S. Kim, and C. G. Lee, “Simultaneous transmission of audio and video signals using visible light communications,” *EURASIP Journal on Wireless Communications and Networking*, Vol. 2013, No. 1, p. 250, Oct. 2013, doi: 10.1186/1687-1499-2013-250

[12] Z. Yang, C. Wu, Z. Zhou, X. Zhang, X. Wang, and Y. Liu, “Mobility Increases Localizability: A Survey on Wireless Indoor Localization Using Inertial Sensors,” *ACM Comput. Surv.*, Vol. 47, No. 3, Apr. 2015, doi: 10.1145/2676430

[13] H. Rashid and A. K. Turuk, "Dead reckoning localisation technique for mobile wireless sensor networks," in *IET Wireless Sensor Systems*, Vol. 5, No. 2, pp. 87-96, 4 2015

[14] J. Qi and G.-P. Liu, “A Robust High-Accuracy Ultrasound Indoor Positioning System Based on a Wireless Sensor Network,” *Sensors (Basel)*, Vol. 17, No. 11, p. 2554, Nov. 2017, doi: 10.3390/s17112554

[15] C. Gentner and T. Jost, "Indoor positioning using time difference of arrival between multipath components," *International Conference on Indoor Positioning and Indoor Navigation*, Montbeliard-Belfort, 2013, pp. 1-10

[16] S. Zhang, et al, “Magnetic declination and zonal wind effects on longitudinal differences of ionospheric electron density at midlatitudes,” in Journal of Geophysical Research, Vol. 117, No. A8, USA, 2012, pp. A08329

[17] E. Chovancová *et al.*, “Securing distributed computer systems using an advanced sophisticated hybrid honeypot technology,” *Computing and Informatics*, Vol. 36, No. 1, pp. 113-139, 2017

[18] S. Kim, S. Ha, A. Saad and J. Kim, "Indoor positioning system techniques and security," 2015 Forth International Conference on e-Technologies and Networks for Development (ICeND), Lodz, 2015, pp. 1-4

[19] M. Kaluža and B. Vukelic, “Analysis of an indoor positioning systems,” *Zbornik Veleučilišta u Rijeci*, Vol. 5, pp. 13-32, 2017, doi: 10.31784/zvr.5.1.2

[20] Boris V Cherkassky, Andrew V Goldberg a Tomasz Radzik. „Shortest paths algorithms: Theory and experimental evaluation”. In: Mathematical programming 73.2 (1996), s. 129-174

[21] A. Yassin *et al.*, "Recent Advances in Indoor Localization: A Survey on Theoretical Approaches and Applications," in *IEEE Communications*

Surveys & Tutorials, Vol. 19, No. 2, pp. 1327-1346, Secondquarter 2017, doi: 10.1109/COMST.2016.2632427

[22] F. Zafari, A. Gkelias and K. K. Leung, "A Survey of Indoor Localization Systems and Technologies," in *IEEE Communications Surveys & Tutorials*, Vol. 21, No. 3, pp. 2568-2599, thirdquarter 2019, doi: 10.1109/COMST.2019.2911558

Fuzzy Failure Modes and Effects Analysis Using Summative Defuzzification Methods

László Pokorádi[1], Sinan Koçak[2], Edit Tóth-Laufer[1]

[1]Óbuda University, Institute of Mechatronics and Vehicle Engineering
Népszínház u. 8, 1081 Budapest, Hungary
pokoradi.laszlo@bgk.uni-obuda.hu; laufer.edit@bgk.uni-obuda.hu

[2]Óbuda University, Doctoral School on Safety and Security Sciences Budapest, Hungary; sinan.kocak@bgk.uni-obuda.hu

Abstract: Nowadays, in order to achieve competitiveness in the manufacturing industry, quality and reliability in design and manufacturing processes are essential factors. These requirements can only be fulfilled by using effective estimation models, instead of the cost- and time-consuming measurements. The widely used engineering technique Fuzzy-based Failure Modes and Effects Analysis (F-FMEA) also serves this purpose. This method is able to identify and eliminate potential problems of a product from the process, system, design, and service based on the available data to avoid possible risk (i.e. repetition of damage and additional costs). Data can be analyzed properly assessing the Probability of Failure (PoF), Consequence of Failure (CoF), and Detectability of Failure (DoF) using a fuzzy-based model, which can work well in situations where there is not enough data for a statistical model. Authors investigate different defuzzification methods in F-FMEA, and propose a novel Summative defuzzification to combine the results of the different fuzzy subsystems.

Keywords: Fuzzy logic; FMEA; Defuzzification; Summative Defuzzification

1 Introduction

Nowadays, due to increased quality requirements, it has become vital to optimize the manufacturing process. Technological advances make it possible to improve the quality and reliability of the manufactured workpiece and the process itself. However, measuring all possible settings and parameters, which affect the quality requirements is cost- and time-consuming, and in some cases is not possible at all. Several problem-solving techniques are available to handle this issue, such as Lean Manufacturing, Six Sigma, Statistical Engineering, Lean Six Sigma [2]. The widely used engineering technique Failure Modes and Effects Analysis (FMEA) also serves this purpose [1]. It is a systematic quality improvement method aimed at preventing any possible defects, which may occur in the system,

design, process, or services. This approach was first used in 1949 by the United States Military to reduce variation sources and possible failures associated with ammunition production, therefore, has proven to be highly effective [3]. This was followed by FMEA and was developed by NASA at the end of the 1960s to be used in the aerospace industry [4]. This technique has been advanced and popularly adopted until today and used in the aerospace sector, the automobile industry, the chemical industry, and in all technology-weighted areas.

Since risk has been defined as the severity and probability of a given hazard, risk prediction is usually based on a quantitative assessment of the risk level and likelihood of occurrence [5]. However, both quantitative and qualitative parameters can be observed among the risk factors, which should be handled adequately in order to obtain realistic results. Consequently, only that method should be used which can handle both types of inputs during the evaluation. The fuzzy approach fulfills these requirements; thus it is a useful method in risk management that solves the uncertainty and subjectivity of the data and the evaluation process [6]. It is a mathematical approach with a decision-making mechanism without sharp limits, in this way it mimics human logic. The concept of fuzzy logic and related fuzzy set theory was introduced and published in 1965 by Lotfi A. Zadeh to handle mathematical concepts that are difficult to quantify [7]. In the classical set concept, an element is either a member of a set or not. However, in fuzzy logic, the degree of specified membership ranges is accepted between 0 and 1 [8]. This approach serves as a more realistic solution to daily life problems because it has a more flexible structure. In 1975, the fuzzy logic inference was operated by Mamdani and Assilian as the first effort to control the steam engine and boiler combination [9]. In light of these studies, fuzzy logic has become a popular and widely-used technique in many areas, such as industrial, aerospace, electrical, mechanical, mechatronics, computer, chemical, biomedical, environmental, agricultural, geological, etc. [20].

The Fuzzy Failure Modes and Effect Analysis (F-FMEA) integration approach is an extension of the traditional FMEA method and has been used since the mid-1990s. The first Fuzzy logic-based Failure Mode, Effects, and Criticality Analysis is connected to the names of Bowles and Peláez, which was used to first describe the prioritization of failures regarding to the corrective actions [10]. The authors proposed two different, but related approaches for assessing criticality. The first one to operate with numerical rankings, based on the aggregated opinions of the experts or obtained from a reliability analysis, and use crisp values. It is applied in the traditional risk priority number (RPN) calculation. However, in the design process, qualitative factors should also be considered, where less detailed information is available. Consequently, the second approach allows these kinds of fuzzy inputs, and linguistic terms can be assigned to the RPN calculation as ranking.

In current literature, there are numerous case studies in the field of F-FMEA. The recent studies of Jakkula, Mandela, and Chivikula's publications are valuable

additions aimed at the FMEA risk assessment approach for the Load Haul Dumper (LHD) machine [11]. The authors analyzed the LHD's failure behavior in every potential failure mode that provided information on various aspects, such as the current operating state of the machines, the reasons for the failure modes occurring, the effect of the failure modes on the equipment performance, and reliable life, etc. Moreover, these investigations evaluated estimates of required management practices or control measures such as possible design changes and replacement of components to ensure the necessary level of usability and utilization.

Further, Kelvin, Jason, Chee-Wah, and Alan have studied the new product development in the flexible electronics industry using the application of Fuzzy-based FMEA [12]. The goal of the paper was to minimize the risks of developing new products for high-tech enterprises in a short time. Therefore, the authors developed a unique methodology to make the product reliable for a long time by prioritizing critical failure mode using F-FMEA.

The bearing is an ubiquitous, essential part of the machine-building industry, used to move and rotate all kinds of machines. The fatigue of the bearing depends on the ambient conditions, the load, and the mechanical strength of the parts that make up the bearing [1] [14] [15] [16].

This paper aims to develop novel fuzzy rule-based risk assessment methods using summative defuzzification in F-FMEA model. Three criteria are calculated to define the Risk Priority Number (*RPN*); the Probability of Failure (*PoF*), the Consequence of Failure (*CoF*), and the Detectability of Failure (*DoF*). This can be achieved by comparing the result of the traditional defuzzification methods, and the authors propose a novel summative defuzzification to combine the results of the different fuzzy subsystems.

The paper is structured as follows: Section 2 presents the FMEA methods. In Section 3 the proposed novel Summative defuzzification methods are presented. Section 4 illustrates the use of proposed methods for risk assessment of bearing manufacturing process as a case study. Section 5 is devoted to the conclusion.

2 The Failure Mode and Effect Analysis

The Failure Modes and Effects Analysis (FMEA) is one of the well-known reliability analysis methods. The FMEA was developed in the USA; Martin Marietta and Boeing companies published an engineering manual on the general method back in 1957. The FMEA method was successfully employed quite early within the frame of the Apollo Moon landing program after astronauts Grissom, White and Chaffee had died on board Apollo 1 during a ground test.

2.1 The Original (crisp) FMEA

The IEC Standard Publication 812 [4] documented how to carry out the "original" FMEA. During the analysis, experts investigate process or system, determine its potential failures and their efficient causes. Criticality level (RPN_i) of the determined i^{th} cause is assessed depending on Probability of Failure (PoF_i), Consequence of Failure (CoF_i), and Detectability of Failure (DoF_i), based on the following multiplication

$$RPN_i = CoF_i.PoF_i.DoF_i \tag{1}$$

Using the results and ranking of *RPN*s, experts propose actions to improve the reliability of the investigated system or process. From time to time, additional requirements can be applied. For example, (see Table 3 and Table 4):

"If $CoF_i > 5$, then Action is Needful".

if there is not enough data available to experts for statistical modeling, for "crisp" FMEA, estimated parameters should be used. Different linguistic interpretations may result in some inaccuracy, which should be handled by the experts. One of the possible tools for this purpose is the Fuzzy Rule-based FMEA (F-FMEA). The F-FMEA seems to be a powerful mathematical approach, which is capable of combining linguistic and numeric variables in order to estimate the subjectiveness involved in FMEA.

2.2 Traditional Fuzzy Rule Based F-FMEA

The traditional fuzzy decision process consists of the following sub-processes: fuzzification, inference (firing strength calculation, and implication), composition, and defuzzification (Figure 1). In certain cases the composition and defuzzification processes are combined.

In the fuzzification sub-process, crisp input values are converted into membership values to define the extent to which the value belongs to the fuzzy sets, which are described using linguistic variables. The predefined fuzzy membership functions for the input parameters represent the mean of experts opinion. These fuzzified values are used in further computations.

The inference sub-process consists of the firing strength calculation and implication. The firing strength calculation is used to combine the membership values of the different input parameters using a conjunction, or disjunction operator. The result of this step represents the truth-value of the rule antecedent for each rule. After evaluating the condition part of the rule, the consequence of the same rule should be considered, using a conjunction operator in the implication step. In this step, the extent of the given rule consequence is involved in the output is examined.

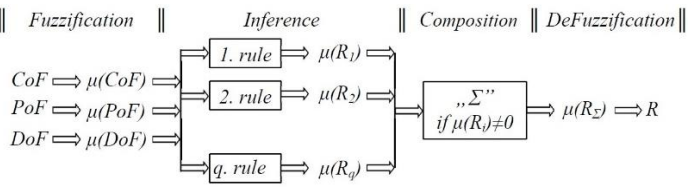

Figure 1
Traditional fuzzy process flow-chart (source: [17])

The above steps are performed for all the rules. In the composition sub-process, the obtained fuzzy sets (i.e. rule consequence after the inference) are aggregated that occur in the fuzzy rule base. This sub-process results in a single, but complex set. It combines the result of the inference of each rule and determines the output of the system.

The last sub-process is defuzzification, which is used to generate a crisp value to represent the output fuzzy set in the best possible way.

2.3 F-FMEA with Summative Defuzzification

The above-mentioned traditional methods can be used effectively when the analysis is performed based on the opinion of a single expert. However, the analysis becomes more reliable if it is considered with multiple opinions if they are available. This type of analysis requires a modified method to obtain a more pronounced result. To address this issue authors, a novel method, so-called Summative defuzzification (SDF) is proposed. This technique calculates the average of the different defuzzified crisp values obtained from different experiences by applying the determined defuzzification method again.

In all cases, the results are considered up to the composition sub-processing of the fuzzy inference process described in Section 2.2. Figure 2 shows the inference process of the SDF fuzzy model for the case where the analysis is performed based on two opinions.

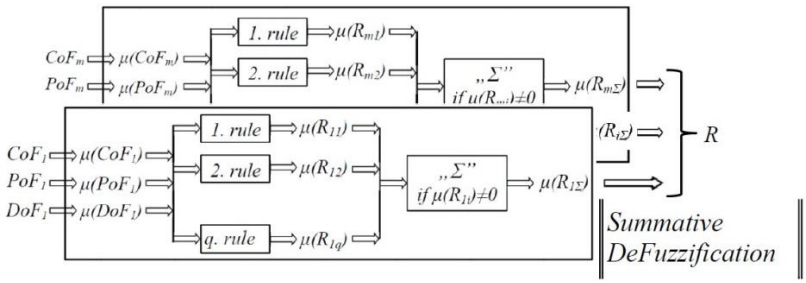

Figure 2
Flow cart of Fuzzy inference with summative defuzzification (source: [21])

3 Summative Defuzzification Methods

Defuzzification is the final sub-process, which transforms the fuzzy set to a crisp value of criticality. This value will be obtained in such a way as to best represent the aggregated fuzzy set. As a result of the fuzzy inference mechanism, the defuzzified crisp value shows the action to be considered in process control. As for which method is the most appropriate, that can always be determined by the task. In this section, the two most commonly used traditional defuzzification methods are presented. These methods are applied in the proposed novel approach.

3.1 Traditional Defuzzification Methods

First a short overview is given about traditional fuzzy rule based F-FMEA, followed by the introduction of summative defuzzification.

3.1.1 Center of Gravity (CoG) Method

The Center of Gravity (*CoG*) method is one of the most frequently used defuzzification methods. It defines the center of gravity under the curve, considering overlapping areas more times.

The following equation defines the crisp result of the centroid defuzzification method.

$$R_{CoG} = \frac{\sum_{i=1}^{n} \int_{-\infty}^{\infty} \mu_i(z) z dz}{\sum_{i=1}^{n} \int_{-\infty}^{\infty} \mu_i(z) dz} \quad , \tag{2}$$

where n is the number of sub-conclusions, μ_i is truth value of the i^{th} sub-conclusion.

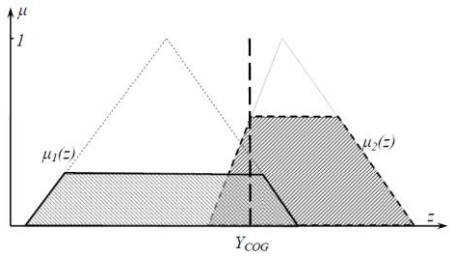

Figure 3
Centre of Gravity Defuzzification Method (source: [22])

3.1.2 Center of Area (CoA) Method

The CoA method is similar to the Center of Gravity method. The difference between the two methods is that the center of gravity method takes into account the overlapped areas of sub-conclusions multiple times, whereas the center of area method only takes into account them only once (see Figs. 3 and 4). The major disadvantage of CoA, as compared with the Center of Gravity method, is that it is very difficult to calculate it in the case of complex shape partial conclusions [18].

$$R_{CoA} = \frac{\int_{-\infty}^{\infty} \mu_{\Sigma}(z) z dz}{\int_{-\infty}^{\infty} \mu_{\Sigma}(z) dz}, \tag{3}$$

where μ_{Σ} is the maximum height of the conjunct set of sub-conclusions.

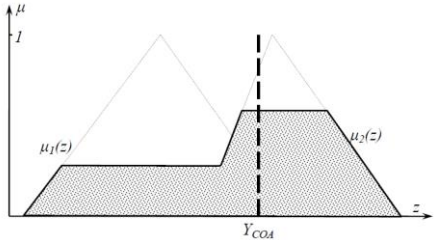

Figure 4
Centre of Area Defuzzification Method (source: [22])

3.2 Summative Defuzzification Methods

In the F-FMEA model it is vital to take into account the available multiple opinions because it makes the analysis more reliable. However, in the case when more different observations are available, the traditional inference process should be modified. This sub-section introduces the theoretical basics of the proposed novel method.

3.2.1 Summative Center of Gravity Defuzzification (SCoG)

In this method, the aggregated fuzzy set representing the expert opinion should first be determined considering overlapping areas more times (as is the case of the COG method). Then, in order to combine the resulting sets of the different experts to gain the system output based on the summary opinion, the CoG method is used on the fuzzy sets obtained for different opinions.

The crisp value of summative Centroid defuzzification method (R_{SCoG}) is defined by the equation

$$R_{SCoG} = \frac{\sum_{j=1}^{m}\sum_{i=1}^{n}\int_{-\infty}^{\infty}\mu_{ji}(z)zdz}{\sum_{j=1}^{m}\sum_{i=1}^{n}\int_{-\infty}^{\infty}\mu_{ji}(z)dz}, \tag{4}$$

where m is the number of the different expert groups, n is the number of sub-conclusions, μ_{ji} is the truth value of the i^{th} sub-conclusion in the case of the j^{th} expert opinion. Figure 5 illustrates the sub-conclusions to be considered separately because the CoG method defines the center of gravity under the curve, considering overlapping areas more times. The overall output set of the system can be generated as a composition of Opinion 1 and Opinion 2.

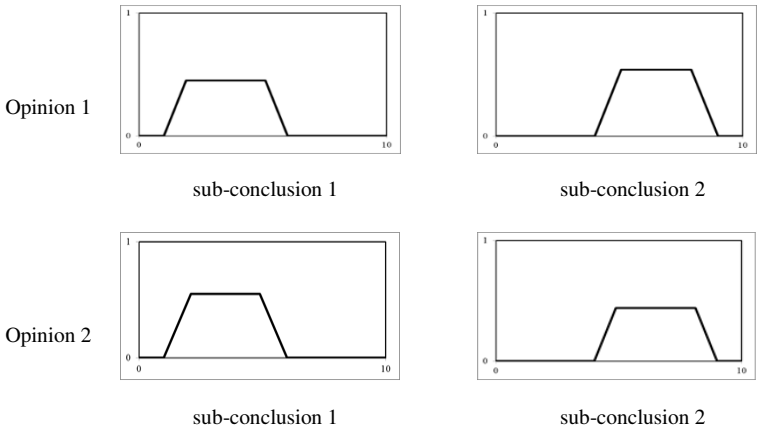

Figure 5
Sub-conclusions of the Failure 'A1' in the Case Study

3.2.2 Combined CoA and CoG Summative Defuzzification (SCoAG)

This version of the Summative defuzzification is a combination of the traditional CoA and CoG methods.

First, the aggregated fuzzy set representing the expert opinion should first be determined considering overlapping areas only ones (as is the case of the COA method) to determine the conclusion sets of different opinions. Then, the obtained fuzzy sets should be combined using the Center of Gravity method.

$$R_{SCoAG} = \frac{\sum_{j=1}^{m}\int_{-\infty}^{\infty}\mu_{\Sigma}(z)zdz}{\sum_{j=1}^{m}\int_{-\infty}^{\infty}\mu_{\Sigma}(z)dz} \tag{5}$$

where *m* is the number of the different expert groups.

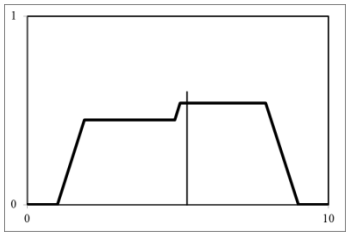

area of the opinion 1

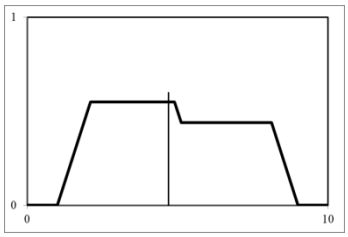

area of the opinion 2

Figure 6
Areas of the Opinions of the Failure 'A1' in the Case Study

4 Case Study

As a case study, the authors investigated an F-FMEA system for assessing the risk of the bearing manufacturing process to demonstrate the usage of summative defuzzification, and the results are compared to the results of publication [1]. For comparability, the same inputs are considered in the modified system, which were used in publication [1]. Although the original system analyzed the opinions of two different expert groups on average, the Summative-defuzzification-supported F-FMEA inference took the opinions into account separately. The failure codes are listed in Table 1, and the related inputs are shown in Table 2, including both individual and average opinions of Team 1 and Team 2. During the evaluation, trapezoidal fuzzy membership functions are used, which are defined by Figure 7, and Equation (6).

Table 1
Failure codes

Function	Failure mode	Failure effect	Code	Occasion (occurance)
Outer diameter of bearing	Big	installation problem, short fatigue life	B1	adjusting of a machine
			B2	omission of finishing
	Small	slack-running fit, early failure	A1	breakage of cone belt
			A2	improper emulsion concentration
			A3	Continuity of charging is improper
			A4	Congestion before finishing

Table 2
Input Data of FMEAs

	Opinion	B1	B2	A1	A2	A3
CoF	Team 1	4.00	4.00	4.00	4.00	4.00
PoF		3.10	9.00	2.10	3.20	2.70
DoF		2.00	2.00	1.00	1.90	2.00
CoF	Team 2	3.66	3.66	3.33	3.33	3.33
PoF		2.50	9.00	1.90	2.80	3.30
DoF		2.33	2.00	1.66	1.76	2.66
CoF	Average	3.83	3.83	3.67	3.67	3.67
PoF		2.8	9.00	3.00	3.00	2.66
DoF		2.17	2.00	1.33	1.83	2.33

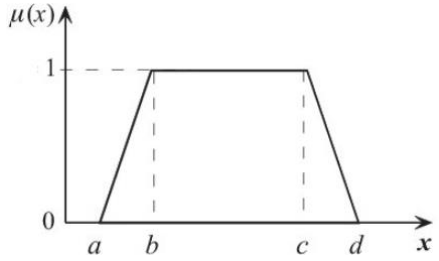

Figure 7
Trapezoidal fuzzy membership function

$$\mu_{A_i}(x) = \begin{cases} 0 & if \quad x \le a_i \\ \dfrac{x - a_i}{b_i - a_i} & if \quad a_i \le x \le b_i \\ 1 & if \quad b_i \le x \le c_i \\ \dfrac{d_i - x}{d_i - c_i} & if \quad c_i \le x \le d_i \\ 0 & if \quad d_i \le x \end{cases} \tag{6}$$

where a_i, b_i, c_i, d_i are the membership function parameters, and $a_i \neq b_i$, $c_i \neq d_i$.

The proposed F-FMEA method uses both qualitative and quantitative perspectives of three inputs and one output parameter, classified as Probability of Failure (*PoF*), Consequence of Failure (*CoF*), and Detectability of Failure (*DoF*) and Risk Priority Number (*RPN*). The fuzzy membership function parameters are specified in Table 3, and illustrated in Figures 8-11.

Table 3
Membership Functions

CoF	C1	Low	$\mu_{Low} = f$: (0,0,1,3)
	C2	Medium	$\mu_{Med} = f$: (1,3,4,6)
	C3	High	$\mu_{H} = f$: (4,6,10,10)
PoF	O1	Improbable	$\mu_{Imp} = f$: (0,0,1,3)
	O2	Occasional	$\mu_{Occ} = f$: (1,3,4,6)
	O3	Probable	$\mu_{Pro} = f$: (4,6,10,10)
DoF	D1	Detectable Easily	$\mu_{E} = f$: (0,0,1,3)
	D2	Detectable	$\mu_{Det} = f$: (1,3,4,6)
	D3	Detectable with Difficulty	$\mu_{Dif} = f$: (4,6,10,10)
PRN	R1	Action is Unnecessary	$\mu_{Unn} = f$: (0,0,1,3)
	R2	Action is Suggested	$\mu_{Sug} = f$: (1,3,4,6)
	R3	Action is Needful	$\mu_{N} = f$: (4,6,7,9)
	R4	Action is Very Needful	$\mu_{VN} = f$: (7,9,10,10)

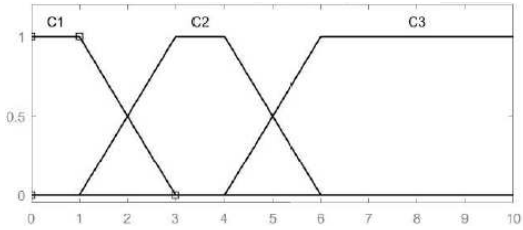

Figure 8
Input variable "CoF

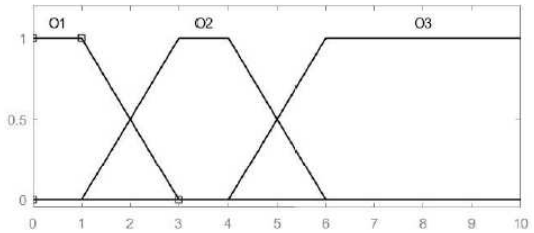

Figure 9
Input variable "PoF"

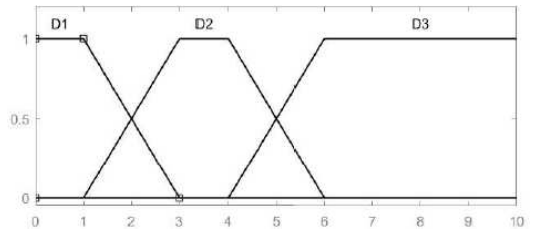

Figure 10
Input variable "DoF"

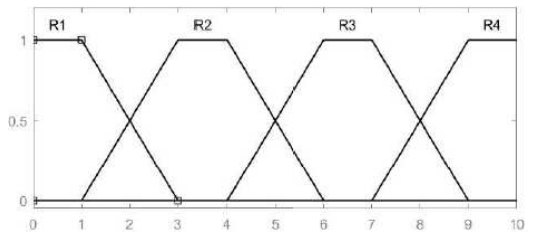

Figure 11
Output variable "Risk Priory Number"

In Table 4, the rule-base of the Fuzzy-based FMEA is defined in an IF-THEN structure, and the Zadeh-norms are used, i.e. minimum operator as AND connection, and the maximum operator as OR connection. Accordingly, following the composition sub-process, the *RPN* is calculated using defuzzification methods for each event.

Table 4
The Rule Base of FMEAs

IF C1 *AND* O1 *AND* D1 THEN R1
IF C1 *AND* O2 *AND* D1 THEN R2
IF C1 *AND* O1 *AND* D2 THEN R2
IF C1 *AND* O2 *AND* D2 THEN R3
IF C2 *AND* O1 *AND* D1 THEN R2

IF C2 *AND* O2 *AND* D1 THEN R3
IF C2 *AND* O1 *AND* D2 THEN R3
IF C2 *AND* O2 *AND* D2 THEN R3
IF C3 *OR* O3 *OR* D3 THEN R4

Table 4 demonstrates the results of the original and modified systems. The results of the original system, where the evaluations are based on the average of expert opinions, are shown in the CoG and CoA columns referring to both F-RPN and Relative FRPN values. The columns SCoG and SCoAG show the result of the proposed F-FMEA improving by the summative defuzzification method when the opinions of the expert groups are evaluated separately, and then summarized.

Table 5
Result of comparison with the results of publication [1]

Failure	F-RPN				Relative FRPN [%]			
	CoG	CoA	SCoG	SCoAG	CoG	CoA	SCoG	SCoAG
B1	6.04	6.2	5.892	6.111	18.443	18.96	18.327	18.64
B2	8.94	9.00	8.94	9.00	27.298	27.52	27.807	27.46
A1	4.77	4.5	4.995	4.967	14.565	13.76	15.537	15.15
A2	6.5	6.5	6.21	6.386	19.847	19.88	19.316	19.48
A3	6.5	6.5	6.113	6.312	19.847	19.88	19.014	19.26

Based on the case study result, the following conclusions can be drawn:

- failure B2 has the highest F-RPN and Relative FRpN numbers;
- failure A1 has the smallest F-RPN and Relative FRpN numbers;
- all the defuzzification methods generate close relative RPN [%] value for B1, A2, and A3.
- the F-FMEA with summative defuzzification gives more expressive results according to the experts. This can be seen from the results that for A2 and A3, the traditional methods give the same results for both RPN and Relative RPN, whereas the summation methods differentiate them better.
- it can be observed that for B2, both CoG and SCoAG give the same result, just like for CoA and SCoAG. This situation arises because this failure is evaluated equally by the two expert groups.

Conclusion

Nowadays, due to increased quality requirements, optimizing the manufacturing process has become crucial. However, measuring all possible settings and parameters, which affect the quality requirements is both cost- and time-consuming, and in some cases is not possible at all. The widely used engineering technique Failure Modes and Effects Analysis (FMEA) is an excellent tool for

preventing any possible defects, which may occur in the system, design, process, or service. However, the applicability of the method is limited by the fact that both quantitative and qualitative parameters can be observed among the risk factors, which should be handled adequately in order to obtain a realistic result. The Fuzzy-FMEA is an extension of the traditional FMEA method, which is able to handle the above-mentioned problem.

The F-FMEA can be used effectively when the analysis is conducted based on the opinion of a single expert. However, if multiple opinions of different experts are available a modified method is needed to ensure more reliable analysis. As an answer to this problem, the authors of this paper propose a novel F-FMEA method using Summative defuzzification (SCog and SCoAG). In this case, the opinions of the different experts are evaluated separately, and the overall result is composed based on the obtained results using a defuzzification again.

After presenting the theoretical basics, a case study was investigated in an F-FMEA system for assessing the risk of the bearing manufacturing process to demonstrate the usage of summative defuzzification, and the results were compared to the results of the traditional F-FMEA method. Based on the investigation it can be concluded that F-FMEA with summative defuzzification gives more expressive results according to the experts.

In future scientific research, the authors intend to:

- study the usage possibilities of fuzzy rule-based methods in the technical management decision making such as risk assessment;
- develop novel fuzzy rule-based methods using summative defuzzificaton in risk assessment-related fields.

References

[1] S. Koçak, E. Toth-Laufer and L. Pokorádi, "Fuzzy Failure Modes and Effects Analysis with Different Defuzzification Methods – A Case Study for Bearing Manufacturing Process," in *IEEE 17th International Symposium on Intelligent Systems and Informatics*, Subotica, Serbia, 2019

[2] Gy. Czifra, P. Szabó, M. MÍkva, J. Vaňová, "Lean Principles Application in the Automotive Industry," Acta Polytechnica Hungarica, Vol. 16, No. 5, pp. 43-62, 2019

[3] T. A. Carbone and D. D. Tippett, "Project risk management using the project risk FMEA," *Engineering management journal,* Vol. 16, No. 4, pp. 28-35, 2004

[4] R. D. Reid, "FMEA—something old, something new," *Quality Progress,* Vol. 38, No. 5, pp. 90-93, 2005

[5] G. Popov, B. K. Lyon and B. Hollcroft, {Risk assessment: A practical guide to assessing operational risks, John Wiley & Sons, 2016

[6] E. Tóth-Laufer, M. Takács and I. J. Rudas, "Fuzzy logic-based risk assessment framework to evaluate physiological parameters," *Acta Polytechnica Hungarica,* Vol. 12, pp. 159-1782, 2015

[7] L. A. Zadeh, "Fuzzy sets," *Information and control,* Vol. 8, No. 3, pp. 338-353, 1965

[8] S. Koçak, "Fuzzy Logic and its Mechatronics Engineering," *Repüléstudományi közlemények xxix. élfolyam,* pp. 41-48, 2017

[9] E. H. Mamdani and S. Assilian, "Learning control algorithms in real dynamic systems," in *th IFAC/IFIP International conference on digital computer applications to process control*, Springer, 1974, pp. 13-74

[10] J. B. Bowles and C. E. Peláez, "Fuzzy logic prioritization of failures in a system failure mode, effects and criticality analysis," *Reliability Engineering & System Safety,* Vol. 50, No. 2, pp. 203-213, 1995

[11] J. Balaraju, M. G. Raj and C. S. Murthy, "Fuzzy-FMEA risk evaluation approach for LHD machine-A case study," *Journal of Sustainable Mining,* Vol. 4, No. 18, pp. 257-268, 2019

[12] Kelvin P. L. Pun, Jason Rotanson, Cheung Chee-wah, Alan H.S., Chan, "Application of fuzzy integrated FMEA with product lifetime consideration for new product development in flexible electronics industry," *Journal of Industrial Engineering and Management,* Vol. 12, No. 1, pp. 176-200, 2019

[13] F. J. Ebert, "Fundamentals of design and technology of rolling element bearings," *Chinese Journal of Aeronautics,* Vol. 23, No. 1, pp. 123-136, 2010

[14] M. M. Khonsari and R. E. Booser, Applied tribology: bearing design and lubrication, John Wiley & Sons, 2017

[15] Y. Yang , W. Yang and D. Jiang, "Simulation and experimental analysis of rolling element bearing fault in rotor-bearing-casing system," *Engineering Failure Analysis,* Vol. 92, pp. 205-221, 2018

[16] H. Cao, L. Niu, S. Xi and X. Chen, "Mechanical model development of rolling bearing-rotor systems: A review," *Mechanical Systems and Signal Processing,* Vol. 102, pp. 37-58, 2018

[17] O. Užga-Rebrovs and G. Kuļešova, "Comparative analysis of fuzzy set defuzzification methods in the context of ecological risk assessment," *Information Technology and Management Science,* Vol. 20, No. 1, pp. 25-29, 2017

[18] S. Naaz, A. Alam and R. Biswas, "Effect of different defuzzification methods in a fuzzy based load balancing application," *International Journal of Computer Science Issues (IJCSI),* Vol. 5, No. 8, p. 261, 2011

[19] L. Pokoradi, "Fuzzy logic-based risk assessment," *AARMS, Academic and Applied Research in Military Science,* Vol. 1, No. 1, pp. 63-73, 2002

[20] T. Obeidi, C. Larbes, A. Ilinca,G. F.T. Kebir, "Fuzzy Logic-based Maximum Power Point Tracking fora Solar Electric Vehicle," Acta Polytechnica Hungarica, Vol. 15, No. 7, pp. 133-156, 2018

[21] L. Pokorádi, B. Szamosi, "Fuzzy Failure Modes and Effects Analysis with Summative Center of Gravity DeFuzzification," 16th IEEE International Symposium on Computational Intelligence and Informatics, CINTI 2015, Budapest, Magyarország : IEEE, (2015) pp. 147-150

[22] L. Pokorádi, "Systems and Processes Modelling," Debrecen: Campus Kiadó, 2008 (in Hungarian)

[23] Gnip, P., Vokorokos, L., & Drotár, P. (2021) Selective oversampling approach for strongly imbalanced data. PeerJ Computer Science, 7, e604

Determining the Embedded Key Performance Indicator (KPI), based on a Fuzzy FxLMS Algorithm

Péter Pál Bakucz, József Zoltán Szabó

Bánki Donát Faculty of Mechanical and Safety Engineering, Óbuda University,
Institute of Mechatronics and Vehicle Engineering
Népszínház utca 8, 1081 Budapest, Hungary
szabo.jozsef@bgk.uni-obuda.hu, bakucz.peter@bgk.uni-obuda.hu

Abstract: In this work, we present the evaluation of the algorithmic performance of perception, achieved by a video sensor, within the framework of the Highly Automated Driving (HAD) project of the Óbuda University. We process the quality of the real-time uncertainty propagation in the embedded environment. The perception software could be characterized by algorithmic key performance indicators (KPIs) which is the measurable metric of the video sequences uncertainty. Based on endurance runs, for the real-time performance determination of the algorithms, an adaptive filter structure could be approximated. The employed performance architecture is a fuzzy-filtered (F-Fx) version of the LMS (Least Mean Square) algorithm in the embedded autonomous driving software platform. The F-FxLMS model is designed for the prediction of the embedded real-time filter outputs. The key performance indicator is related to the adaptation number of the F-FXLMS filter.

Keywords: Uncertainty Analysis; Fuzzy Filter; Fuzzy FxLMS (F-FxLMS) Algorithm; Highly Autonomous Driving; Software Performance

1 Introduction

Determining embedded KPIs (key performance indicators) by filtered LMS algorithms, with periodic and deterministic sensor *reference*, are often the subject of the measuring and managing the quality of platform design in the highly automated driving (HAD) software development process [1].

The two primary *reasons* of the periodic and deterministic references are: the embedded microcontroller environment simplification requirements, and it is generally easier to find a good reference signal to model them.

In addition to these reference signals, frequently stochastic signals are used in real autonomous driving projects today. The algorithms are mathematically classified into filtered LMS algorithm sequences [11]. However, based on highly autonomous driving (HAD) research at the University of Óbuda, we considered that the "classical" filtered LMS algorithm should be supplemented with fuzzy features (F-FxLMS) in order to facilitate the modeling of uncertainty propagation [2] [3].

In addition, the main reason for fuzzification [8] is the basic issue to be found in numerical analysis → when applying algorithms using classical deterministic references, there may be cases whose convergence has not been proved, which is called non-Wiener effects in the literature [9].

In previous work, which were presented at the SISY conference in 2019 [4], we showed in outline the steps of determining the software performance that can be used in the HAD project of the Óbuda University. Based on this, we present now a detailed analysis of the F-FxLMS algorithm and the test results performed with a vehicle with video sequences.

The essence of the adaptive filtering algorithm for determining embedded KPIs is based on the interpretation of the *transfer function* (*W* function) between different inputs and outputs.

Generally, to determine the embedded KPIs as a transfer function must be defined:

input *objects* (see Fig. 1) of the transfer *W* function of the F-FxLMS filter (in Óbuda University HAD Software see Fig. 1 defined by the Generation 5 video signals [11]), the environmental, digital signal processing *parameters* (period sampling), as well as uncertainty *values* on the *input* side [5].

At the same time, the *outputs* are the detected objects via object lists like object center, object width, and length. These parameters of the signal processing chain, are covering areas of the transfer function whose size far exceeds the unit, with the consequence that the number of interfering main pulses may increase [6].

The purpose of embedded filter-based performance analysis, is to define the maximum amount of transfer *W* function based on algorithmic uncertainty [7].

Determining the real-time filtering parameters for the optimal F-FxLMS illustrates, that it cannot be used to analyze stationary signals in specific frequency ranges. However, embedded considerations are needed to determine the duration of the entire system (in fuzzy filtering: via the neuro-estimated secondary path). These runtime additions extend the interpretation of the maximum stable filter parameter when viewing a specific frequency range.

The Matlab System Identification Toolbox [10] was recently released for the embedded, real-time analysis, of the classical FxLMS filtering and its filter behavior for autonomous driving projects, as approved for given microcontrollers.

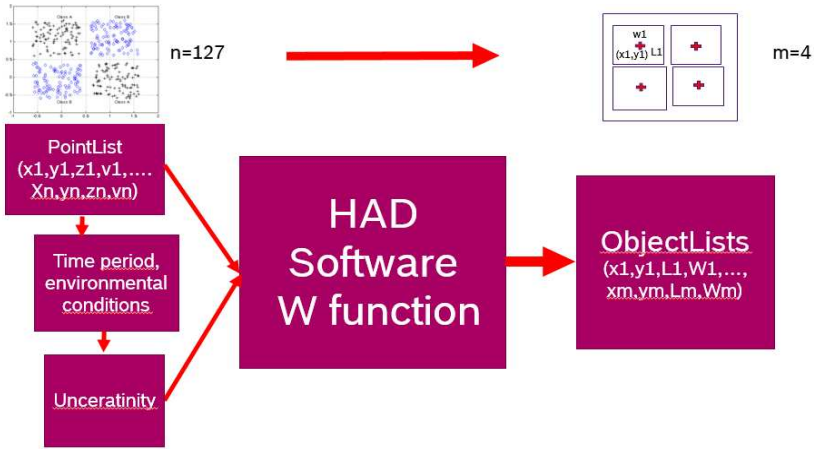

Figure 1

Óbuda University Human Autonomous Driving (HAD) software performance based on the input list (here n=127 video detected objects (points)) the time period, diverse environmental conditions, and the output (vehicle object lists; m=4, with centrum of the object x,y, and the width W and length L) (based on [14])

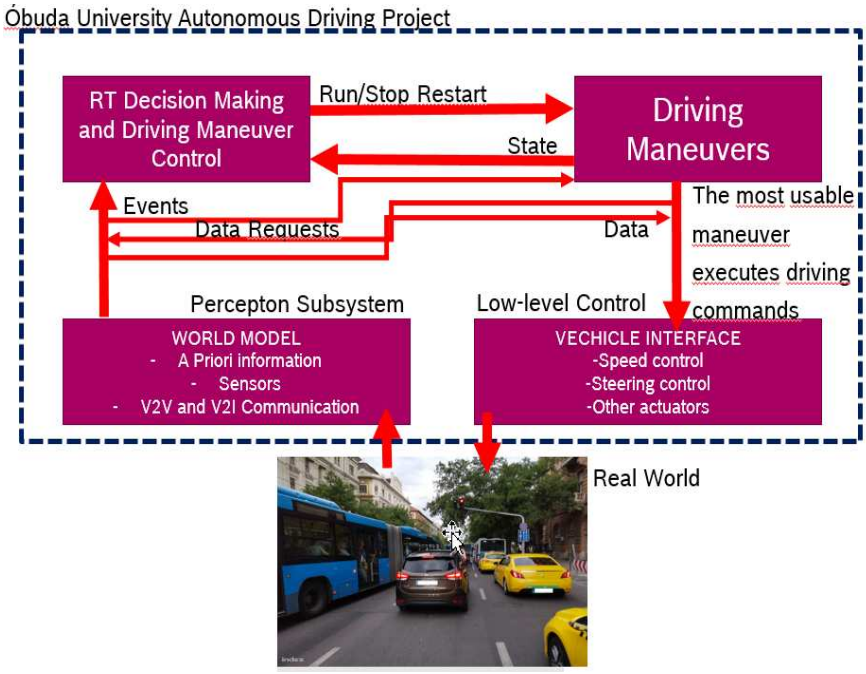

Figure 2

Autonomous Driving Control Application. The Óbuda University Autonomous Driving Project is engaged with the Perception Subsystem (video) software key performance indicators, KPIs [14].

In this work, we examine one of the software modules of the Software Sensing Subsystem of the Autonomous Driving Project of the Óbuda University and test our results in the real world as well in the form of testing with specific vehicles (Figures 3, 4). This software module is responsible for the sensor fusion detected on the video and radar channel, the "Perception" subclass.

To determine the embedded performance of the software module, we examined the analytical form of the *W* transfer function and the analysis of simple secondary sections with a clear delay. In possession of these, the maximum filter parameter of the F-FxLMS algorithm can be determined. Analysis of the poles of the *W* function provides data for the performance of the software module. This pole is related to the secondary path of the filter and the filter parameter and can be analytically expressed as required for embedded systems by maximizing the filter coefficients.

The application of the algorithm in the form of real-time measurements was performed within the framework of the Autonomous Driving Project of the University of Óbuda.

Our work presents in Sec. II, the basics of classical and fuzzy filtered (F-Fx) LMS algorithm. Afterward, in Sec. III, the designed procedure for autonomous driving software performance is presented. Sec. IV, provides the first results and Sec. V offers the Conclusions for this work.

Figure 3
Function structure of Óbuda University Autonomous Driving Software Sensor C++ system function component to be controlled by Fuzzy-FxLMS system [14]

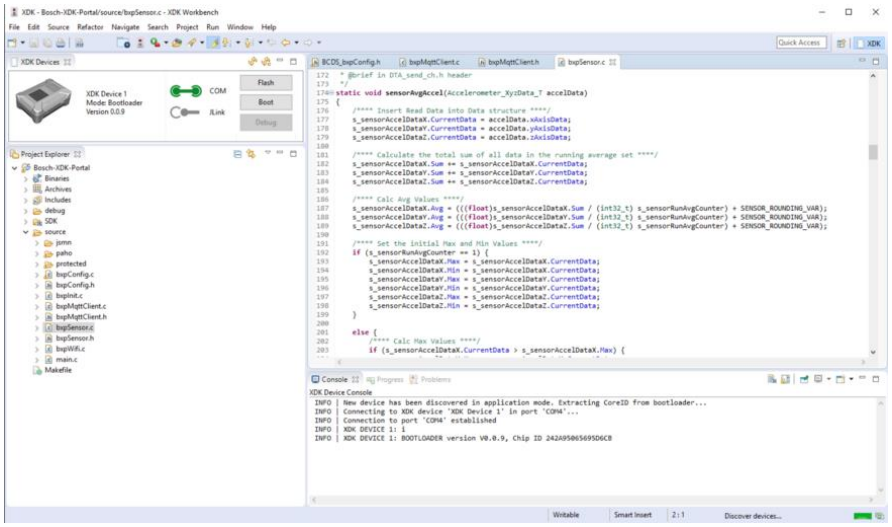

Figure 4
Eclipse Environment of Óbuda University Autonomous Driving Software Sensor C++ system function component to be controlled by Fuzzy-FxLMS system [14]

2 F-FxLMS Algorithm for KPI Determination

2.1 FxLMS Algorithm

In this chapter, we are engaged with the classical FxLMS embedded real-time active control of highly autonomous driving software system and controller functions defining embedded performance issues.

The classical (non-fuzzy) FxLMS algorithm can be applied to both feedback and feed-forward structures.

Figure 5, shows the block diagram of a feed-forward FxLMS system.

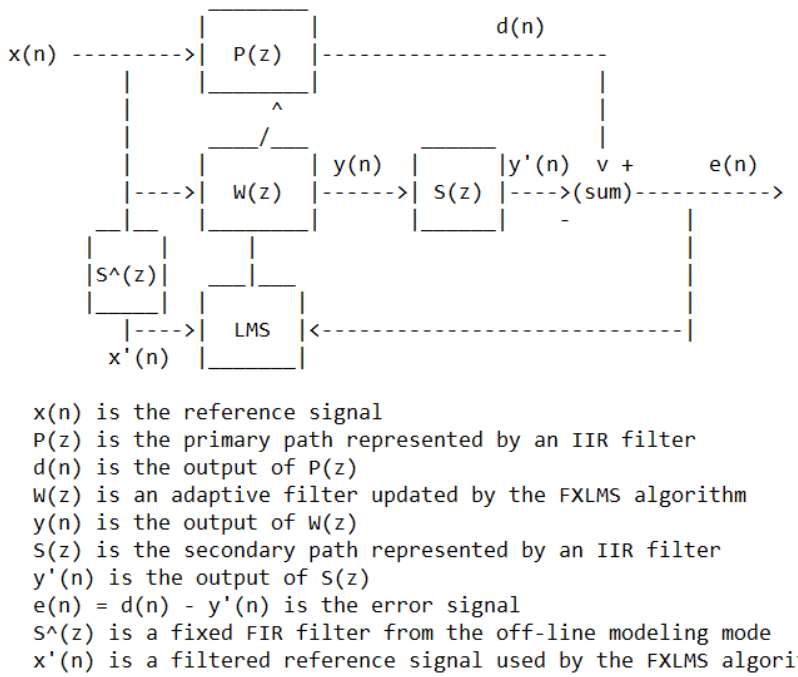

Figure 5

"Classical" FxLMS algorithm. In the fuzzy modified version, the off-line modeling mode of the secondary path is realized by a neural network with fuzzy activation functions focused on the convergence optimum of the real-time embedded growing equation

In Figure 5, $P(z)$ resolves the primary path between reference input signal source and error path. $S\hat{}(z)$ is purchased offline and fix stored during the real-time transaction of the performance determination, and z is the filter space variable, and n is the time-space variable [12] [13].

The interpretation for the residual error $e(n)$ is given as

$$e(n) = d(n) - y'(n) \tag{1}$$

where:

$y'(n)$ is the filter output $y(n)$ refined through the secondary path $S(z)$,

and $y'(n)$ and $y(n)$ computed as follows:

$$y'(n) = s^T(n)y(n) \tag{2}$$

$$y(n) = w^T(n)\, x(n) \tag{3}$$

where:

$$w(n) = [w_0(n),\, w_1(n), \ldots,\, w_{L-1}(n)]^T$$

is a weight vector, and

$x(n) = [x(n), x(n-1),\ldots,x(n-L+1)\ ]^T$

is the reference signal preferred by the reference signal.

Consequently, there is no feedback from the secondary path to the reference signal.

The FxLMS update equation for the coefficients of $W(z)$ is given as:

$$w(n+1) = w(n) + \mu e(n)x'(n) \tag{4}$$

where $x'(n)$ is the reference signal.

$x(n)$ refined through secondary path model $\hat{S}(z)$, and μ is the gain factor of the adaptive system [6] like:

$$x'(n) = \hat{S}^T(n)\, x(n) \tag{5}$$

2.2 Fuzzy FxLMS Algorithm

In the adaptive digital signal processing, one of the most usable controllers is the fuzzy-filtered (x) -least mean square (F-FxLMS) algorithm, which is based on the second-order moment of the $e(n)$ error signal (see Fig. 3) with non-periodical reference. The "fuzzy filtered" means that [8] [9]:

> ***The $\hat{S}(z)$ estimation path, the model of the secondary path $S(z)$, is realized with neural nets by fuzzy activation functions. These membership functions could be derived from measurement results so that the real-time growing equation is:***
>
> $w(n+1) = w(n) + \mu_F(n)e(n)x'(n)$
>
> ***converges and is optimal. Here the classical gain factor μ is also modified as a function ($\mu_F(n)$) and depends on the error function e(n).***

Technically, the new update equation is modified based on the thresholding parameters. In the available autonomous driving systems, these thresholding parameters need to be estimated offline with a secondary path neural network. They cannot be updated during the online operation of autonomous driving detection systems.

For an in-depth study on fuzzy filtered F-FxLMS algorithm with neural nets, the reader may refer to [8] [9].

3 Procedure

The spirit of the embedded KPI algorithm based on the F-FxLMS algorithm can be seen in Figure 6. In this case, the transfer function, realized by a filter *H(z)* is responsible for the adaptive filtering as a fuzzyfied transfer function between the input vector and the error signal *e(n)*, the "primary path", while *S(z)* is the secondary transfer function followed by *W(z)*, which identifies the embedded performance of the software.

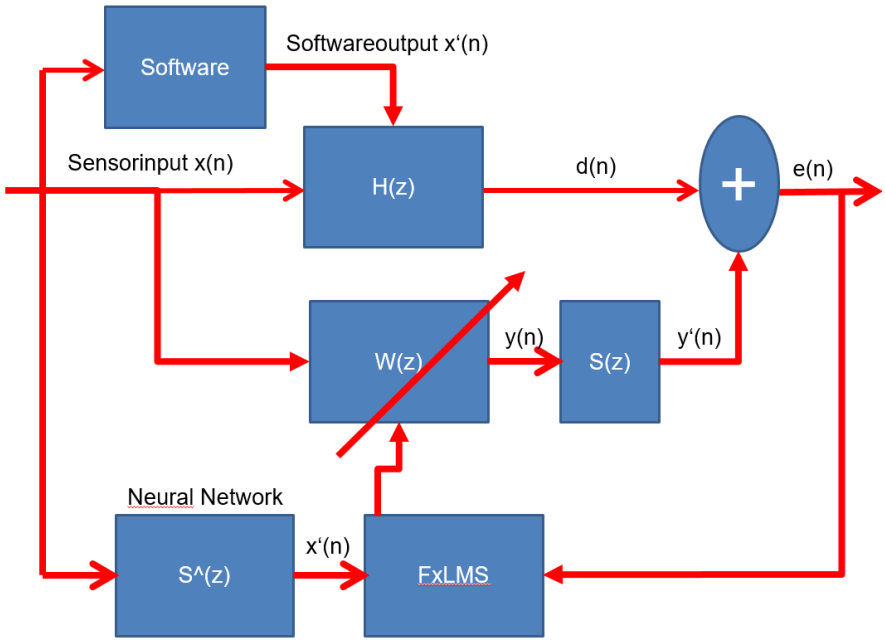

Figure 6
Detailed flow-chart of the procedure

The input video sensor signal *x(n)* is branched to three paths. First we passed it through the software module to be tested, where the *x'(n)* is obtained, thru the module algorithm and is passed secondly, to the transfer function *H(z)*.

In the third step, the video signal is applied to the adaptive filter *W(z)* and finally, to the block expressed by the neural network *S'(z)*, synthesizing the test results, which models the primary path.

We need to compare the output of this with the output of the software module to be tested, which can be done with the coefficients of the adaptive data channel filter *W(z)*.

The core of our F-FxLMS based procedure is that the strength (necessity) of the adaptation is proportional to the key performance of the software module.

That is, the closer we are to the metric of the learned video signals, or the fewer steps we have to realize for convergence, the more efficient the software module.

We can control the comparison and the convergence study with the F-FxLMS algorithm. The task of the primary path ($S(z)$) is to compare the signal $y(n)$ from the adaptive filter and the sensor input and the signal $d(n)$ of the sensor input modified by the software.

Another advantage of our method is that the neural network can be shaped easily by performing a sufficient number of tests. The neural network determines the direction of convergence and the nature of the reference. Otherwise, the method would not be possible in an embedded environment. With the right neural network model, the system can react immediately to changes in the input signal caused by changes in traffic systems. However, the performance of the software system depends primarily on the fuzzified transfer function of the neural network model of the secondary path.

4 Results

The embedded performance algorithm has been approved with the platform software of the Óbuda University (see Figure 2 before) using real data video and radar sequences.

In Figure 7 above, the video image is shown on the left, from which the sensor detects 137 possible objects.

The perception subsystem, where the real-time performance algorithm was placed, detected two objects (red crossed) as automobiles (out of 137), as shown above on the right in Figure 7. The figure below shows an image in a tunnel where the video chip indicated 1209 possible objects, but in reality, there is only one correct object (marked with a red cross).

In the form of crosses in yellow shown in Figure 8, the software error.

This error is expressed in a real-time adaptive manner by the F-FxLMS algorithm.

Figure 9 shows the performance of various measurements. The x-axis shows the time and the vertical axis, the performance value. Square objects are characterized by correct detection to characterize the increase in performance. The excellent quality of the fuzzy adaptive filter is characterized by the fact that the system can respond immediately to changes in the state in milliseconds.

The rectangles are also related to the quality of the video chip. Hardware impulses the appearance of objects.

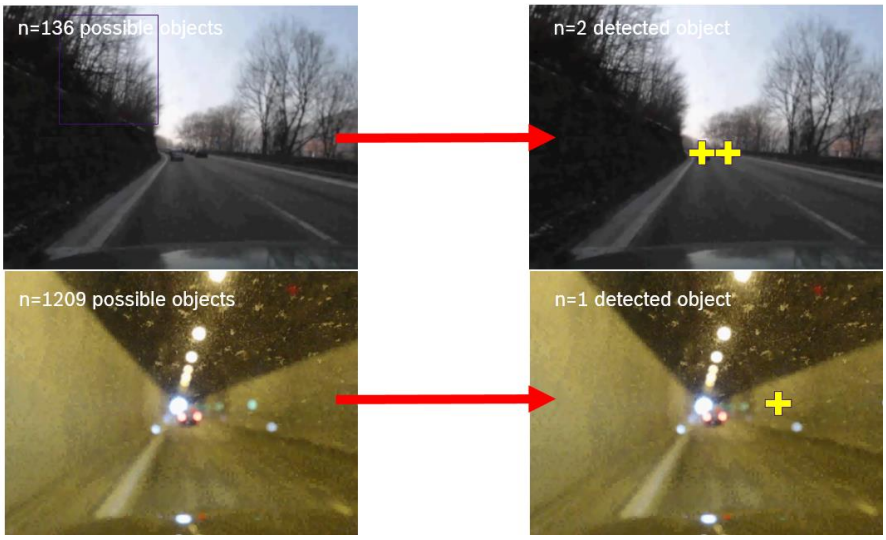

Figure 7

The video image is shown on the left, from which the sensor detects 137 possible objects. The perception subsystem, where the real-time performance algorithm was placed, detected two objects (yellow crossed) as automobiles (out of 137), as shown above on the right. The figure below shows an image in a tunnel where the video-chip indicated 1209 possible objects, but in reality there is only one correct object (marked with a yellow cross) but now is a wrong position.

Figure 10 shows a comparison of the algorithms (traditional FxLMS and the new fuzzy version we developed) based on 60 endurance (long-range) tests. The average KPI of the test indicated by a dot in the figure. In the figure on the left, where the test using the Video Generation 5 chip shown, it can be observed that the two methods provide approximately the same characteristics. However, there is a significant difference with the use of radar, which is shown in the figure on the right. It can be seen here that the fuzzy algorithm varies much more intensely based on tests than the traditional FxLMS algorithm. This is due to the detection uncertainty of the radar, which can be characterized by the intensification of the uncertainties. This fact is excellently represented by the new F-FxLMS algorithm.

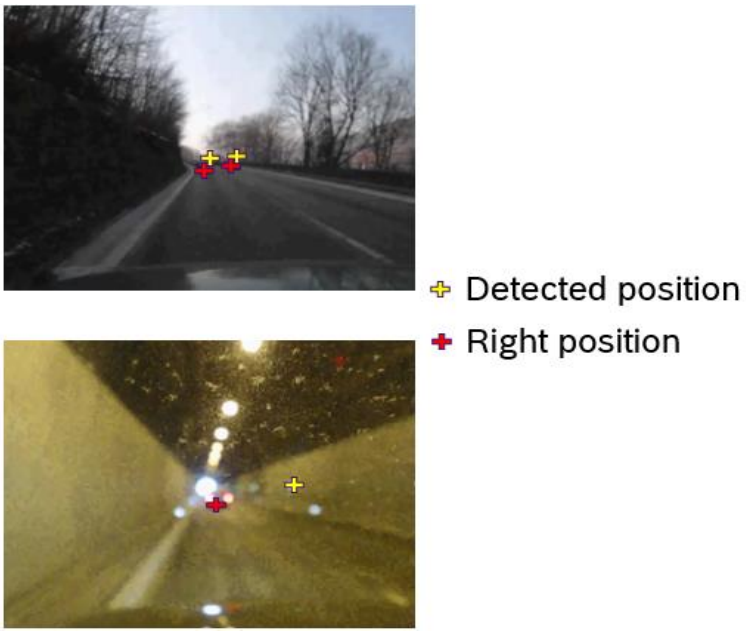

Figure 8

The distance between the detected (yellow) and software-provided (red) centers represents performance, which is determined by the necessary iteration step of the adaptive filter. This error is expressed in a real-time adaptive manner by the F-FxLMS algorithm.

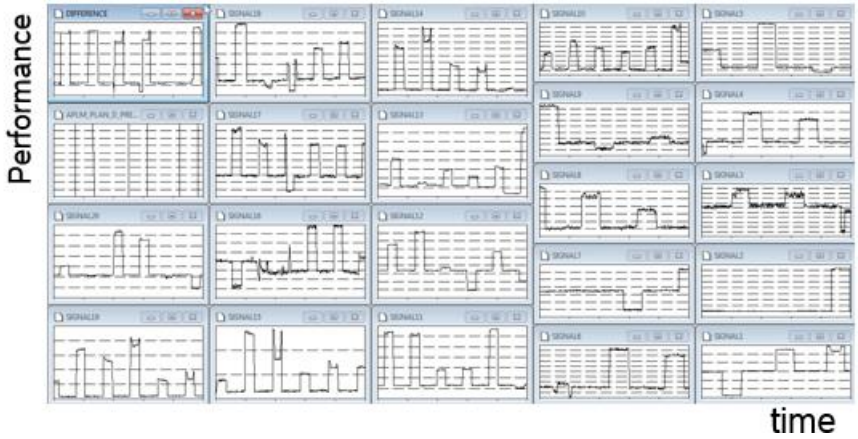

Figure 9

The performance diversity of various HAD video-based measurements. The x-axis shows the time and the vertical axis the performance value. Square objects are characterized by correct detection to represent the increase in performance. The good quality of the adaptive filter is symbolized by the fact that the system is able to respond immediately to changes in the state in milliseconds. The rectangles are also related to the quality of the video-chip

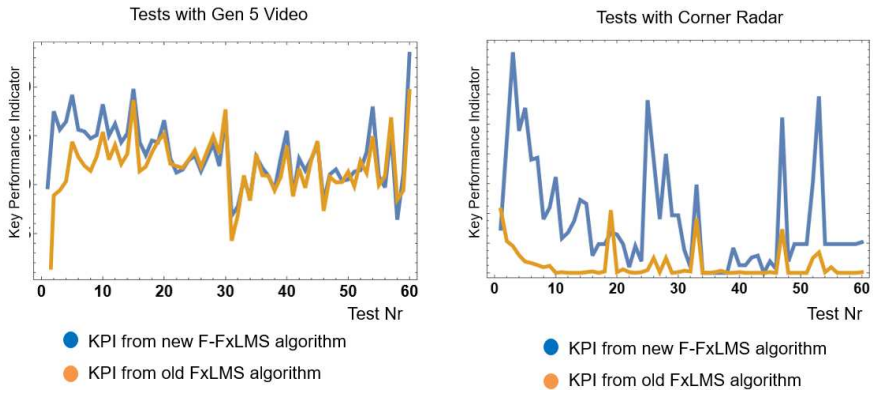

Figure 10

The KPI for video and radar long-range, endurance experiments, for FxLMS and our new fuzzy F-FxLMS algorithm

Conclusions

In this work, we tested the Highly Automated Driving (HAD) project, of Óbuda University. It is important to determine the quality of the various software elements, in an environment characterized by embedded microcontrollers, in real time, in the vehicle.

The advantage of the method, is that by performing a sufficient number of tests, the neural network based digital filter, could be seen as a key object defining the performance of a software module in a real environment. The neural network determines the direction of system convergence and the nature of the reference. Otherwise, the method would not be possible for use in an embedded environment.

With the right neural network model, the system can react immediately to changes in the input signal caused by changes in traffic systems. The performance of the software system depends primarily on the fuzzified transfer function of the neural network model of the secondary path.

During the first part testing the performance indicators of the HAD system, we performed endurance long-range vehicle tests where we can present the performance of the video and radar perception software module as a one-dimensional signal (see Figure 9).

This signal is determined in real time, i.e. when providing control of the vehicle, it provides useful information for possibly switching on other sensors, when performance decreases.

Our future plans for the HAD project and the definition of performance, include:

1) Development and implementation of an additional large number of test scenarios;

2) Involving the performance of other sensors;
3) Examine the performance of the sensor fusion algorithm;
4) The systematic alteration of neural networks.

References

[1] Anderson J. M. et al. 2016: Autonomous vehicle technology. Rand Corporation 2016, p. 214

[2] Beranek, L. Ver I. L. 1992: Noise and Vibration Control Engineering: Principles and Applications. New York: Wiley, 1992

[3] Hansen, C. H. Snyder, S. D. 1997: Active Control of Noise and Vibration. London, U. K.: E&FN Spon, 1997

[4] Szabó, J. Z., and Bakucz, P. 2019: "Determining Algorithmic Performance with Uncertainty Analysis." IEEE 17th International Symposium on Intelligent Systems and Informatics (SISY) IEEE, 2019

[5] Kuo, S. M., Morgan, D. R. 1996: Active Noise control systems, algorithms and DSP implementation functions, New York, Wiley 1996

[6] Widrow, M. Stearns, S. D. 1985: Adaptive Signal processing, Prentice Hall, New Jersey 1985

[7] Kuo, S. M Dipa Vijayan, M. D. 1997: A Secondary path modeling technique for Active Noise Control Systems. IEEE Transactions on Speech and Audio Processing, July 1997

[8] Zadeh, L. A. Fuzzy Sets. Information & Control. 1965, Vol. 8, pp. 338-353, ISSN 0019-9958

[9] Cintula, P. From Fuzzy Logic to Fuzzy Mathematics. PhD Thesis. FJFI CVUT Praha, 2004

[10] Mathworks Inc.: Matlab 2018b computer algebra software. System Identification Toolbox

[11] EE Automotive 5th generation of video sensors offers significantly higher resolution https://www.eenewsautomotive.com/news/

[12] Obeidi, T et al, 2018: Fuzzy logic-based maximum power point tracking for a solar electric vehicle. Acta Polytechnica Hungarica, Vol. 15, No. 7, 2018

[13] Y. Sun et al, 2019: A fuzzy brain emotional learning classifier design andapplication in medical diagnosis. Acta Polytechnica Hungarica, Vol. 16, No. 4, 2019

[14] Óbuda University: HAD Software Users Manual. Highly Autonomous Driving Platform. Budapest 2019

Parameter Estimation Methods for the FOPDT Model, using the Lambert W Function

Radmila Gerov[1], Tatjana V Jovanovic[2], Zoran Jovanovic[1]

[1]University of Nis, Faculty of Electronic Engineering, Aleksandra Medvedeva 14, 18000 Nis, Serbia, gerov@ptt.rs, zoran.jovanovic@elfak.ni.ac.rs

[2]University of Nis, Faculty of Medicine, Dr. Zoran Djindjic Boulevard 81, 18000 Nis, Serbia, tatjana@medfak.ni.ac.rs

Abstract: This paper discusses the estimation of the processes, that can be described by the first-order plus dead time, system model. Two methods of parameter estimation are proposed in this paper: the closed-loop under the proportional controller step test and the relay feedback test. The standard symmetrical relay and the preload relay, were used with the Relay feedback. Based on the data, from the recorded response, the parameters of the FOPDT model were estimated, by means of manual calculation using the Lambert W function. The produced results were compared to the results using other methods, in the current literature. Illustrated results were shown through a simulation of several different processes, as well as, with the example of the linearized model, of the pupillary light reflex system.

Keywords: Dead-Time System; FOPDT model; Parameters estimations; Relay feedback test; Closed-loop test; Lambert W function; pupillary light reflex system

1 Introduction

The main goal of feedback management is for the managed variable to be equal to or at least to deviate as little as possible from the desired value. To create an appropriate controller, which would satisfy all the requirements, it is necessary to understand the behavior of the controlled object in time, i.e. it is necessary to understand the dynamic characteristics of the controlled process. The majority of methods used for designing a controller demand a mathematical process model given in a certain form [1].

Taking into account that processes have different dynamic behavior, they can be described by means of different mathematical models. Models can be described in various ways: with the set of algebraic equations, regular differential equations, non-linear differential equations, etc. The mathematical model needs to portray

the process' dynamics for its analysis to be comprehensive and accurate. Adequate process control cannot be based on a poor mathematical model, as this would result in a poor design of different controllers, for example: The Linear Quadratic Regulators (LQR) [2], PI controllers [3], PID controllers [4], etc. Choosing an inadequate controller will not only result in unsatisfactory performance values of the controlling system but there is also a chance that the closed-loop control system will become unstable.

On the other hand, there are many processes that we are not acquainted with well enough, processes or systems that are affected by changes in the environment, as well as processes that show highly nonlinear behavior. Difficulties that occur in modeling and identification for this type of cases can be found for example: in robotics problems of modeling and identification of inertia and motor parameters for the PUMA 560 robot [5], difficulties of friction modelling and identification in precision positioning systems [6], parametric sensitivity in chemical reaction systems lead to large change in the temperature of the system [7]. For this reason, it is illusory to expect that in these practical cases a satisfactory, sufficiently precise model of a process or system can always be obtained.

In the past, the wide classes of nonlinear, adaptive, robust and intelligent controllers were developed for this type of systems. Research in adaptive control began in the middle of the last century [8] and was developed into an excellent control tool for many practical applications, e.g. adaptive fuzzy control was used for an uncertain teleoperation system [9]. The robust control approach has been applied in small turbojet engines [10]. Two sliding mode observers tracking control are used for robotic manipulators with uncertain kinematics and dynamics and unknown torques in [11]. Dynamic analysis and intelligent control (fuzzy logic, neural network, genetic algorithm) techniques for flexible manipulators for the time period 1970-2013 are summarized in [12]. Non-linear model predictive control has been used to avoid thermal runaway in semi-batch reactor [13]. For manipulating the feed rate in fed-batch fermentation processes different control strategies can be applied. In [14] was analyzed adaptive control, model predictive control, artificial neural networks and fuzzy control strategies applied in fed-batch fermentation processes.

Apart from the usage of mathematical models for the description of process behavior in the industry, using mathematical models, processes in other fields can be described as well. For example, the dynamics from the light amount reaching the retina to the pupil diameter is described with first-order plus time delay model in [15], the differential equation of the extended tumor growth model is given in [16], the pupil reflex to light has been considered as servomechanism in [17-19], the major features of cell growth and cell cycle in Saccharomyces cerevisiae is described by a coarse-grain model in [20], etc.

There exist different identification techniques used for determining the mathematical model of a dynamic system [21]. Apart from the usage of mathematical statistics, to process the collected data of a certain process, there can be found two other methods for the estimation of system model parameters in literature. For example, the neuro-fuzzy state-space model obtained from experimental data acquired from a real robotic arm [22], Kohohen's self-organizing maps, examinations of the classification of droplet epitaxial nanostructures [23], vehicle dynamic functions of the cars are obtained from its technical data [24], etc.

It is well known that for a Linear Time-invariant (LTI) system, that by, using the Laplace transformation, differential equations can be transcribed into algebraic equations, in other words, the dynamic characteristics of a process can be described using the transfer function. Most physical processes exhibit nonlinear behavior, but for great number of them the linear time invariant (LTI) models with time delay provide satisfactory model. Furthermore, a great number of controller configuration techniques is based on the system models whose transfer functions are of a lower order, such as first-order plus dead time (FOPDT) model, unstable first-order plus dead time (unstable FOPDT) model, second-order plus dead time (SOPDT) model, integrator plus dead time (IPDT) model, etc. The identification process techniques used for obtaining the previously mentioned lower-order system can be classified into two categories: the time-domain approach, examples [25]-[28], and the frequency domain approach, examples [29-33].

This paper considers parameter estimation of the FOPDT model. Two methods are suggested for the parameter estimation: The closed-loop under the proportional controller step test and the relay feedback test. The transcendental characteristic system equation in both suggested methods is solved by the usage of the Lambert W function (LWF) [34] [35]. The Lambert W function can be evaluated using the open source software the LambertW_DDE Toolbox [36]. Validation of the received FOPDT system model is done using the mean absolute error (MAE) and the root mean squared error (RMSE) index.

With the closed-loop under the proportional controller step test method, the step change is added to the setpoint. From the recorded response, to apply the suggested method, it is necessary to measure five parameters that are going to be used in the estimation of all the FOPDT model parameters [27] [28]. This method is illustrated in the example of the linearized model of the pupillary light reflex system.

The other suggested method for parameter estimation of the FOPDT model uses the standard symmetrical relay feedback test as well as the preload relay feedback test. In order to use this suggested method, it is necessary to measure the values of the amplitude and the oscillation period of the received response [34].

The results were compared to the results received using other methods from current literature. The quality of the suggested methods of parameter estimation of

the FOPDT model was compared by considering the original system model response and the received FOPDT models within the time and frequency domain.

This paper consists of several sections. The parameter estimation process of the FOPDT model using the closed-loop under proportional controller step test is given in Section 2. Section 3 portrays the parameter estimation process of the FODT model using the relay feedback test. Section 4 portrays the example of estimation with the linearized model of the pupillary light reflex system, while Section 5 presents the Conclusions and compares the results of the suggested methods, to the methods given in the current literature.

2 Parameter Estimation of FOPDT Model using Closed-Loop under Proportional Controller Step Test

2.1 Theoretical Background

The transfer function of FOPDT model, where K is the gain, T is the time constant and L is dead time, is:

$$G(s) = \frac{K}{Ts+1} e^{-Ls} \tag{1}$$

The closed-loop transfer function $W(s)$ of the FOPDT model under the proportional (P) controller, is:

$$W(s) = \frac{y(s)}{r(s)} = \frac{K_p G(s)}{1 + K_p G(s)} \tag{2}$$

where $y(s)$ is the Laplace transform of the controlled output, $r(s)$ is the Laplace transform of the reference step input amplitude R and K_p is the gain of the proportional controller.

Substituting the value $G(s)$ given in (1) into the equation in (2), it can be concluded that the closed-loop transfer function:

$$W(s) = \frac{K_p K}{Ts + 1 + K_p K e^{-Ls}} e^{-Ls} \tag{3}$$

It is well known that the closed-loop poles present the solution to the characteristic system equation. In this particular case, the characteristic equation of the closed-loop system is transcendental:

$$Ts+1+K_pKe^{-Ls}=0 \tag{4}$$

The characteristic system equation, given in (4), because of its transcendental nature has an infinite number of solutions, therefore *W(s)* has an infinite number of closed-loop poles, which can be calculated using the Lambert W function:

$$s_k=\frac{1}{L}W_k(-\frac{K_pK}{T}Le^{\frac{L}{T}})-\frac{1}{T} \tag{5}$$

where the s_k stands for k number of the closed-loop pole and k stands for an ordinal number of the Lambert W function branch.

It has been seen in literature, among which are [35] [37], that we can get the rightmost closed-loop poles if the ordinal number of the Lambert W function branch is equal to 0 or -1. Taking into account that rightmost closed-loop poles greatly affect the dynamic characteristics i.e. the system response, for the suggested system parameter estimation method, it is enough just to consider them. The rightmost closed-loop poles (s_1 and s_2), are received from the expression given in (5), for k=0 and k=-1:

$$\begin{aligned} s_1&=\frac{1}{L}W_0(-\frac{K_pK}{T}Le^{\frac{L}{T}})-\frac{1}{T}\\ s_2&=\frac{1}{L}W_{-1}(-\frac{K_pK}{T}Le^{\frac{L}{T}})-\frac{1}{T} \end{aligned} \tag{6}$$

On the other hand, the closed-loop transfer function *W(s),* after the approximation of the dead time from the denominator, can be considered as the second-order plus dead time system model with dynamic numerators as shown in [27]. In that case, closed-loop poles, where ξ is a damping ratio and ω_n is natural frequency, are:

$$\begin{aligned} s_1&=-\xi\omega_n+j\omega_n\sqrt{1-\xi^2}\\ s_2&=-\xi\omega_n-j\omega_n\sqrt{1-\xi^2} \end{aligned} \tag{7}$$

From equations (6) and (7) we get:

$$\begin{aligned} -\xi\omega_n+j\omega_n\sqrt{1-\xi^2}&=\frac{1}{L}W_0(-\frac{K_pK}{T}Le^{\frac{L}{T}})-\frac{1}{T}\\ -\xi\omega_n-j\omega_n\sqrt{1-\xi^2}&=\frac{1}{L}W_{-1}(-\frac{K_pK}{T}Le^{\frac{L}{T}})-\frac{1}{T} \end{aligned} \tag{8}$$

2.2 Algorithm for Parameter Estimation of the FOPDT Model

Step 1: By choosing the appropriate proportionate regulator K_p gain, we can ensure that the underdamped closed-loop step response is obtained. A typical response is shown in Figure 1.

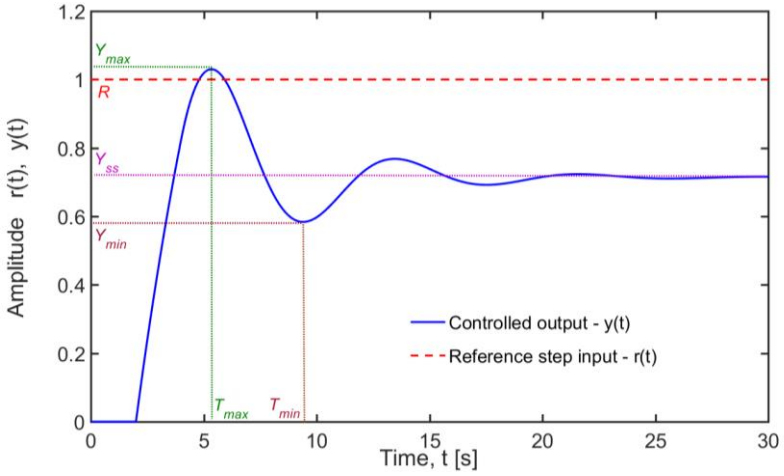

Figure 1
Underdamped closed-loop step response of the FOPDT model under proportional control

Step 2: From the received response, read the values Y_{max}, Y_{min}, Y_{ss}, R, T_{max}, T_{min}, necessary for the application of the suggested estimation [18], as shown in Fig. 1.

Step 3: Calculate the damping ratio ξ, natural frequency ω_n, and gain K of the FOPDT model using equations (9), (10) and (11), respectively:

$$\xi = \frac{-\ln\left(\frac{Y_{ss} - Y_{\min}}{Y_{\max} - Y_{ss}}\right)}{\sqrt{\pi^2 + \ln\left(\frac{Y_{ss} - Y_{\min}}{Y_{\max} - Y_{ss}}\right)^2}} \tag{9}$$

$$\omega_n = \frac{\pi}{(T_{\min} - T_{\max})\sqrt{1-\xi^2}} \tag{10}$$

$$K = \frac{Y_{ss}}{K_p(R - Y_{ss})} \tag{11}$$

Step 4: Substitute the received values of damping ratio ξ, natural frequency ω_n, and gain K of the FOPDT model in the two equations given in (8). Solving the

system of two equations with two unknowns *T*- the time constant and *L*-the dead time, all the parameters of the FOPDT model have been estimated.

Step 5: Validate the received FOPDT model using the Mean Absolute Error (MAE) and the Root Mean Squared Error (RMSE) indexes in the time domain, where y is the output of the real system and y_m represented output of FOPDT model.

$$MAE = \frac{1}{n}\sum_{i=0}^{n}|y - y_m|$$
$$RMSE = \sqrt{\frac{1}{n}\sum_{i=0}^{n}(y - y_m)^2} \tag{12}$$

Other performance indexes known to literature can also be used for the validation of the received FOPDT model.

3 Parameter Estimation of the FOPDT Model using the Conventional Symmetrical Relay and the Preload Relay Feedback Test

3.1 Theoretical Background

It is known that the relay belongs to the group of nonlinear elements where static characteristics are described by mathematical models whose complexity depends on the type of nonlinearity. Ambiguous nonlinearities, e.g. relays with hysteresis, are described by functional dependence:

$$u(t) = F\left(e(t), \frac{de(t)}{dt}\right) \tag{13}$$

where $u(t)$ is the relay output, $e(t)$ is the output error (the relay input) and $\dot{e}(t)$ is the derivative of $e(t)$. With unambiguous nonlinearities, for example, the ideal relay, $\dot{e}(t)=0$.

Block diagram control system used for the conventional relay feedback test, where r denotes the desired variable (the set-point), y the controlled variable (the process output), u the manipulated variable (the relay output), and e the output error, is shown in Figure 2.

Symmetrical (unbiased) relay and asymmetrical (biased) relay feedback tests are used in the identification process procedure. Techniques based on relay feedback identification methods can be classified into three groups: the describing function

method, the use of frequency response estimation for model fitting, and the curve fitting approach. The methods used in the paper are the unbiased relay method and the describing function method.

The describing function of the relay represented the complex ratio of the fundamental harmonic relay output to the sinusoidal relay input.

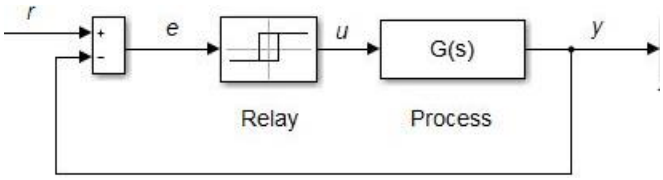

Figure 2
Block diagram of a conventional relay feedback test

The describing function for the unbiased relay with hysteresis *N(A)* [33], where *h* is the relay amplitude, ε is the switch hysteresis and *A* is the amplitude of the output oscillations, is:

$$N(A)=\frac{4h}{\pi A}e^{-j\arcsin\left(\frac{\varepsilon}{A}\right)}=\frac{4h}{\pi A}\left(\sqrt{\left(1-\frac{\varepsilon^2}{A^2}\right)}-j\frac{\varepsilon}{A}\right) \tag{15}$$

The describing function of the relay is a transfer function of a relay for a given frequency. The describing function of the ideal relay is received for the expression in (15) for ε=0. The magnitude of the ideal relay and unbiased relay with hysteresis is equal. As opposed to the ideal relay where the phase is zero, the unbiased relay with hysteresis introduces the phase shift.

It is well known that under an unbiased relay test (the set-point *r(t)*=0) the process response moves into the limit cycle. The ultimate gain K_u is approximately equal to:

$$K_u=\frac{4h}{\pi A} \tag{16}$$

The ultimate frequency ω_u, where P_u ultimate period, is equal to:

$$\omega_u=\frac{2\pi}{P_u} \tag{17}$$

The process in Figure 2, is described by the transfer function of the FOPDT model *G(s)* with the parameters given in (1) and the relay described by the transfer function *N(A)* given in (15). Characteristic system equation shown in Figure 2 is:

$$1+N(A)G(s)=0 \tag{18}$$

Substituting the expression for $G(s)$ given in (1) into equation (18), as well as, using some mathematical arrangement, the following is obtained:

$$s_k = \frac{1}{L} W_k\left(-\frac{N(A)K}{T} L e^{\frac{L}{T}}\right) - \frac{1}{T} \tag{19}$$

Taking into account that the process response from Figure 2 moves into the limit cycle under unbiased relay, then there exist two conjugated complex closed-loop poles with real parts equal to zero and imaginary parts $\pm j\omega_u$. These poles are rightmost closed-loop poles which can be calculated using the equation (19) for k=0 and k=-1, therefore:

$$\begin{aligned} +j\omega_u &= \frac{1}{L} W_0\left(-\frac{N(A)K}{T} L e^{\frac{L}{T}}\right) - \frac{1}{T} \\ -j\omega_u &= \frac{1}{L} W_{-1}\left(-\frac{N(A)K}{T} L e^{\frac{L}{T}}\right) - \frac{1}{T} \end{aligned} \tag{20}$$

If the process response moves into the limit cycle, for ultimate frequency ω_u, then:

$$\left|N(A)G(j\omega_u)\right| = \left|\frac{N(A)K}{\sqrt{(\omega_u T)^2 + 1}}\right| = 1 \tag{21}$$

If gain K>0. Since the expression under the root in the denominator of the equation (21) is always greater than zero, from (21) it can be seen that:

$$\left|N(A)\right| K = \sqrt{(\omega_u T)^2 + 1} \tag{22}$$

Substituting the expression (22) into (20), the following is produced:

$$\begin{aligned} +j\omega_u &= \frac{1}{L} W_0\left(-\frac{\sqrt{(\omega_u T)^2 + 1}}{T} e^{-j\arcsin\left(\frac{\varepsilon}{A}\right)} L e^{\frac{L}{T}}\right) - \frac{1}{T} \\ -j\omega_u &= \frac{1}{L} W_{-1}\left(-\frac{\sqrt{(\omega_u T)^2 + 1}}{T} e^{-j\arcsin\left(\frac{\varepsilon}{A}\right)} L e^{\frac{L}{T}}\right) - \frac{1}{T} \end{aligned} \tag{23}$$

For the ideal relay ε=0, equations (23) are reduced to:

$$\begin{aligned} +j\omega_u &= \frac{1}{L} W_0\left(-\frac{\sqrt{(\omega_u T)^2 + 1}}{T} L e^{\frac{L}{T}}\right) - \frac{1}{T} \\ -j\omega_u &= \frac{1}{L} W_{-1}\left(-\frac{\sqrt{(\omega_u T)^2 + 1}}{T} L e^{\frac{L}{T}}\right) - \frac{1}{T} \end{aligned} \tag{24}$$

Depending on the type of relay used, the FOPDT model, the time constant T, and the dead time L are received by solving the system equations given in (23) or (24). The gain of the FOPDT model, not depending on the type of relay, can be calculated using equation (25):

$$K = \frac{\pi A}{4h}\sqrt{\left(\omega_u T\right)^2 + 1} \tag{25}$$

It is well known that by using the unbiased relay feedback test, an error occurs in the estimation of the ultimate gain K_u, that is, in the magnitude of the describing function of the relay. For this reason, the estimated value of the gain of the FOPDT model, received using equation (25), also deviates from the true value. Value estimation of the gain K is better done using equation (11), for the closed-loop under proportional controller step test where $K_p<K_u$ or using the preload relay [33].

The preload relay can be considered a relay where the proportional controller is connected in parallel to the ideal relay. The gain of the proportional controller is less than the relay amplitude h, and is equal mh, where $m<0.5$. The describing function of the preload relay is:

$$N(A) = \frac{4h}{\pi A} + mh \tag{26}$$

The gain K of the FOPDT model, using the preload relay feedback test, can be calculated using equation (27) as follows:

$$K = \frac{\pi A}{h\left(4 + \pi A m\right)}\sqrt{\left(\omega_u T\right)^2 + 1} \tag{27}$$

In methods known to literature that use the unbiased relay feedback test for the FOPDT model parameter estimation, it is necessary to know either the gain K or the dead time L, and the other two parameters are received by solving the two equations. Using the suggested method, it is not necessary to estimate the dead time of the FOPDT model from the limit cycle process response, nor is it necessary to know the gain K of the FOPDT model. It is only necessary to measure the amplitude of the output oscillations A and the ultimate period P_u.

3.2 Algorithm for Parameter Estimation of the FOPDT Model using the Relay Feedback Test

Step 1: Use the unbiased relay feedback test as in Figure 2. The reference input $r(t)$, the ideal relay output $u(t)$, and the process response $y(t)$, is shown in Figure 3.

Step 2: From the received response, read the following values: the process response amplitude A and the ultimate period P_u, for the applied value the relay amplitude h, in the manner shown in Figure 3.

Step 3: Calculate the ultimate frequency ω_u using equality in (17).

Step 4: Substitute the received value of the ultimate frequency ω_u into the system of two equations (24). Solving the system equations, the time constant T and the dead time L of the FOPDT model are estimated.

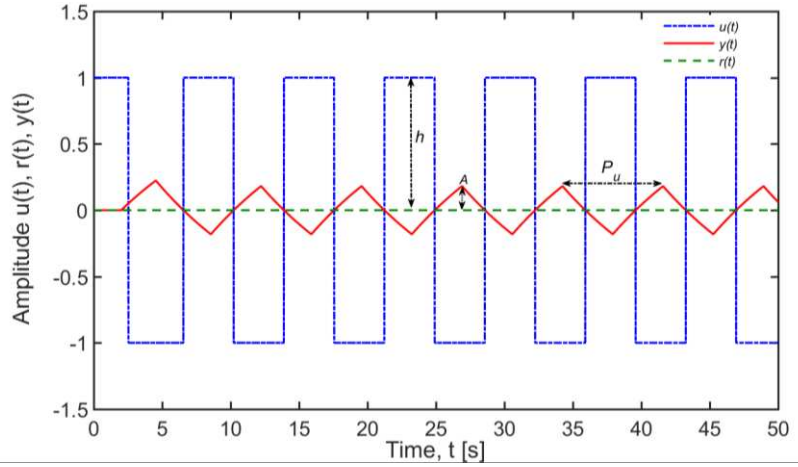

Figure 3
Limit cycle response of FOPDT model under ideal relay feedback test

Step 5: Using equation (25) calculate the gain K of the FOPDT model.

In this way, all parameters of the FOPDT model using the ideal relay feedback test were estimated. With the unbiased relay with the hysteresis feedback test, the only difference is in *Step 4* of the suggested algorithm where for the estimation of the time constant T and the dead time L of FOPDT model equations in (23) are used. With the preload relay feedback test in *Step 5* of the suggested algorithm, the gain K of the FOPDT model should be calculated using equations in (27).

Step 6: This step can be applied to achieve better estimation results of the gain K of the FOPDT model. Use the closed-loop under the proportional controller step test for $K_p < K_u$, as explained in the previous Chapter. From the received response read the steady-state value of the output Y_{ss}. For the known value of the amplitude step input R, the gain K should be estimated using the equation in (11).

4 Simulation Study

4.1 Simulation Study using Closed-Loop under Proportional Controller Step Test

The transfer function of the linearized model of pupillary light reflex [17]-[19], which represents the ratio of the change of flux due to pupil-area alteration $Iref\Delta A$ and change of flux due to external light variation $Aref\Delta I$, is given as the third-order plus time delay model:

$$G(s) = \frac{I_{ref}\,\Delta A}{A_{ref}\,\Delta I} = \frac{(\Delta A / A_{ref})}{(\Delta I / I_{ref})} = \frac{Ke^{-Ds}}{(1+\tau s)^3} = \frac{0.16e^{-0.18s}}{(1+0.1s)^3} \tag{28}$$

Step 1: Closed-loop unit step response with gain K_p=5 and the reference step input amplitude R=1

Step 2: From the received closed-loop step response the parameters are: Y_{max}=0.6330, Y_{min}=0.36805,Y_{ss}=0.4444, R=1, T_{max}=0.6735, T_{min}=1.1165

Step 3: Calculated parameters from equations (9 thru 11) respectively are: ξ=0.7892, ω_n=1.7051, the identified FOPDT model gain K=0.16

Step 4: From equation (8) the identified FOPDT model time constant and dead time are: T=0.2014, L=0.3169

Step 5: Model validation in time domain (simulation time is 2s): MAE=0.00308, RMSE=0.00513

The received FOPDT was compared to the FOPDT model received using the Half-rule technique [26] with the following parameters K=0.16, T=0.15 and L=0.33. Model validation in time domain for Half-rule FOPDT model (simulation time is 2s): MAE=0.00240, RMSE=0.00548.

Unit step response of the linearized model of pupillary light reflex, proposed identified FOPDT model and Half rule FOPDT model is shown in Figure 4.

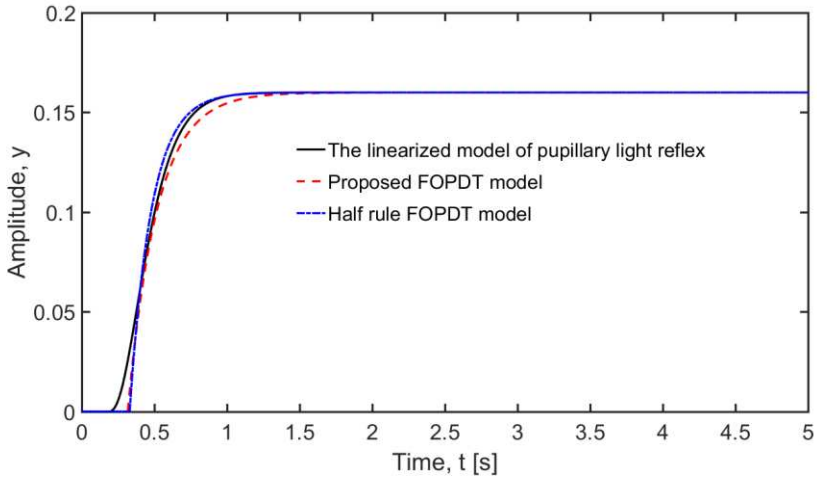

Figure 4
Unit step response of the linearized model of pupillary light reflex and identified FOPDT models

Nyquist fitting of identified FOPDT models for a linearized model of the pupillary light reflex is shown in Figure 5.

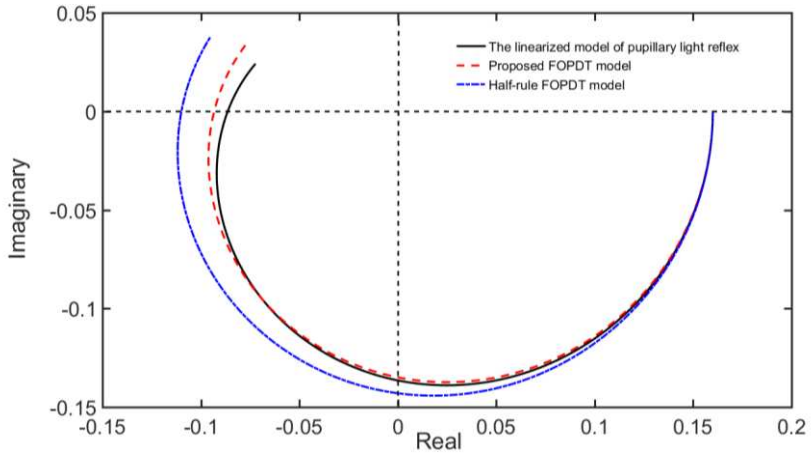

Figure 5
Nyquist fitting of identified FOPDT models for a linearized model of the pupillary light reflex

The gain margin of a linearized model of the pupillary light reflex is GM=21.3 dB and phase crosover freqency ω=7.13 rad/s. The same parameteres for the proposed FOPDT model are: GM=20.6 dB, ω=6.92 rad/s and for Half-rule FOPDT models are: GM=19.2 dB, ω=7.05 rad/s.

Based on the given characteristics of the FOPDT model in the time and frequency domain, it can be concluded that the Half-rule FOPDT model represents the characteristics of the linearized model of the pupillary light reflex in time domain more accurately, while the suggested FOPDT model provides better results in the frequency domain.

Comparison results of the suggested parameter estimation method of the FOPDT model with methods from literature are considered in [28] for the following examples: first-order plus time delay system, eight-order plus time delay system and non-minimum-phase time delay system.

4.2 Simulation Study using Relay Feedback Test

Parameter estimation of the FOPDT model is given in the example of the Wood-Berry distillation column model (WB column) [38] as follows:

$$G(s) = \frac{12.8}{16.7s+1} e^{-s} \tag{29}$$

Step 1: The unbiased relay feedback with the relay amplitude h=1

Step 2: From the limited cycle response, the following values were measured: the process response amplitude A=0.7442 and the ultimate period P_u=3.9 s.

Step 3: From equations (17) ultimate freqency ω_u=1.611 rad/s was calculated.

Step 4: From equation (24) the identified FOPDT model time constant and time delay are: T=14.005, L=1.

Step 5: From equation (25) the gain of FOPDT model K=13.166.

The identified FOPDT model using the unbiased relay feedback test, is:

$$G_1(s) = \frac{13.166}{14.005s+1} e^{-s} \tag{30}$$

Step 6: The closed-loop under proportional controller step test with K_p=1.5 (K_p<1.715) and the reference step input amplitude R=1. From the closed-loop response, the steady state value of the output Y_{ss}=0.95. From equation (11) the gain of FOPDT model K=12.8.

The identified FOPDT model using the same feedback test and Step 6, is:

$$G_2(s) = \frac{12.8}{14.005s+1} e^{-s} \tag{31}$$

Parameter estimation was also performed using the preload relay with describing function (26), with m=0.2 and the relay amplitude h=1. From the limited cycle response the following values were measured: the process response amplitude

A=0.7991 and the ultimate period P_u=3.89 s. From equations (17) ultimate freqency ω_u=1.615 rad/s was calculated. From equation (24) the identified FOPDT model time constant and time delay are: T=13.993, L=0.999. From equation (27) the gain of FOPDT model is K=12.616.

The identified FOPDT model using the preload relay feedback test, is:

$$G_3(s) = \frac{12.616}{13.993s+1} e^{-0.999s} \tag{32}$$

Unit step response of the WB column and the identified FOPDT models are shown in Figure 6.

Model validation in time domain (simulation time is 100 s): for the identified FOPDT model $G_1(s)$: MAE=0.65, RMSE=0.70, the identified FOPDT model $G_2(s)$: MAE=0.34, RMSE=0.44, the identified FOPDT model $G_3(s)$: MAE=0.27, RMSE=0.35.

The gain margin of the WB column is GM=6.44 dB and ultimate freqency ω_u=1.61 rad/s. The same parameteres for the FOPDT models $G_1(s)$ are: GM=4.71 dB, ω_u=1.61 rad/s, for the FOPDT models $G_2(s)$, GM=4.95 dB, ω_u=1.61 rad/s and for the FOPDT models $G_3(s)$, GM=5.08 dB, ω_u=1.62 rad/s.

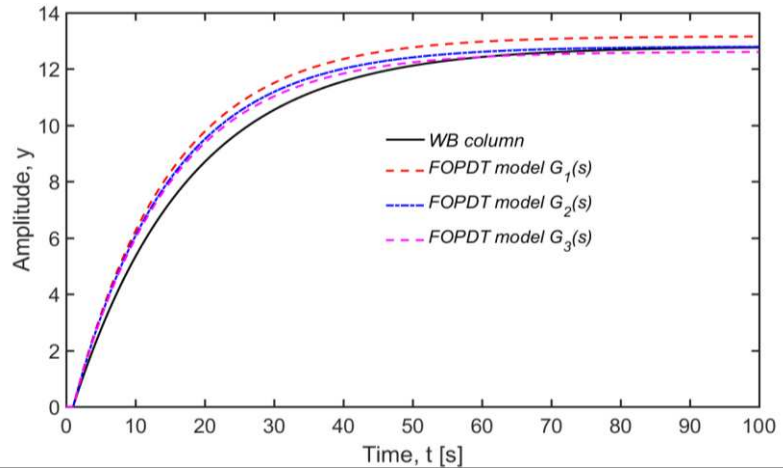

Figure 6
Unit step response of the WB column and identified FOPDT models

The gain margin of the WB column is GM=6.44 dB and ultimate freqency ω_u=1.61 rad/s. The same parameteres for the FOPDT models $G_1(s)$ are: GM=4.71 dB, ω_u=1.61 rad/s, for the FOPDT models $G_2(s)$, GM=4.95 dB, ω_u=1.61 rad/s and for the FOPDT models $G_3(s)$, GM=5.08 dB, ω_u=1.62 rad/s.

Nyquist fitting of the identified FOPDT models for a linearized model of WB column is shown in Figure 7.

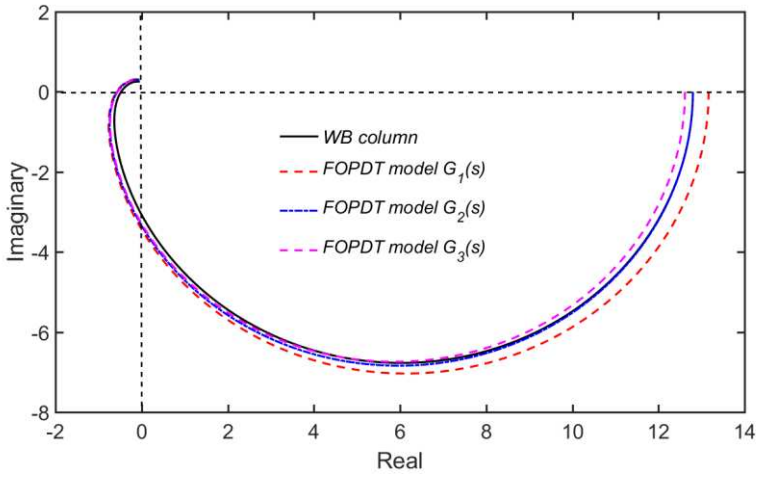

Figure 7
Nyquist fitting of identified FOPDT models for a WB column

It is obvious that the identified FOPDT model $G_1(s)$ in comparison to the other two identified models doesn't represent the WB column in time and frequency domain as accurate as the two models. Using Step 6 of the method, the estimated gain is received compared to the gain of the FOPDT model received using formula (25). Using the preload relay feedback test, the parameters of the FOPDT models are better estimated.

Conclusions

The application of the Lamber W function, in the unbiased relay test, allows for the estimation of all the parameters of the FOPDT model to be estimated without prior knowledge of either the gain or dead time, as opposed to other methods, in the literature, where it is necessary to know at least one of the two aforementioned parameters, or to read the dead time, from the obtained response.

References

[1] K. J. Åström, T. Hägglund: PID Controllers: Theory, Design, and Tuning, Research Triangle Park, North Carolina, Instrument Society of America, 1995

[2] R. Zhang, F. Gao, Z. Cao, P. Li: Design and implementation of an improved linear quadratic regulation control for oxygen content in a coke furnace, IET Control Theory and Applications, Vol. 8, No. 14, 2014, pp. 1303-1311

[3] R. Gerov, Z. Jovanovic: Synthesis of PI Controller with a Simple Set-Point Filter for Unstable First-Order Time Delay Processes and Integral plus Time Delay Plant, Elektronika Ir Elektrotechnika, Vol. 24, No. 2, 2018, pp. 3-11

[4] T. Haidegger, L. Kovács, R. E. Precup, B. Benyó, Z. Benyó, S. Preitl: Simulation and control for telerobots in space medicine, Acta Astronautica, Vol. 81, No. 1, 2012, pp. 390-402

[5] P. I. Corke, B. Armstrong-Helouvry: A search for consensus among model parameters reported for the PUMA 560 robot, Proceedings of the 1994 IEEE International Conference on Robotics and Automation, San Diego, CA, USA, Vol. 2, 1994, pp. 1608-1613

[6] L. Márton, B. Lantos: Identification and model-based compensation of Striebeck friction, Acta Polytechnica Hungarica, Vol. 3, No. 3, 2006, pp. 45-58

[7] J. Jiang, J. Jiang, Z. Wang, Y. Pan: Thermal runaway criterion for chemical reaction systems: A modified divergence method, Journal of Loss Prevention in the Process Industries, Vol. 40, 2016, pp. 199-206

[8] R. Isermann, K. H. Lachmann, D. Matko: Adaptive control systems, Prentice-Hall International, Hemel Hempstead, U.K., 1992

[9] L. Yang, Y. Chen, Z. Liu, K. Chen, Z. Zhang: Adaptive Fuzzy Control for Teleoperation System with Uncertain Kinematics and Dynamics, International Journal of Control, Automation and Systems, Vol. 17, 2019, pp. 1158-1166

[10] R. Andoga, L. Főző, R. Kovács, K. Beneda, T. Moravec, M. Schreiner: Robust Control of Small Turbojet Engines, Machines, Vol. 7, No. 3, 2019, pp. 1-14

[11] B. Xiao, S. Yin, O. Kaynak: Tracking Control of Robotic Manipulators With Uncertain Kinematics and Dynamics, IEEE Transactions on Industrial Electronics, Vol. 63, No. 10, 2016, pp. 6439-6449

[12] H. N. Rahimi, M. Nazemizadeh: Dynamic analysis and intelligent control techniques for flexible manipulators: a review, Advanced Robotics, Vol. 28, No. 2, 2013, pp. 63-76

[13] Alex Kummer, Tamás Varga, Lajos Nagy: Semi-batch reactor control with NMPC avoiding thermal runaway, Computers & Chemical Engineering, Vol. 134, 2020, pp. 1-10

[14] L. Mears, S. M. Stocks, G. Sin, K. V. Gernaey: A review of control strategies for manipulating the feed rate in fed-batch fermentation processes, Journal of Biotechnology, Vol. 245, 2017, pp. 34-46

[15] A. Amodio, M. Ermidoro, D. Maggi, S. M. Savaresi: A low-cost system for dynamic analysis of pupillary light response for a driver drowsiness

detection system, Proceedings IEEE European Control Conference (ECC), 2018, pp. 2691-2696

[16] D. A. Drexler, T. Ferenci, A. Lovrics, L. Kovacs: Tumor dynamics modeling based on formal reaction kinetics, Acta Polytechnica Hungarica, Vol. 16, No. 10, 2019, pp. 31-44

[17] L. Stark: Stability, oscillations, and noise in the human pupil servomechanism, Proceedings of the IRE, Vol. 47, No. 11, 1959, pp. 1925-1939

[18] L. Stark: Environmental clamping of biological systems: pupil servomechanism, Journal of the Optical Society of America, Vol. 52, No. 8, 1962, pp. 925-930

[19] L. Stark, P. M. Sherman: A servoanalytic study of consensual pupil reflex to light, Journal of Neurophysiology, Vol. 20, 1957, pp. 17-26

[20] P. Palumbo, F. Papa, M. Vanoni, L. Alberghina: A coarse-grain model of growth and cell cycle in Saccharomyces cerevisiae: a mathematical analysis, Acta Polytechnica Hungarica, Vol. 16, No. 10, 2019, pp. 205-224

[21] L. Ljung: System Identification-Theory for the User, Prentice-Hall, Englewood Cliffs, New Jersey, 1987

[22] A. Chatterjee, R. Chatterjee, F. Matsuno, T. Endo: Augmented stable fuzzy control for flexible robotic arm using LMI approach and neuro-fuzzy state space modeling, IEEE Transactions on Industrial Electronics, Vol. 55, No. 3, 2008, pp. 1256-1270

[23] A. Ürmös, Z. Farkas, M. Farkas, T. Sándor, L. T. Kóczy, Á. Nemcsics: Application of self-organizing maps for technological support of droplet epitaxy, Acta Polytechnica Hungarica, Vol. 14, No. 4, 2017, pp. 207-224

[24] A. Szántó, S. Hajdu, G. Á. Sziki: Dynamic Simulation of a Prototype Race Car Driven by Series Wound DC Motor in Matlab-Simulink, Acta Polytechnica Hungarica, Vol. 17, No. 4, 2020, pp. 103-122

[25] Q. Bi, W. J. Cai, E. L. Lee, Q. G. Wang, C. C. Hang, Y. Zhang: Robust identification of first-order plus dead-time model from step response, Control Engineering Practice, Vol. 7, No. 1, 1999, pp. 71-77

[26] S. Skogestad: Simple analytical rules for model reduction and PID controller tuning, Jornal Process Control, Vol. 13, No. 4, 2003, pp. 291-309

[27] R. Gerov, Z. Jovanovic: Parameter Estimation Method for the Unstable Time Delay Process, Acta Polytechnica Hungarica, Vol. 16, No. 3, 2019, pp. 101-120

[28] R. Gerov, Z. Jovanovic: Closed-loop identification of a first-order plus time delay model using Lambert W function, 2019 IEEE 17th International

Symposium on Intelligent Systems and Informatics (SISY), Subotica, Serbia, 2019, pp. 000067-000070

[29] Q. Wang, C. Hang, B. Zou, Low-order modeling from relay feedback, Industrial and Engineering Chemistry Research, Vol. 36, No. 2, 1997, pp. 375-381

[30] W. Li, E. Eskinat, W. Luyben: An improved auto-tune identification method, Industrial and Engineering Chemistry Research, Vol. 30, No. 7, 1991, pp. 1530-1541

[31] T. Liu, F. Gao: Alternative identification algorithms for obtaining a first-order stable/unstable process model from a single relay feedback test, Industrial and Engineering Chemistry Research, Vol. 47, No. 4, 2008, pp. 1140-1149

[32] T. Liu, Q. G. Wang, H. P. Huang: A tutorial review on process identification from step or relay feedback test, Journal of Process Control, Vol. 23, No. 10, 2013, pp. 1597-1623

[33] K. Tan, T. Lee, S. Huang, K. Chua, R. Ferdous: Improved critical point estimation using a preload relay, Journal of Process Control, Vol. 16, No. 5, 2006, pp. 445-455

[34] R. Gerov, Z. Jovanović: Parameter Estimation of the IPDT Model using the Lambert W Function, 2019 14th International Conference on Advanced Technologies, Systems and Services in Telecommunications (TELSIKS), Nis, Serbia, 2019, pp. 400-403

[35] R. Corless, G. Gonnet, D. Hare, D. Jeffrey, D. Knuth: On the Lambert W function, Advances in Computational Mathematics, Vol. 5, 1996, pp. 329-359

[36] S. Yi, S. Duan, P. W. Nelson, A. G. Ulsoy: The Lambert W Function Approach to Time Delay Systems and the LambertW_DDE Toolbox, Proceedings of the 10th IFAC Workshop on Time Delay Systems, The International Federation of Automatic Control Northeastern University, Boston, USA, June 22-24, 2012, pp. 114-119

[37] L. Pekař, Q. Gao: Spectrum analysis of LTI continuous-time systems with constant delays: A literature overview of some recent results, IEEE Access, Vol. 6, 2018, pp. 35457-35491

[38] R. Wood, M. Berry: Terminal composition control of a binary distillation column, Chemical Engineering Science, Vol. 28, 1973, pp. 1707-1717

Hierarchical Mapping of an Electric Vehicle Sensor and Control Network

István Nagy

Óbuda University, Bánki Donát Faculty of Mechanical & Safety Engineering,
Institute of Mechatronics & Vehicle Engineering, Dept. of Mechatronics
H-1081 Budapest, Népszínház u. 8, Hungary
Email: nagy.istvan@bgk.uni-obuda.hu

Abstract: This article reviews the electronic networks used in automotive engineering, with particular reference to a fully electric vehicle (EV). The block diagram of the electronic network of the vehicle is assembled on the basis of measurements and studies carried out on a university EV. The block diagram includes the network connections of sensors, actuators, switches, indicators, control systems, and sub-systems of the vehicle. After mapping the electrical network, the paper is briefly surveying the communication systems and control processors used in EV, then investigates the causes of the probabilities of the failures from the sensor core up to the control units. Regarding sensors investigation, the most important sensor, the wheel speed sensor, will be examined, then the LIN and CAN bus systems operation and its possible faults will be reviewed, analysed. At the end of the article, in the appendix, the complete electronic network of the vehicle can be seen.

Keywords: Control Units (CUs); Control Modules (CMs); Electric Vehicle Control (EVC); Vehicle Control Module (VCM)

1 Introduction

Nowadays electric vehicles are becoming more and more important in our lives. However, as manufacturers hold patents and guard their knowledge carefully, only a limited amount of information is passed on to researchers independent of any one manufacturer. This article tries to fill in some of the gaps in engineering research. Articles related to electric vehicles can be classified into the following categories.

- Articles dealing with *charging* options for electric devices, [1], [2]
- Articles dealing with *controls*, like the SRM motor's control and simulation [3]

- Articles dealing with the kinematic and dynamic control of the unmanned vehicles [4]
- Articles examining the workings of the internal combustion engine and the electric motor in a hybrid EV (HEV). [5]
- Articles addressing the harness [6]
- Articles examining sensors used in EVs to monitor driver behaviour [7]

Although AMR sensors have been available to the industry for a relatively short period of time, there are nevertheless several studies looking at their theoretical basis [8], [9]. In this article, the AMR sensors used in vehicle engineering will be shown as the lower level of the control hierarchy.

Among the scientific articles or conference papers reviewed, the author did not find one which attempted to map the electronic, sensory, and control network of an EV. Therefore, this article will pay particular attention to this topic, by trying to map all the electric connections of a vehicle, and then by specifying the electrical path from sensor to CU, and examining the communication systems.

The structure of the article can be summarized as follows.

After the introduction, the article reveals the electronic network of a particular EV, and then deals with different communication (Bus) systems and protocols, used in vehicle engineering, where the different possible failures will be examined. In addition, the paper will highlight the path of the electric signal (impulse) from the wheel speed sensor to the onboard computer. In Section 4, the control units of the embedded systems will be surveyed, and some hierarchy will be built from the sensor core to the onboard processor. The article will conclude by summarizing the findings. There is also an appendix, in which the complete sensory and control network is mapped.

2 Mapping the Electronic Control System of a Particular EV[1]

It is not an easy task to begin to discover the electronic system of a vehicle without having the correct documentation. Thanks to the Institute for Computer Science and Control of the Hungarian Academy of Sciences (MTA SZTAKI)[2], the author was able to obtain the service book [10] for the vehicle in question, from which a lot of useful information was derived.

[1] The particular EV is a *NISSAN LEAF Z0,* owned by Óbuda University.

[2] Hungarian Academy of Sciences, Institute for Computer Science and Control.

The first step in mapping the electric network of a vehicle involves finding the main nodes of the network. Primarily the control modules, such as the Vehicle Control Module (VCM), and the Body Control Module (BCM) etc. were considered as main nodes, but the network seemed so chaotic that it needed to be divided into sub-systems. There are 9 sub-systems in this division (or 10, if EVB will be separated from EVC). The sub-systems contain one or more control modules that in some cases are almost directly (through some interfaces, which are usually integrated into the sensors) connected to the sensors, actuators, switches, indicators. Continuing this idea, in order of importance, the following sub-systems can be set up.

2.1. EV Control System (EVC)

This system should be classified as the main system of the vehicle. It contains two modules, the Vehicle Control Module (VCM), and the Intelligent Power Distribution Module in the Engine Room (IPDM E/R), see the darkened section in Fig. 1 (below). The EVC is responsible for the proper electric power train, and power transmission in the vehicle. Through the IPDM module, the "cost-effective" (energy efficient) operation of the vehicle is controlled. A sub-system of this EVC is the EVB (EV Battery System), which controls the Li-ion battery system of the vehicle. Here the Power Delivery Module (PDM) plays the main role in the control. The PDM is connected to the Li-ion battery controller unit, which (among other things) monitors the battery current and battery temperature. The EV control system connections can be seen in Fig. 1.

The ASCD (Automatic Speed Control Device) cannot be neglected in this diagram. It allows a driver to keep the vehicle at a predetermined constant speed, without pressing the accelerator pedal (popularly this is known as a "tempo-mat" switch). The operation is the following: The VCM module receives the vehicle speed signal from the electronically-driven intelligent brake unit (ABS), processes it with the motor speed signal, and controls the traction motor to regulate vehicle speed. This is also known as cruise control.

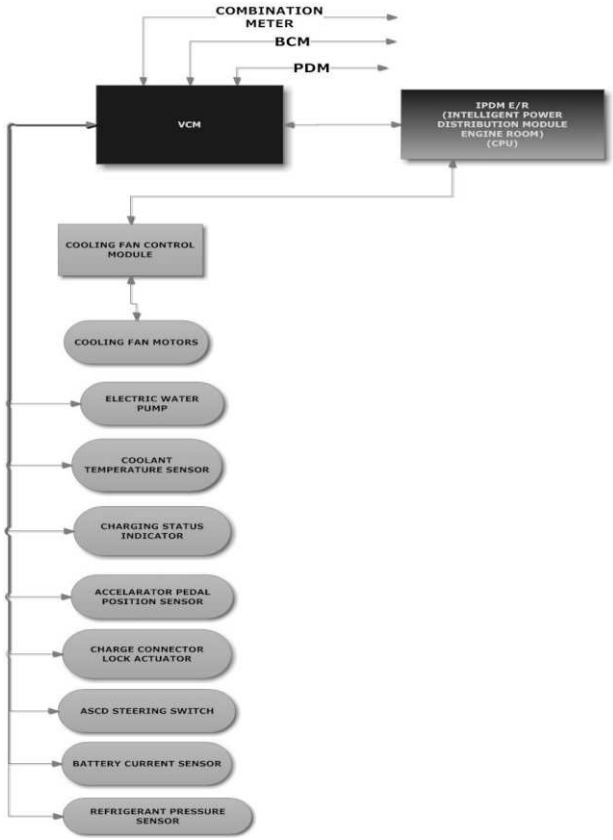

Figure 1
The EV sub-system

2.2. Driver Control System

This sub-system contains the most modules, units, sensors and actuators. Furthermore, it includes those parts of the system, which can be controlled or operated by the driver.

The diagram shows that the system contains three control MODULES (see darkened rectangles at the top, which are representing the top hierarchy level). Beneath are two control UNITS for “approaching vehicle sound for pedestrians” (APVSP) and “auto levelizer”, two “combination switches” plus a “horn relay” (see, lighter rectangles, which are representing the middle level of hierarchy). Below these boxes, the SENSORS and ACTUATORS, as low level of hierarchy, can be found (see, elliptical shapes). The directed lines on the upper part of the diagram indicate the connections to other modules. Control units in the middle level of hierarchy are pre-processing the signals for the modules in the upper

hierarchy level. Basically, the hierarchy from top to down is built up from MODULES; UNITS; ACTUATORS and SENSORS.

Figure 2
The electronic network of the Driver Control System

2.3. The Brake Control System and Electronically Controlled Power Steering System

The importance of these sub-systems is in the driving dynamics properties of the vehicle. Here, the sensors and actuators are connected to the different control units in the medium hierarchy level, such as the electronically-driven Intelligent Brake Unit, the ABS actuator and the Electric Control Unit (ECU), EPS control unit. Further control units are connected to the modules, see the upper part of Fig. 3 (the arrows to the left).

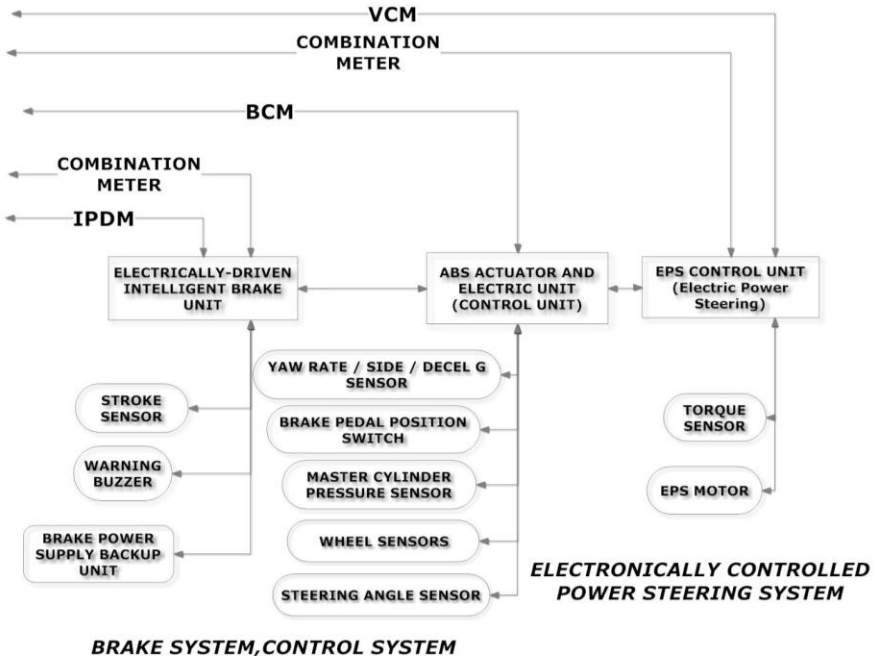

Figure 3

The Brake Control System (left) and the Electronically Controlled Power Steering System, *EPS* (right)

The task of units: *electrically-driven intelligent brake unit* integrates the control, master cylinder, brake booster, and checking the fluid pressure. This "reports" to the *ABS actuator and electric unit*, which is direct connected to the *EPS Control Unit*. Essentially this electrically-driven intelligent brake is a booster system that generates force to assist braking by using an internal motor to operate a piston inside the brake cylinder. The parking brake system (PBS) is also included in this system.

The *EPS control unit* performs an arithmetical operation on data, such as steering wheel turning force (sensor signal) from the torque sensor, vehicle speed signal, and EPS motor position signal, which is obtained from the *EPS motor*.

It processes these signals and generates an optimum torque assist signal to the EPS motor appropriate for the driving conditions. In case of malfunction, the system enters into the manual steering mode.

2.4. The Vehicle Charging System, Traction Motor System, and Electric Shift

These three sub-systems are served by three modules (PDM, IPDM, VCM). Their operation will be discussed separately in the sub-sections below.

2.4.1. Vehicle Charging System, Traction Motor System (Power Train)

The task of the charging system is to make the most of the public power network (220/50) to charge the Li-ion batteries of the EV. The PDM plays a key role in this process. The charger uses two-converter systems, consisting of the Power Factor Correction (PFC) circuit and the DC/DC converter, which improve charging efficiency, charge level accuracy, and consequently the service life of a Li-ion battery. The PFC is a device that efficiently converts AC power supply input to slightly pulsing, but more energized DC power. The operation of the charging system is the following: the PDM detects the input power supply (either 110 V or 220 V) and switches the charger to the appropriate mode. Then the AC source is filtered and rectified by the 2-way rectifier. Then the PFC improves and boosts the power factor of the rectified signal. This boosted signal is again converted to AC by the inverter. The insulation transformer converting the AC to the high-voltage and the 2nd rectifier results in high-voltage DC power. In addition to all of this, the insulation transformer separates the charging circuits from the vehicle's circuits. The whole process can be seen in Fig. 4.

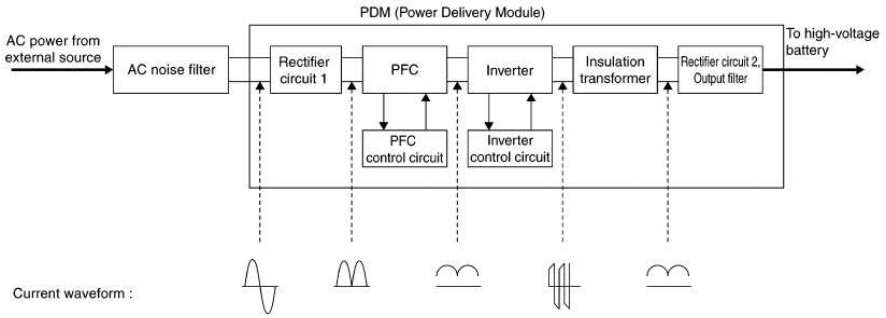

Figure 4
The EV charging process

The possibility of solar charging should also be mentioned here. This type of vehicle is equipped with a solar cell module to charge the 12 V battery. Charging depends on the power generation of the cells, which depends on the amount of

solar radiation available. The battery is not recharged, when this amount of power is low. The ideal conditions can be described approximately as being fair weather, with the temperature around 25^0C, and between 11am and 2pm, with the cell clean and in sunlight. Charging occurs when the *emf* (electro-motive force) of the cell is more than the battery voltage. The charging current corresponds to the potential difference between the battery and the *emf* of the cell.

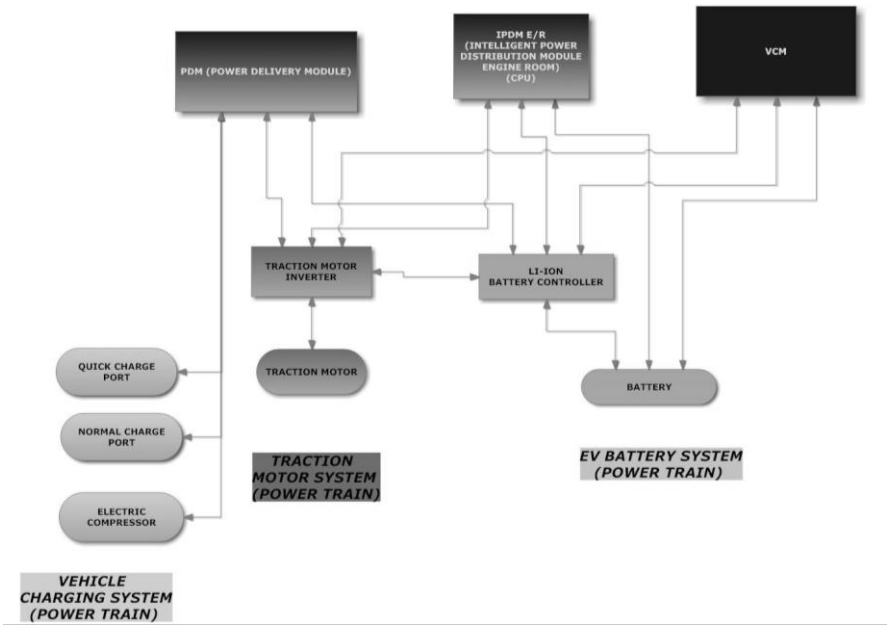

Figure 5
Vehicle charging System and the Power Train

2.4.2. Traction Motor (power train) System and Electric Shift Control Module

The traction motor is a compact Interior Permanent Magnet Synchronous Motor (IPMSM) with high power output and high efficiency. Essentially this is a 3-phase synchronous AC motor, with an electronic IGBT (Insulated Gate Bipolar Transistor) commutation. The traction motor inverter converts the DC power, from the Li-ion battery to the AC power, which drives the motor. The AC power frequency and voltage created can be varied with the DC converter, which results in a high control performance of the IPMSM. The traction motor inverter can be regarded as the motor controller, because it regulates the motor performance based on the required motor torque signal obtained from the EV System of the VCM. The regulation accuracy of *torque* is based on the current sensor detection signal, while the *RPM* (which is sensed by the traction motor resolver) depends on the

frequency of the 3-phase current. Moreover, the traction motor inverter performs vibration control in order to improve accelerator response and provide better acceleration during driving.

The *Electric Shift Control Module* is built into the VCM, and determines the shift position, based on the shift position data captured from the electric shift sensor. It transmits data to the VCM and traction motor inverter via the CAN Bus system. This module also controls the parking actuator, based on the signal from the position of the *Electric Shift Selector* (known commonly as the gearstick).

The components of the *Traction Motor System* (power train) are the following: traction motor, connected to the traction motor inverter, which is controlled through the PDM (see Fig. 5).

2.5. Tyre Pressure, SRS Air Bag and Body Exterior (door, window, security) Systems

Because this article trying to map the connections between the sensors and their controllers, so the author will focus on these devices in these sub-systems.

2.5.1. Body Exterior and Security System

With the emphasis on safety equipment, first the sensors/actuators will be described, which can be found in this sub-system. The intelligent-key antennas (outside-rear, outside-passenger side, outside-driver side; inside-luggage room, inside-rear seat, inside-instrument centre) can detect when the legitimate owner is near the vehicle, and based on this, when the key lock is touched, unlock the steering wheel. The communication between the key and the units goes through the NATS (Nissan Anti-Theft System) antenna. The units transmit the signal towards the BCM module. One of the units is the *Siren Control Unit*, which monitors the vehicle condition and controls the vehicle security system. The *intruder sensor* detects movement in the passenger compartment and then transmits a signal to the siren control, which transmits it onto the BCM. The *power door lock system* is also part of the intelligent key system. Given all this, the BCM can be regarded as the key module for car security.

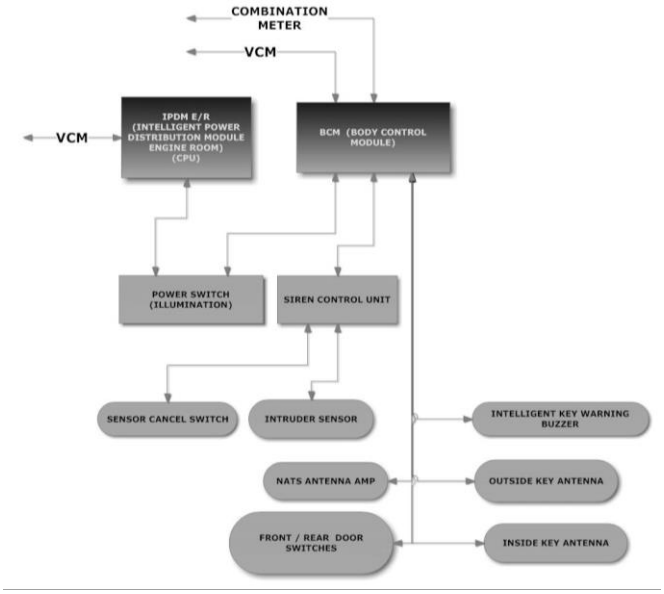

Figure 6
The Body Exterior and Security System

2.5.2. Tyre Pressure and SRS Air Bag Systems

The Supplemental Restraint System (SRS), regarding the sensors, can be divided into two main modules: *air bag diagnosis sensor* – controlling the airbags, and the *crash zone sensor* – integrating the crash sensors' data. The main parts of the system are as follows: the spiral cable, which provides the connection between the airbag diagnosis sensor and the driver airbag module; the *crash zone sensor* – integrating the frontal collision sensor and the satellite sensor (for lateral and roll-over collisions); the *airbag diagnosis sensor* – controlling the driver airbag, passenger airbag, side airbag, curtain airbag, seatbelt pre-tensioner, lap pre-tensioner.

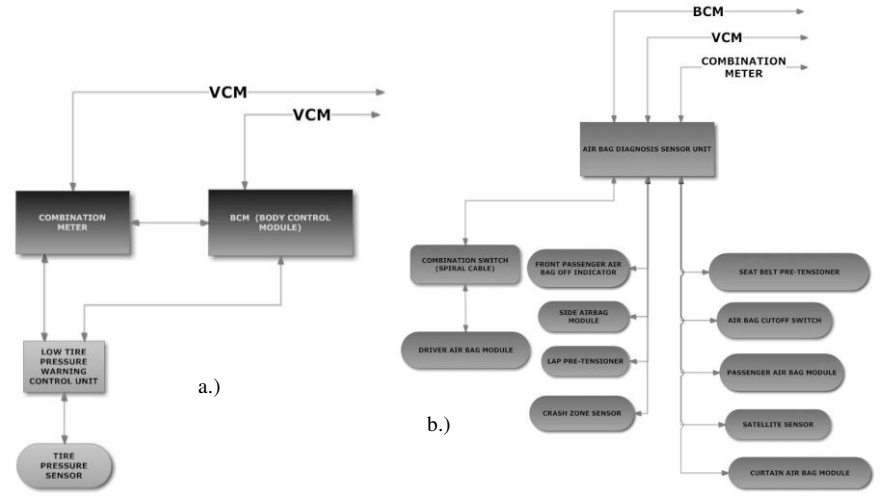

Figure 7
The Tyre Pressure a) and SRS Air Bag System b)

Regarding tyre pressure, basically, two types of sensors can be distinguished. The *direct sensors* are mounted directly onto each wheel and measure the air pressure inside each individual tyre, while the *indirect sensors* work with the ABS, evaluating the tyre pressures from the wheel speeds (if the tyre pressure is low, the wheel is rolling with different speed, because the nominal diameter of the wheel is decreased). The indication of low pressure is displayed on a combination meter, see Fig. 7 a).

2.6. Summary of Electronic Control System Mapping

In the summary, the individual sub-systems and the real control modules (boxed units), connections will be illustrated, (see below). In some previously published conference papers [11], published by the author, several stand-alone sub-systems were examined. Portrayal of the whole system, with this level of complexity, is published for the first time here.

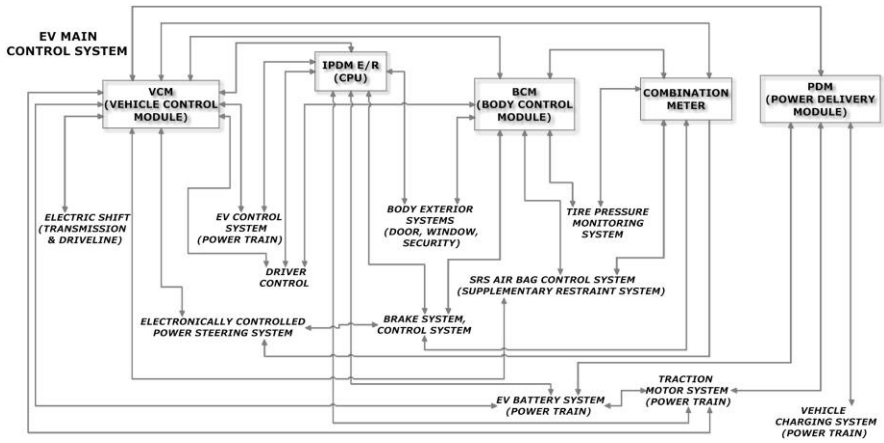

Figure 8
The Control Modules and the Sub-system's relations

3 Communication Systems used in EVs

In this section the most frequently used communication systems of vehicles will be surveyed. The author has already partly addressed this issue in a previously published paper [12], where the CAN system was examined, so this will be only referred to in this section. The communication systems, given the medium of communication, can be enrolled into two main classes, namely wired and wireless communications. Systems can be classified further based on the distance between the communication devices: *in-vehicle* communication (*InV*), and communication *outside* the vehicle. Outside communication can be classified still further into *medium* (car to car (*V2V*), or car to infrastructure (*V2I*)) and *long* (car-satellite (*V2S*) or car to everything (*V2X*)) *range* communications. Table 1 summarizes the communication systems.

Table 1
Vehicle Communications Systems

In-Car System		**Outside** of Car	
Wired (*InV*)	**wireless** (*InV*)	**medium(short)** range (*V2V, V2I*)	**long** range (*V2I, V2X, V2S*)
LIN	BlueTooth	mmWave (~50 m)	Cellular Techs (~15 km)
CAN	UWB	5 G (~50 m)	WiMax (~40 km)
FlexRay	ZigBee	WiFi (50 m-1 km)	LTE-A-Pro (~30 km)
MOST		DSCR (~1 km)	UMTS (~10 km)
Automotive Ethernet			GPS (*V2S*)

The diagrams, prepared above (see Section 2), use communication systems highlighted in grey in the table. In the next two sections, these will be detailed.

3.1. The Local Interconnect Network (LIN)

In the hierarchy of the automotive communicative network, the LIN is located on the lowest level. It usually connects the switches or indicators (lamps) to the *control units*, located under the *control modules*, in the lowest level of the electrical network. The "one master-multi slave", the bus-topology network is driven by UART/SCI interface and realized by one wire with a maximum length of 40 m, and with a maximum number of 16 slave nodes. It has a self-synchronizing ability (in frame header is the synchronizing field) and good flexibility.

3.1.1. Possible Malfunctions

Table 2
The malfunctions and symptoms of LIN communication

malfunction	**symptom**
Power supply voltage is out of range (8-18)[V]	The ECU of LIN still operates, but the communication is not guaranteed
Losing the power supply or GND	The unpowered ECUs (slaves) do not obstruct the normal communication
Shortcut between power supply and GND	The communication breaks down, but no damage occurs. After removing the error, the system will operate normally.

Regarding bit-rate and signal distortion, it is important to know the capacity (C_{BUS}) and resistance value (R_{BUS}) of the Bus, because the time constant (τ) determines the signal change rate at the rising edge (slope) of the signal. The calculation is based on the following equations [13].

$$C_{BUS} = C_{MASTER} + n.C_{SLAVE} + C'_{LINE}.Length_{BUS} \tag{1}$$

and the BUS resistance

$$R_{BUS} = R_{MASTER} \times R_{SLAVE1} \times ... \times R_{SLAVEn} \tag{2}$$

the time constant, which influences the signal shape, and bit rate

$$\tau = C_{BUS}.R_{BUS} \tag{3}$$

where "n" is the number of slave nodes, C'_{LINE} is the BUS capacity on unit length.

3.1.2. LIN Applications in Vehicle Engineering

The LIN's communication method has the following advantages: ease of use, relative simplicity, cheapness, wide availability of components, simple harness, and the flexibility of extension. What is known as non-demanding equipment (listed below) uses this communication.

Table 3
The practical applications of LIN communication

segment of operation	practical use
The roof	Light sensor, light control, sunroof
Steering wheel	Cruise Control Sw., wiper, turning light, radio, wheel lock - switches
Seats	Seat position motor and sensors
Engine	Cooling fan motor
Climate	Small motors, control panel
Door	Mirrors, window lift, door lock

3.2. Controller Area Network (CAN)

The CAN Bus system of this particular vehicle and possible CAN Bus failures, regarding *shorted* and *opened* circuits, are discussed in [12], so the author will just make reference to it. Here, in this article the CAN connections of diagrams described earlier in Section 2 will be shown.

There are 5 main Control Modules (CMs) in the EV Control System (*VCM, BCM, IPDM E/R, PDM, Combination meter*) which are connected to each other via this (CAN) protocol. Moreover, the connections between the Control Units (there are 9 control units (CUs): *VSP, Auto levelizer CU, Li-ion Battery Controller, EPS, Tyre pressure CU, ABS CU, Electrically-driven intelligent brake CU, cooling Fan CU, SRS Airbag CU*) and Control Modules are also realized through the CAN Bus system. Not only this but further down the network hierarchy, some intelligent sensors (like AMR wheel Speed sensors) are also connected via CAN to their control units. After mapping the electronic system of the vehicle a table of signals and control units communicating on the CAN Bus system can be created. (Due to the limitations of the size of the paper, the full table will not be displayed).

The table can be useful in searching for possible communications failures in the Bus system. For example, the vehicle is in motion, but the speedometer (tachometer, part of combination meter) is not moving. The table shows that a signal should be transmitted (T) by the ECM and received (R) by the Combination meter. Therefore, one can conclude that in this case, the transmission of a signal between the ECM and the Combination meter is not functioning properly.

Table 4
The signals that travel on CAN System and main CMs

Control Units *Signal name*	**ECM**	**BCM**	**Combination meter**	**STRG**[3]	**ABS**	**IPDM E/R**
A/C compressor feedback	T		R			
A/C compressor request	T					R
Accelerator pedal position	T				R	
Cooling fan motor operation	T					R
Engine coolant temperature	T		R			
Engine speed signal	T		R		R	
Fuel consumption monitor signal	T		R			
Malfunction indicator lamp signal	T		R			
A/C switch signal	R	T				
Ignition switch signal		T				R
Sleep / wake up signal		T	R			R
…						

4 Control Circuits Used in EVs

After mapping the electronic circuits of the vehicle a hierarchical system begins to emerge. At the bottom of this system are lamps, indicators, sensing core of the sensors, and on the top is the VCM. Based on this hierarchy, different control circuits are used for signal transferring and data processing. In the case of vehicle engineering, the control units are embedded systems. The embedded systems usually consist of (in order: Input → Output): sensors, signal conditioning unit, central control unit, output interface, actuator, or indicator. The control circuits, including processors, can be either a microcontroller, microprocessor, or high-complexity control logic, e.g. CPLD / FPGA.

[3] Steering Unit

The central control units can be classified into three main classes, where the top class is the *General Purpose Processor* (GPP). Main features: relative low speed but high complexity, supporting on-chip DMA, and on-chip Cache, provides HW circuits for commonly used math and logic operations, uses pipeline, and wide data buses, and at the end, the cost is relatively high. Summary: high complexity and flexibility, relatively high cost, relatively low performance.

The Application Specific Instruction set Processor (ASIP) can be put into the medium class of control circuits. This uses SoC (*System on Chip*) technology and the set of instructions is usually tailored to the task. The medium class is between the flexibility of GPP and the performance of ASIC circuits. Summary: performance many times faster than GPP, effective with a smaller number of instructions, less complexity, medium flexibility.

The lower class of control circuits form the Application Specific Integrated Circuits (ASIC). The word "lower" is not used pejoratively but simply means that this type of controller is near to the physical level control. The circuits have low flexibility and complexity, but very high performance for the given task. It has no instruction set, but instead, the program is burned into the IC. They are available in two versions: semi-customized, where the circuit contains pre-programmed segments; fully customized, where the circuit is fully designed by the developer. Most known among such circuits are the PAL, PLA, GAL circuits, and somewhere a little bit higher the FPGAs and CPLDs. Summary: high performance, fitted to the given task, relatively low cost, and very low flexibility.

At the end of section, the control circuits that can be assigned to different levels of the hierarchy are summarized, see Fig. 9.

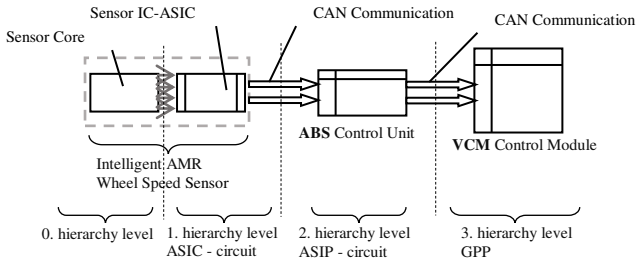

Figure 9

The hierarchy levels from sensor core to the top level of hierarchy and the possible control circuits in different levels

Conclusions

In this paper, the electronic control network of a particular vehicle has been introduced. References [11] and [12], where the communication and the AMR wheel speed sensors are detailed, make this article more complete.

The author has tried to explore the connections between the sensors, indicators, switches, and the control unit in a specific EV, by dividing the whole system into operational sub-systems, mapping these sub-systems in detail. (Section 2) The sub-systems and their connectivity to the control modules are illustrated on Fig. 8. Finally, the whole map of the connectivity is presented in Attachment nr. 1. The mapped system can provide a very good base for further analysis of error-spreading on the network (something the author plans to examine in a future paper), or for evaluation of the reliability of the system [14], and not less in graph-model creating of the system [15].

Table 5
NOMENCLATURE

Acro-nym	Meaning	Acro-nym	Meaning	Acro-nym	Meaning	Acro-nym	Meaning
ABS	Anti-lock Braking System	**CU**	Control Unit	**HEV**	Hybrid Electric Vehicle	**PFC**	Power Factor Correction
AMR	Anisotropic Magneto-Resistive (sensor)	**DMA**	Direct Memory Acces	**IGBT**	Insulated Gate Bi-polar Transistor	**PLA**	Programmable Logic Array
APVSP	Approaching Vehicle Sound for Pedestrians	**EMF**	Electro-motive Force	**IPDM**	Intelligent Power Distribution Module	**R**	Receiver
ASCD	Automatic Speed Control Device	**EPS**	Electric Power Steering System	**IPDM E/R**	Intelligent Power Distribution Module, Engine Room	**RPM**	Rotation per Minute
ASIC	Application Specific Integrated Circuit	**EV**	Electric Vehicle	**IPMSM**	Interior Permanent Magnet Synchronous Motor	**SoC**	System on Chip
ASIP	Application Specific Instruction-set Processor	**EVB**	Electric Vehicle Battery System	**LIN**	Local Interconnect Network	**SRS**	Supplemental Restraint System
BCM	Body control Module	**EVC**	Electric Vehicle Control System	**NATS**	Nissan Anti-Theft System	**T**	Transmitter
CAN	Controller Area Network	**FPGA**	Field Programmable Gate Array	**PAL**	Programmable Array Logic	**VCM**	Vehicle Control module
CM	Contol Module	**GAL**	General Array Logic	**PBS**	parking brake system		
CPLD	Complex Programmable Logic Device	**GPP**	General Purpose Processor	**PDM**	Power Distribution Module		

Acknowledgement

The research presented in this paper was carried out as part of the *EFOP 3.6.2-16-2017-00016* project in the framework of the *Széchenyi Plan*. The completion of this project is funded by the European Union and co-financed by the European Social Fund.

References

[1] N. D. Mazharov, S. M. Hristov, D. A. Dichev, I. S. Zhelezarov: Some Problems of Dynamic Contactless Charging of Electric Vehicles; Acta Polytechnica Hungarica, Vol. 14, Nr. 4, 2017, pp. 7-26

[2] P. Kádár, A. Varga: Photo Voltaic EV charge Station; in 11th International Symposium on Applied Machine Intelligence and Informatics (SAMI 2013) IEEE, ISBN 978-1-4673-5929-0, Herlany, Slovakia, pp. 57-60

[3] S. Sadeghi, M. Mirsalim, A. H. Isfahani: Dynamic Modelling and Simulation of a Switched Reluctance Motor in a Series Hybrid Electric Vehicle; Acta Polytechnica Hungarica, Vol. 7, Nr. 1, 2010, pp. 51-71

[4] B. Lantos, Zs. Bodó: High Level Kinematic and Low Level Nonlinear Dynamic Control of Unmanned Ground Vehicles; Acta Polytechnica Hungarica, Vol. 16, Nr. 1, 2019, pp. 97-117

[5] Zs. Preitl, P. Bauer, J. Bokor: Cascade Control Solution for Traction Motor for Hybrid Electric Vehicles; Acta Polytechnica Hungarica, Vol. 4, Nr. 3, 2007, pp. 75-88

[6] T. Sawatdee, P. Chutima: Design Process Improvement for Electric Car Harness; MOIME2017, in IOP Conference Series: Materials Science and Engineering 215 (2017) 012011, DOI:10.1088/1757-899X215/1/012011, pp. 1-7

[7] G. Fördős, I. Bosznai, L. Kovács, B. Benyó, Z. Benyó: Sensor-net for Monitoring Vital Parameters of Vehicle Drivers; Acta Polytechnica Hungarica, Vol. 4, Nr. 4, 2007, pp. 25-36

[8] R. Guyol: "AMR Angle Sensors", in analog Devices, Inc. AN12487-0-10/14(0), 2014, p. 4

[9] R. Slatter: Magnetoresistive (MR) sensors for Angle-, Path- and Current Measurement in Harsh Environments; AMA Conferences 2015, Sensor 2015 and IRS 2015, DOI 10.5162/sensor2015/B3.1, pp. 228-233

[10] Nissan Leaf Z0, Service Book, Electrical & Power Control, Section: Power Supply, Ground & Circuit Elements, 2013

[11] I. Nagy, Sz. Tuloki: Fault Analysis and System Modelling in Vehicle Engineering; in Proc of IEEE 18th International Symposium on Computational Intelligence and Informatics (CINTI 2018), Budapest, Hungary, 2018, pp. 313-319

[12] I. Nagy, F. B. Vér: Practical Analysis of an AMR Wheel Speed Sensor and CAN Bus System for the Communication's Failures and its Implications to the EV's Control System; in IEEE 17th International Symposium on Intelligent Systems and Informatics Proceedings (SISY 2019) Subotica, Serbia, pp. 241-247

[13] D. Fodor, Zs. Szalay: Autóipari kommunikációs eszközök; Pannon Egyetem, 2014, pp. 46-116

[14] L. Pokorádi, P. Felker: Interval Uncertainty Analysis of Bridge Structure Systems' Reliability (SISY 2019) IEEE, 17th International Symposium on Intelligent Systems and Informatics, September 12-14, 2019, Subotica, Serbia, pp. 235-239

[15] L. Pokorádi, "Graph model-based analysis of technical systems", IOP Conference Series: Materials Science and Engineering 393 : 1 Paper: 012007, 8 p. (2018)

Attachment nr.1